UNIVERSITY OF TRENTO

Department of Mathematics

XXXII CYCLE

Mathematical Modeling of Prostate Cancer Immunotherapy

Ph.D. thesis of

Roberta Coletti

Supervisors:

Prof. Corrado Priami

Dr. Luca Marchetti

May 28, 2020

"Your time is limited, so don't waste it living someone else's life.

Don't be trapped by dogma — which is living with the results of other people's thinking.

Don't let the noise of others' opinions drown out your own inner voice.

And most important, have the courage to follow your heart and intuition.

They somehow already know what you truly want to become."

S. J.

Dedicated to my family,

my love and my friends.

Abstract

Immunotherapy, by enhancing the endogenous anti-tumor immune responses, is showing promising results for the treatment of numerous cancers refractory to conventional therapies. However, its effectiveness for advanced castration-resistant prostate cancer remains unsatisfactory and new therapeutic strategies need to be developed. To this end, mathematical modeling provides a quantitative framework for testing *in silico* the efficacy of new treatments and combination therapies, as well as understanding unknown biological mechanisms. In this dissertation we present two mathematical models of prostate cancer immunotherapy defined as systems of ordinary differential equations.

The first work, introduced in Chapter 2, provides a mathematical model of prostate cancer immunotherapy which has been calibrated using data from pre-clinical experiments in mice. This model describes the evolution of prostate cancer, key components of the immune system, and seven treatments. Numerous combination therapies were evaluated considering both the degree of tumor inhibition and the predicted synergistic effects, integrated into a decision tree. Our simulations predicted cancer vaccine combined with immune checkpoint blockade as the most effective dual-drug combination immunotherapy for subjects treated with androgen-deprivation therapy that developed resistance. Overall, this model serves as a computational framework to support drug development, by generating hypotheses that can be tested experimentally in pre-clinical models.

The Chapter 3 is devoted to the description of a human prostate cancer mathematical model. The potential effect of immunotherapies on castration-resistant form has been analyzed. In

particular, the model includes the dendritic vaccine *sipuleucel-T*, the only currently available immunotherapy option for advanced prostate cancer, and the *ipilimumab*, a drug targeting the cytotoxic T-lymphocyte antigen 4 , exposed on the CTLs membrane, currently under Phase II clinical trial. From a mathematical analysis of a simplified model, it seems likely that, under continuous administration of *ipilimumab*, the system lies in a bistable situation where both the no-tumor equilibrium and the high-tumor equilibrium are attractive. The schedule of periodic treatments could then determine the outcome, and mathematical models could help in deciding an optimal schedule.

Publications included in this thesis

This thesis contains material which has already been published or has been submitted for publication:

- Roberta Coletti, Lorena Leonardelli, Silvia Parolo, and Luca Marchetti (in press). A QSP model of prostate cancer immunotherapy toidentify effective combination therapies. *Scientific Reports*.

- Roberta Coletti, Andrea Pugliese, and Luca Marchetti (2020). Modeling the effect of immunotherapies on human castration-resistant prostate cancer. *Submitted manuscript*.

Contents

List of Figures

List of Tables

Introduction

Mathematical modeling has been successfully applied in the context of computational systems biology to develop comprehensive mathematical descriptions of several pathologies [1–9]. Mathematical models are calibrated through experimental data to simulate *in silico* biological systems and test hypotheses, for example regarding the regulative mechanisms of complex diseases [10–16].

Cancer immunotherapy is an emerging treatment approach that stimulates the immune system against tumors, by enhancing or suppressing the immune response [17]. The idea of modulating the immune response as cancer therapy is a direct consequence of the strong, well recognized interplay between tumors and the immune system. Indeed, the genetic alterations in cancer cells promote the activation of the immune system that starts a series of events, known as cancer-immunity cycle, to control cancer growth [18].

In the past few years, many progresses have been performed in the treatment of cancer by immunotherapies, especially in hematological cancer, such as leukemia, and some solid tumors, as metastatic melanoma and renal carcinoma [19]. In this context, deciding the right doses or protocols may be critical, and mathematical models can be crucial for supporting these medical decisions as well as understanding unknown cell-interaction mechanisms. In the literature, there are many mathematical models of cancer immunotherapy [3], which can be generically formulated on the basis of common tumor-immune features [20] or targeted to a particular tumor type, such as renal cell carcinoma [21], brain tumors [22] and prostate cancer [23; 24]. Mathematical models describe the immune system and tumor interactions, including the effect of immunotherapies as single treatments [25], or combined with classical therapies, such as chemotherapy [26; 27].

Moreover, models have been used to investigate not well known mechanisms, such as recurrence and immunostimulation [28] or the tumor capacity to escape the immune control [29]. Another interesting modeling application is the *in silico* evaluation of drug efficacy and of the optimal administration protocol for single or combination therapies, as in [30–33].

The supporting for the pharmaceutical industry by mathematical models is a promising approach, because these models represent a cost-effective way to predict and investigate the efficacy of a therapy. Indeed, the development of a new pharmaceutical drug is a very complex and long process. It includes a first phase of pre-clinical studies, involving *in vitro* and *in vivo* experiments on animals, which are necessary for understanding molecular features. At the end of this phase, the relative information are submitted to the US Food and Drug Administration (FDA) and, if they are approved, the development moves to the clinical studies. The clinical phase is composed by 4 steps of experiments on humans in order to introduce the drug on market. The whole process could be long, with an average time of 7 - 10 years, and expensive. Literature studies have estimated that the cost needed to bring new therapies to market varies from 161 million to 2 billion of US dollars [34]. Moreover, there are evidences that highlight a significant variability in drug responses for different patients, motivating the pharmaceutical industries to invest in personalized medicine [35; 36]. In this context, the Quantitative System Pharmacology (QSP) modeling technique is particularly relevant. Indeed, this innovative approach allows the inclusion of several data from different sources, integrated in compartmental and hierarchical mathematical models, which comprehends the pharmacokinetics and pharmacodynamics [37; 38]. Therefore, the QSP mathematical models can help in validating or identifying drug targets, designing new therapies and evaluating side effects for low costs [39–43].

This thesis is focused on Prostate Cancer (PCa), one of the leading causes of cancer-associated death in the male population [44–46]. Patients diagnosed with localized PCa are usually monitored for their blood levels of prostate-specific antigen and, when appropriate, are treated with radiation therapy or prostatectomy [47]. However, 20-40% of patients develops PCa recurrence and requires further treatments [48–50]. Since PCa cell proliferation is dependent on androgen signaling, androgen deprivation therapy, either by chemical or surgical castration, is the first-line

treatment for advanced PCa [51]. Although this therapy is initially highly effective in most of the patients, in some cases the tumor evolves into an androgen independent form, transition that may occur through several mechanisms that are not yet completely understood [52]. The androgen independent form of PCa currently lacks efficacious therapeutic options [53] and therefore, in this context, immunotherapy represents a highly promising new treatment approach. Over the last few years, numerous pre-clinical and clinical studies have been performed to develop and test different PCa immunotherapies [54; 55]. A main achievement has been the FDA approval of *sipuleucel-T*, so far the only approved immunotherapy for PCa treatment [51]. Compared with other types of cancer, PCa is relatively insensitive to the most popular immunotherapies and additional studies are needed to understand the mechanisms underlying this lack of immune responsiveness [56; 57].

It has been shown that the PCa is able to evade the immune surveillance by several mechanisms [58; 59]. One of these is the expression of particular ligands called immune checkpoints that, recognized from T cells, can inactivate the latter, such as the Programmed Death-Ligand 1 (PD-L1) and the Cytotoxic T-Lymphocyte Antigen 4 (CTLA4). In detail, the PD-L1 on the tumor cell membranes binds its Programmed cell Death protein 1 receptor (PD-1) exposed on the CTL, inhibiting their expression. On the other hands, the tumor also stimulates the proliferation of the Antigen Presenting Cells (APCs) expressing B7 ligands, which bind with the CTLA4 on the CTLs. These complex mechanisms imply the suppression of the CTL immune reaction. Current studies are investigating on the therapeutic effect of Immune Checkpoint Blockade (ICB) drugs, that have been recently approved by FDA for the treatment of some solid tumors [60]. A combination of ICB involving anti-CTLA4 and anti-PD-L1 drugs is currently under phase II clinical trial for PCa (NCT03061539, NCT02985957). The PCa also stimulates the production of immune cells responsible for immune system regulation, mainly Regulatory T cells (Tregs) [58; 61] and Myeloid-Derived Suppressor Cells (MDSCs) [62–64]. Figure 0.1 summarizes the described immune-suppression mechanisms in the tumor microenvironment.

This dissertation presents two mathematical models of PCa developed during my PhD studies. Both models are calibrated by using experimental data from the literature and they are employed

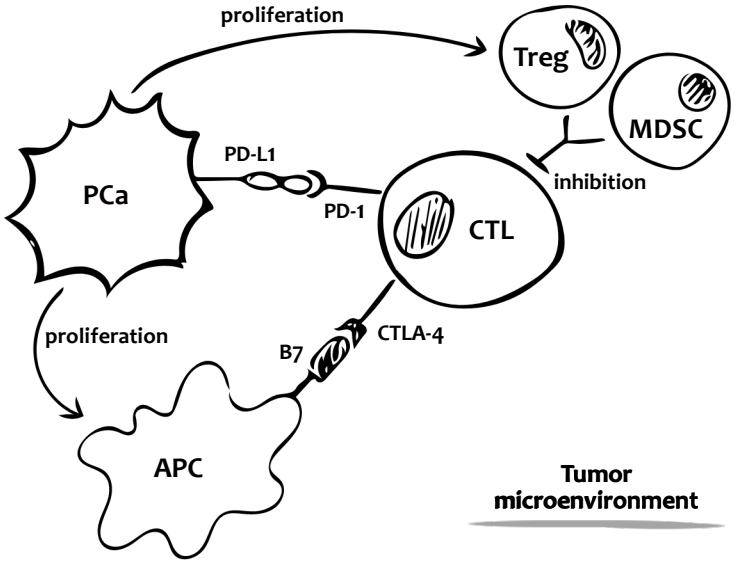

Figure 0.1: Immuno-suppressive tumor microenvironment. Schematic representation of the immune-suppression induced by the prostate cancer. This tumor promotes the proliferation of immunosuppressive cells in the tumor microenvironment and inactivates the CTLs by the expression of immune checkpoints.

to evaluate the effects of the therapies implemented. The two models describe the PCa progression in case of mice and humans, and they are developed and analyzed by different techniques.

The thesis is organized as follows:

Chapter 1 includes the mathematical background necessary for the development and the analysis of the mathematical models presented in the following chapters. This section starts describing system biology and the main mathematical modeling approaches. Then, a summary of the theory of ordinary differential equations is presented. In particular, the main theorems in this field and the qualitative behavior analysis are introduced. Moreover, this chapter comprises a brief overview of the model calibration techniques and an hint of *a priori* and *a posteriori* analyses used for validating mathematical models.

Chapter 2 presents the QSP model of murine PCa. The model is accurately described by its diagram and equations, with a detailed explanation of the single terms. We present the model simulations for the experimental scenarios used to calibrate the model and we discuss the results showing the corresponding data fits. After having verified the reproducibility of the experimental

data, we use the model to identify the most effective combination therapy by considering both the model-predicted tumor reduction and the synergy between treatments. In particular, we emphasize the androgen deprivation therapy as leading treatment and we provide a decision tree as tool for choosing the best protocol to treat castrated subject. The content of this chapter is going to be published on *Scientific Reports* journal.

Chapter 3 is dedicated to the human PCa model, which represents a step forward in the direction of the mathematical description of human prostate cancer. The description of tumor-immune interactions is less detailed than the models presented in the Chapter 2, but it is due to the paucity of human data in the literature. The model diagram and equations are presented and discussed in detail. The goal of this work is to analyze the steady states and their stability in relation to the tumor proliferation rate, which is patient specific. To this aim, we reduce the model to obtain a three-dimensional Limiting System (LS), and we study the stability of LS equilibrium points with and without immunotherapies. Most of the results presented in this chapter has been included in a paper submitted for publication in a scientific journal.

Chapter 4 is devoted to a final discussion. In this chapter we summarize the main results and limitations of this dissertation, biologically discussing the presented mathematical outcomes.

Chapter 1

Mathematical modeling and system biology: backgrounds

System biology is a discipline that provides mathematical descriptions of complex biological systems [65]. During the last decades, the interest in this interdisciplinary approach considerably increased, determining several progresses in biology [66]. Indeed, comprehensive mathematical models can help in understanding biological processes, since they describe complex systems by a collection of few variables. The mathematical description of biological systems has several advantages. First of all, mathematical models provide schematic representations, which, compared to the described biological phenomena, are much easier to study [67]. Moreover, unexpected model results can give an indication that some essential factors were ignored, contributing to the comprehension of unknown underlying mechanisms, as well as discovering biological misinterpretations [68]. In addition, mathematical models predict the evolution of the biological system, and, then, can determine how much perturbations in the model affect the dynamics. This model capability can be used to evaluate the predicted system behavior in case of mutations or drug administrations [69], supporting the pharmaceutical industry in discovering new strategies for drug development or in designing possible experiments [70; 71].

It is essential to notice that a mathematical model is an abstract representation of a bio-

logical process, therefore many different mathematical models can be developed for the same phenomenon. Each model can be suitable, depending on the information that we want to extrapolate from it. For this reason, to obtain a reasonable description of the biology, before developing a mathematical model, we need to define the properties of the system that we want to investigate.

Dynamic mathematical models form a collection of interacting variables, and they represent the most widely used mathematical approaches in system biology [72]. Dynamic systems can be described by deterministic or stochastic methods. The behavior of deterministic models depends on the initial condition, *i.e.* the initial state of the model variables, and can be described by systems of ordinary or partial differential equations. Those models present several benefits. Indeed, they are exactly and easily reproducible under the same conditions and, even if the model cannot be explicitly solved, the solutions can be efficiently approximated by numerical methods. On the contrary, a stochastic representation changes according to specified conditions and random laws, since the variable state is determined by a probability distribution. Given the intrinsic random nature of the biological phenomena, stochastic mathematical models often represent an accurate description of the biology., but their numerical cost can be very high. Therefore, for high-dimensional systems, a stochastic representation is not feasible. Hence, the choice on the type of model depends on the nature of the biological problem and the questions one wants to address. For further details on the differences between these two mathematical modeling techniques see [73].

In this thesis, we present two deterministic mathematical models in form of ordinary differential equation. Hence, as a matter of clarity, in the following section, we propose a brief overview of the main concepts and results from this mathematical field.

1.1 Basis of Ordinary Differential Equations

In this section we introduce the basis of the Ordinary Differential Equation (ODE) theory, the mathematical tool that we used to develop the models presented in this dissertation. Since we include only the main results in this field, for more details we refer to [74–76]. In the context of

system biology, a system of ODEs describes the evolution in time of the variables included in the model; therefore a typical system of n first-order ODEs can be written as:

$$\frac{dx}{dt}(t) = F(x(t), t), \tag{1.1}$$

where $x = (x_1, x_2, ..., x_n) \in \mathbb{R}^n$ and $F = (F_1, F_2, ..., F_n)$ is a vector field such that

$$\begin{aligned} F : Dom(F) \subseteq \mathbb{R}^n \times \mathbb{R}^+ &\longrightarrow \mathbb{R}^n \\ (x, t) &\longrightarrow F(x, t) \end{aligned}$$

Observation 1. We note that a k-order ODE $\frac{d^k y}{dt^{(k)}} = f(y, \frac{dy}{dt}, \frac{d^2 y}{dt^2}..., \frac{d^{(k-1)} y}{dt^{(k-1)}}, t)$ can be expressed as a first-order ODE system by the substitution: $y = x_1$, $\frac{dy}{dt} = x_2$, ..., $\frac{d^{(k-1)} y}{dt^{(k-1)}} = x_n$, obtaining the system (1.1).

A solution of (1.1) is a differentiable function $x(t) : \mathbb{R}^+ \to \mathbb{R}^n$, which satisfies the condition (1.1), and such that (x, t) is in the domain of F, for every $t \in \mathbb{R}^+$. Given a solution of the system (1.1), this is invariant for translation. Indeed, if x is a solution, also $x + k$, with $k \in \mathbb{R}$, is a solution of the same ODE system.

The solution can be uniquely determined for a Cauchy problem, which is composed by a system of ODEs coupled with an initial condition:

$$\begin{cases} \frac{dx}{dt}(t) = F(x(t), t) \\ x(t_0) = x_0 \end{cases} \tag{CP}$$

In this case the invariance for translation does no longer hold, since the solution $x(t)$ must satisfy the initial condition $x(t_0) = x_0$.

The main result of the ODE theory is the theorem of existence and uniqueness of the ODE system solution. Before introducing this theorem, we define the Lipschitz condition.

Definition 1. (Local Lipschitz condition) A function $f : Dom(f) \subseteq \mathbb{R}^n \times \mathbb{R}^+ \to \mathbb{R}^n$ is locally

Lipschitz with respect to the variable x if $\forall K \subseteq Dom(F)$, compact set, $\exists L \in \mathbb{R}, L > 0$ such that

$$||f(x,t) - f(y,t)|| \leq L||x - y||,$$

$\forall (x,t),(y,t) \in K$. In this case, we write $f \in Lip^x_{loc}(Dom(f))$.

This definition can be extended to a global condition:

Definition 2. (Global Lipschitz condition) A function $f : Dom(f) \subseteq \mathbb{R}^n \times \mathbb{R}^+ \to \mathbb{R}^n$ is globally Lipschitz with respect to the variable x if $\exists L \in \mathbb{R}, L > 0$ such that

$$||f(x,t) - f(y,t)|| \leq L||x - y||,$$

$\forall (x,t),(y,t) \in Dom(f)$. In this case, we write $f \in Lip^x(Dom(f))$.

In other words, a function is globally Lipschitz if the constant L does not depend on the compact subset of the function domain. This condition means that the function f is limited in how fast it can change, since its increments are limited by the Lipschitz constant L. The Lipschitz condition of the vectorial field F ensures the uniqueness of the solution of an ODE system, as stated in the following result..

Theorem 1. ***(Local existence and uniqueness)*** *Let us consider the Cauchy problem (CP), with F continuous function such that $F \in Lip^x_{loc}(Dom(F))$. Then, $\forall (x_0,t_0) \in Dom(F)$ $\exists$ $I_{t_0} \subseteq \mathbb{R}^+$, neighborhood of the initial point t_0, in which there exists $x \in C^1(I)$ unique solution of (CP).*

When the local existence and uniqueness theorem is satisfied, the local solutions of the (CP) can be extended.

Definition 3. (Extended solution) Let $u : I_{t_0} \subseteq \mathbb{R}^+ \to \mathbb{R}$ and $w : J_{t_0} \subseteq \mathbb{R}^+ \to \mathbb{R}$ be solutions of (CP), where I_{t_0} and J_{t_0} are neighborhoods of the initial point t_0. The solution w is an extension of the solution u if $I_{t_0} \subseteq J_{t_0}$ and $w(t) = u(t)$ for $t \in I_{t_0}$.

Definition 4. (Maximal solution) A solution $x(t)$ of (CP) is called maximal if it has no extensions.

Now we can introduce the global existence and uniqueness theorem.

Theorem 2. ***(Global existence and uniqueness)*** *Let us consider the Cauchy problem (CP), with F continuous function such that $F \in Lip^{x}_{loc}(Dom(F))$. If there exists a constant $k > 0$ such that:*

$$||F(x,t)|| \leq k(||x|| + 1),$$

$\forall (x,t) \in Dom(F)$, therefore every maximal solution of (CP) is global, i.e. the solution $x(t)$ is defined $\forall t \in \mathbb{R}^{+}$.

A vector field that is not explicitly dependent on time, i.e. F (x (t), t) = F (x (t)), is called autonomous. Since all the models presented in this thesis are autonomous, in the following we refer to the vector field F as $F(x(t))$.

1.1.1 Qualitative analysis of ODE systems

In many cases an explicit solution of an ODE system can not be determined. Therefore, the system can be solved by numerical approximations or, alternatively, the properties of the field F can be studied for understanding the qualitative behavior of the solution of the ODE system.

Definition 5. (Equilibrium point) A point $\overline{x} \in \mathbb{R}^n$ is an equilibrium point for the system $\frac{dx}{dt} = F(x)$ if $F(\overline{x}) = 0$.

Therefore, $x(t) = \overline{x}$ represents a steady state of the system, since the derivative $\frac{dx}{dt}(\overline{x}) = 0$.

Definition 6. Stable equilibrium point. An equilibrium point $\overline{x}$ is stable if $\forall$ $I_{\overline{x}}$ neighborhood of $\overline{x}$, there is a subset U such that the solutions $x(t)$ satisfying the initial condition $x(t0) = x0$ in U remain in $I_{\overline{x}}$, $\forall t > 0$.

Definition 7. Attractive equilibrium point. An equilibrium point $\overline{x}$ is stable if $\forall I_{\overline{x}}$ neighborhood of $\overline{x}$, there is a subset U such that the solutions $x(t)$ starting from $x_0 \in U$ converge to $\overline{x}$.

Definition 8. Asymptotically stable equilibrium point. An equilibrium point $\overline{x}$ is asymptotically stable if it is stable and attractive.

Given a non-linear autonomous ODE system as

$$\frac{dx}{dt} = F(x), \tag{1.2}$$

it can be shown that the behavior of the solutions around the equilibrium point $\overline{x}$ for long times can be determined by studying the linearized corresponding system:

$$\frac{dx}{dt} = DF(\overline{x}) \cdot x, \tag{1.3}$$

where $DF(\overline{x})$ is the Jacobian matrix of the field F evaluated in $\overline{x}$. We do not provide a proof of this result. For major information we refer to [74].

Theorem 3. *Let $F \in C^1(Dom(F))$, being $Dom(F)$ an open subset of $\mathbb{R}^n$. Let $\overline{x} \in Dom(F)$ be an equilibrium point. If the real part of all the eigenvalues of the matrix $DF(\overline{x})$ is negative, the equilibrium point $\overline{x}$ of the system (1.2) is asymptotically stable. On the other hands, if there is at least one eigenvalue of the matrix $DF(\overline{x})$ with positive real part, the equilibrium point of the system (1.2) is unstable.*

The study of the linearized system provides information on the local behavior of (1.2) when the real part of the eigenvalues of $DF(\overline{x})$ is different from zero, but it does not provide any information about the basin of attraction of a steady state.

In some cases, the stability or the presence of a steady state may depend on the model parameter values. When the system behavior changes for small variation of one or more parameters,

this system presents a bifurcation. There are many types of bifurcations, but, in this thesis, we include only the saddle-node, the transcritical and the Hopf bifurcations.

Saddle-node bifurcation. When as a consequence of varying a parameter there is a creation or a disruption of an equilibrium point, there is a saddle-node bifurcation. The equation

$$\frac{dx}{dt} = F(x, \alpha) = x^2 - \alpha \tag{1.4}$$

represents the simplest example of the saddle-node bifurcation in one dimension. Indeed, as shown in Figure 1.1, by changing the parameter α the system presents:

(i) two equilibrium points for $\alpha > 0$, one stable $\overline{x}_1 = -\sqrt{\alpha}$ and one unstable $\overline{x}_2 = +\sqrt{\alpha}$;

(ii) a bifurcation point for $\alpha = 0$, which is generated by the collapse of the two equilibrium points in one steady state preserving the stability and instability properties of the two equilibria together;

(iii) no steady states for $\alpha < 0$.

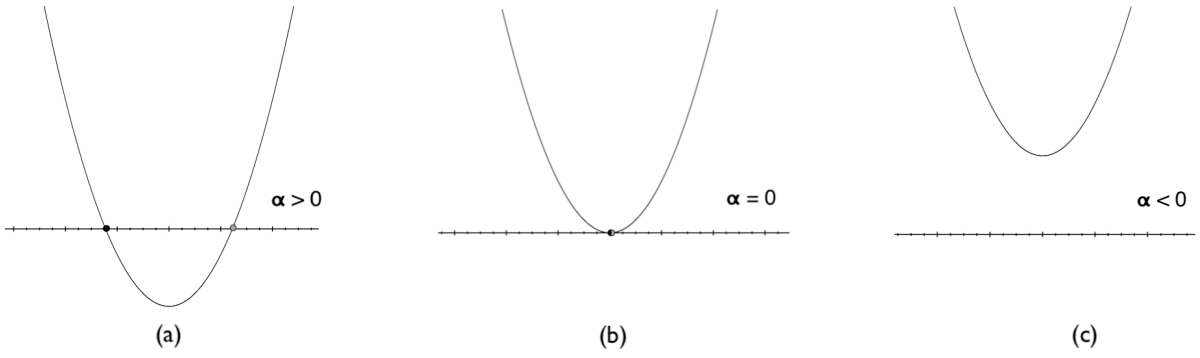

Figure 1.1: Graphical representation of the saddle-node bifurcation. Different system behaviors appear as a function of the parameter α. (a) for $\alpha < 0$ the system has two equilibria, one stable (black point) and one unstable (grey point). (b) for $\alpha = 0$ the two equilibium points collapse in a unique equilibrium. (c) for $\alpha > 0$ the system does not present equilibrium points.

Transcritical bifurcation. When by changing a parameter the stability of an equilibrium point varies, there is a transcritical bifurcation. The simplest example of this bifurcation in one dimension is given by the equation

$$\frac{dx}{dt} = F(x, \alpha) = x(\alpha - x). \tag{1.5}$$

Indeed, as shown in Figure 1.2, by changing the parameter α the system presents:

(i) two equilibrium points for $\alpha > 0$, one unstable $\overline{x}_1 = 0$ and one stable $\overline{x}_2 = \alpha$;

(ii) a bifurcation point for $\alpha = 0$, which is generated by the collapse of the two equilibrium points in one steady state preserving the stability and instability properties of the two equilibria together;

(iii) two equilibrium points for $\alpha < 0$, one stable $\overline{x}_1 = 0$ and one unstable $\overline{x}_2 = \alpha$;

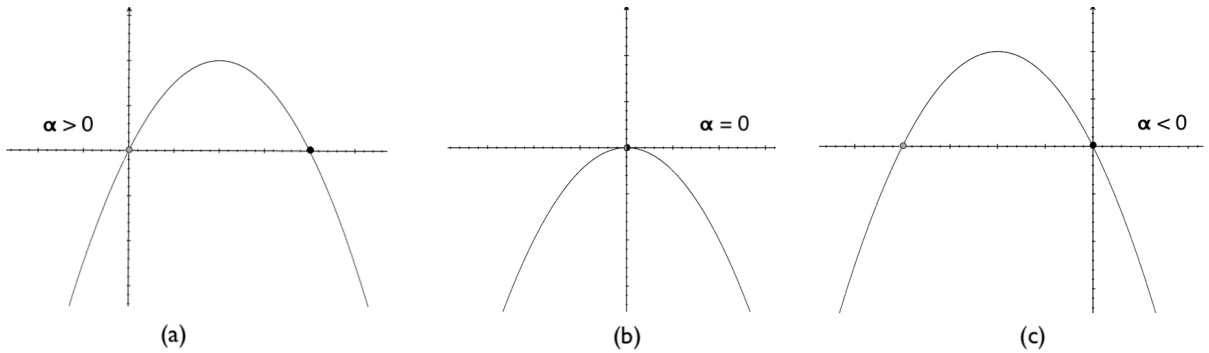

Figure 1.2: Graphical representation of transcritical bifurcation. Different system behaviors appear as a function of the parameter α. (a) for $\alpha > 0$ the system has two equilibria, one unstable (grey point) and one stable (black point). (b) for $\alpha = 0$ the two equilibium points collapse in a unique equilibrium. (c) for $\alpha < 0$ the system has two equilibrium points, one stable (black point) and one unstable (grey point).

Hopf bifurcation. The Hopf bifurcation is characterized by the variation of the stability of an equilibrium point and the formation of a limit cycle associated to the variation of a parameter. This bifurcation is connected to periodic solutions and it can be either subcritical or supercritical.

In the first case, starting from a stable point, the variation of a parameter generates an unstable limit cycle, in the second case, from an unstable equilibrium point the variation of a parameter generates a stable limit cycle.

The qualitative analysis of our model of human prostate cancer provided in Chapter 3 shows the presence of two of these bifurcations. The steady states of the model have been analyzed by the Mabtlab toolbox Matcont [77], which labels with Branching Point the transcritical biforcation, while the saddle-node bifurcation is called Limit Point.

1.2 Model calibration and optimization algorithms

Mathematical models depend on the parameter estimates. Therefore, the general formulation of a model can be expressed as

$$\frac{dx}{dt}(t, p_1, \ ..., \ p_m) = F(x(t, p_1, \ ..., \ p_m)), \tag{1.6}$$

where $x \in \mathbb{R}^n$ and p_1, ..., p_m are the model parameters.

The model parameters require to be estimated. The calibration of the models presented in this thesis has been performed by considering literature values or by using optimization algorithms to fit experimental data. For this reason, in this section we present the main strategies for model calibration, with particular emphasis on those used for our research scopes.

All the optimization methods aim at finding the best solution satisfying specific criteria. In our work, we used the optimization techniques to estimate model parameters. In all our cases, the optimization problem was to minimize a function, called objective function, by varying the input in the parameter space. The objective function used for our model calibrations have been created by considering the differences between the output of the model and experimental data taken from the literature. The procedures are reported in the following chapters, in the 2.2 and 3.2 subsections. Once fixed the objective function, the choice of the algorithm for the model calibration can be crucial, since it influences the outcomes and then the parameter setting. There

are many optimization algorithms, which can be classified in several ways, depending on what we are considering. For example it is possible to classify the algorithms as constrained or non-constrained, as iterative or heuristic, as deterministic or stochastic, and so on. For an overview of the available options we refer to [13; 78–82].

In our works we used an iterative gradient-based method and a genetic algorithm, then we focus on these two different algorithms for optimization problems. The main differences between these two approaches are the exploration of the parameter space and the strategy to select the minimum of the objective function.

Gradient-based methods. The gradient-based methods explore the parameter space by following the gradient of the objective function. These iterative algorithms need an initial point. Starting from a fixed initial parameter set, it always returns the same result, which corresponds to the minimum of the objective function. The main limitation of this approach is that the resulting parameter set could be associated to a local minimum of the objective function and it might not represent the best solution of the optimization problem. A possible way to bypass this issue is to implement a multi-start strategy, which generates random starting points, allowing a more effective exploration of the parameter space. However, for particularly complicated objective functions it should not be sufficient to avoid the convergence to local minima. Given the complexity of the objective function and the high dimension of the parameter space of the model presented in the Chapter 2, for the model calibration of that model we followed the genetic approach.

Genetic algorithms. This type of algorithms are inspired by nature genetic processes. By fixing the population size, these methods explore the parameter space, considering random parameter sets as member of this population and evaluate the objective function corresponding to the different inputs. Among these, the algorithm selects the best one and recombine the other strings of parameters by crossover, recombination and random mutations, generating the next population. This stochastic approach allows a good exploration of high-dimensional parameter

spaces, avoiding the possibility to remain in a local minimum of the objective function. However, the implementation of genetic algorithms requires a lot of time. In this sense, the choice of the population size is essential, since a small population gives a fast implementation, but the solution could be not optimal, while a large population better explores the parameter space, but the time of convergence increases.

1.3 Identifiability and sensitivity analyses

Once a parameter set has been identified to fit the experimental data by a mathematical model, it is important to understand the reliability of these estimates and how the parameter values influence the system dynamics. For this reason the analyses of parameter identifiability and sensitivity have to be performed, especially when there are a lot of parameters that need to be estimated by using data coming from different sources, as in the model presented in Chapter 2. These analyses increase the confidence in the model predictions, and therefore they are essential to discuss the results from a biological point of view.

Identifiability analysis. The parameter identifiability analysis establishes if there exists one or more possible sets of parameter estimates for a given model fitting a user provided amount of experimental data. Parameter identifiability can be considered as a property of the defined mathematical system. In this case, the parameter identifiability depends on the model structure, and it can be performed by considering information such as the experimental data used for the fitting, the variables and their relations, the whole set of parameters and the ones that have to be estimated [83].

If the analysis predicts that the parameters are identifiable, the identifiability can be either global or local. In the first case, it means that there exists a unique possible set of parameters, while, in the second case there are more than one reasonable parameter sets. On the other hands, if the analysis predicts a non-identifiability, this problem could be solved by parameter substitution or analytical manipulation of the model. We performed an *a-priori* identifiability analysis for

the model presented in Chapter 2, by using GenSSI [84], a Matlab toolbox that evaluates the structural identifiability of a model by using Lee derivatives. To further information we refer to [85].

When the analysis of the identifiability includes the parameter estimates, it is *a posteriori* investigation, which can be performed by the sensitivity analysis.

Sensitivity analysis. The analysis of the model sensitivity to the parameter estimates evaluates how much the parameter uncertainty influences the model results [86]. This analysis can be local, if it explores only a neighborhood of the parameter estimate, or global, if the entire parameter space is investigated. Essentially, during the sensitivity analysis, the parameter values are modified in order to examine the impact of these perturbations on the model outcomes.

The Local Sensitivity Analysis (LSA) studies the changing on model dynamics caused by local perturbations of the parameters. Therefore, if $X = x_i$ is the i-th variable of the system (1.6), and p a given parameter, the value of LSA is defined as:

$$LSA = \frac{\partial X(t,p)}{\partial p}. \tag{1.7}$$

The impact of the perturbation of a parameter p on the variable X is described by this value: higher the LSA value is, greater is the impact of parameter perturbations.

In our work, we performed the LSA using a logarithmic LSA [87]:

$$LSA = \frac{\partial log(X(t,p))}{\partial log(p)} = \frac{\frac{1}{X(t,p)}\partial X}{\frac{1}{p}\partial p} = \frac{\partial X(t,p)}{\partial p}\frac{p}{X(t,p)}. \tag{1.8}$$

The Global Sensitivity Analysis (GSA), instead, investigates how much the model predictions can be influenced by global parameters changing. To this scope, the parameter space needs to be sampled by generating k random parameter sets. For each parameter set, LSA have to be performed. Thus, the process returns a matrix $A \in \mathbb{R}^{k\times m}$, where m is the number of the model parameters, and the element a_{ij} represents the LSA value corresponding to the i-th set and the j-th parameter. From the matrix A, one aims at obtaining a unique GSA value for each parameter.

In order to do this, one can use different statistics, such as the average LSA, the median LSA or the maximum LSA value for each parameter.

For further information about the sensitivity analyses performed to validate our mathematical models we refer to Sections 2.5 and 3.7.

Chapter 2

A QSP model of prostate cancer immunotherapy in mice

In this chapter we propose a QSP model of prostate cancer that extends a previous one published by Peng *et al.*[23] based on data from a murine Pten prostate cancer model [88; 89].

Although Peng and coworkers already described the action of CTLs, dendritic cells, Tregs, androgens and interleukin-2 (IL-2) in the tumor microenvironment, we extended the characterization of the immune system by including MDSCs and Natural Killer (NK) cells as potential targets for new prostate cancer therapies. Indeed, since the PCa does not highly respond to several immunotherapies, evaluating combination therapies is an important step to improve therapeutic benefits [90]. Therefore, the main goal of this work is to provide a mathematical model able to test the efficacy of several immunotherapies and their combinations. We incorporate a wide range of experimental data from literature [23; 64; 91–93] to implement seven treatments. The efficacy of the therapies is assessed considering the model-predicted tumor inhibitory effect and the synergy of combination therapies. Synergy between treatments, indeed, plays a crucial role from a clinical point of view, since it allows the reduction of the drug doses maintaining a satisfactory overall treatment efficacy, and improving patients' quality of life [94].

The text in the following chapter is mainly taken from the work *"A QSP model of prostate can-*

cer immunotherapy to identify effective combination therapies", which is currently in the process of publication on *Scientific Reports* journal. The corresponding model limitations are discussed in the final Chapter 4.

2.1 Mathematical model

Starting from the model introduced by Peng *et al.*[23], we built a mathematical model based on ODEs describing the prostate cancer and its interaction with the immune system. A graphical representation of the model variables and their regulative effects is shown in Figure 2.1.

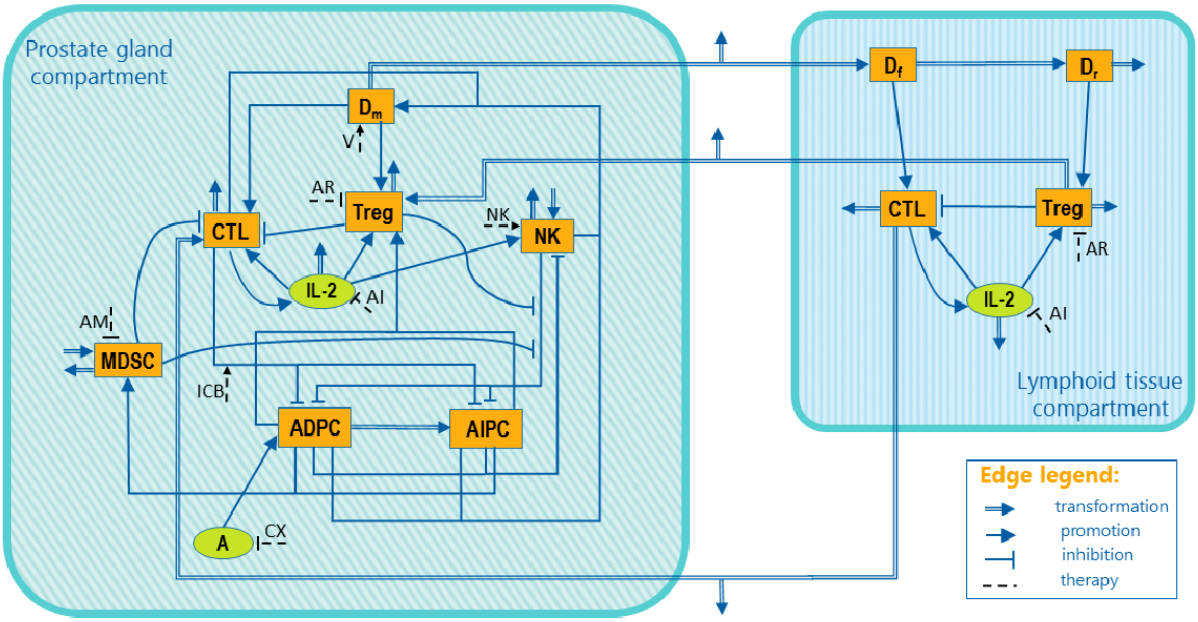

Figure 2.1: Mouse PCa model diagram. The model is composed of two compartments: prostate gland and lymphoid tissue. Cells are represented in orange squared boxes, while molecules in green rounded ones. In the prostate gland compartment the cancer is in its two forms: Androgen Dependent Prostate Cancer (ADPC) and Androgen Independent Prostate Cancer (AIPC). Other players involved: mature Dendritic cell (Dm), regulatory T cell (Treg), Myeloid-Derived Suppressor Cell (MDSC), Cytotoxic T Lymphocyte (CTL), Natural Killer cell (NK), functional Dendritic cells (Df), regulatory Dendritic cells (Dr), Androgen (A) and Interleukin-2 (IL-2). Double arrows represent transformations, single lines represent promotions and inhibitions, while dashed lines depict the seven implemented treatments. A complete description of the treatments and the corresponding abbreviations are reported in Table 3.1.

The model has two compartments: the prostate gland and the lymphoid tissue. The prostate gland compartment includes Androgen Dependent (ADPC) and Independent (AIPC) Prostate Cancer cells. While the ADPC grows in the presence of androgens, under androgen deprivation therapy ADPC cells undergo apopotosis. However, the low androgen level leads to the AIPC proliferation. ADPC and AIPC cell expansion is counteracted by the activation of the host immune system. NK cells and CTLs have been included as the major effectors of the innate and adaptive immune response, respectively. NK and CTL killing activity is counteracted by Tregs and MDSCs, immune cells promoting immune tolerance. In addition, IL-2 has been included into the model as a key signaling molecule promoting the proliferation of CTLs, NK and Treg cells. The lymphoid tissue compartment includes variables representing biological processes of the prostate draining lymph nodes and the spleen. Within this compartment, functional (Df) and regulatory (Dr) dendritic cells activate CTLs and Treg cells, respectively. The two compartments communicate by exchanging dendritic cells, CTLs and Tregs. In addition, the model incorporates 7 different treatments, shown with dashed lines in Figure 2.1 and summarized in Table 3.1.

In total, the model is composed of 19 ODEs, which describe the dynamics of 14 variables related to the tumor and the immune system, and 5 treatment-related variables. It is worth noting that the androgen deprivation therapy (CX) and the infusion of NK do not have an equation describing their behaviour. The androgen deprivation is included in the model as a term of the Eq. (2.11), while the infusion of NK is implemented by changing the initial condition of NK cells. Compared with the starting model[23], our extended version includes two additional variables describing the tumor microenvironment (NK cells and MDSC) and two variables related to the treatment: the immune checkpoint blockade (ICB) and the MDSC-targeted therapy (AM). Moreover, the original equations have been extended to take into account the action of the new players. Each variable is expressed as a ratio between its current value and its initial value. The model equations are described in the following subsections, while the model parameters are reported in Table 2.3.

Therapy	Abbreviation	Description	Reference
castration	CX	androgen deprivation within the prostate gland	[23]
vaccine	V	administration of mature dendritic cells into the prostate gland	[23]
anti-IL2	AI	administration of monoclonal antibodies neutrali zing IL-2 within the prostate gland and the lymphoid tissue	[23]
anti-Treg	AR	Treg depletion within the prostate gland and the lymphoid tissue through anti-CD25 antibody injection	[23]
NK cells	NK	administration of NK cells within the prostate gland implemented by increasing the initial condition of NK	[95]
Immune checkpoint blockade	ICB	an intermittent therapy with a cocktail of anti-CTLA4 and anti-PD1 antibodies administered three times per week, for 4 weeks, starting 21 days after androgen deprivation therapy	[93]
anti-MDSC	AM	an intermittent therapy with anti-MDSC drugs (Cabozatinib) daily administered for 4 weeks, starting 21 days after androgen deprivation therapy	[93]

Table 2.1: Table of the treatments for mouse PCa model. Summary of the treatments implemented in the mathematical model.

Prostate gland compartment

The prostate gland compartment contains prostate cancer cells (ADPC and AIPC), immune system cells (Dm, CTL, NK, Treg and MDSC), androgens and IL-2.

$$\frac{dX_1}{dt} = \underbrace{r_{p1}\ A\ X_1}_{\text{proliferation}} \underbrace{-\ \mu_1\ (1\ -\ A)\ X_1}_{\text{death}} \underbrace{-\ r_M\ (1-A)\ X_1}_{\text{mutation}} \underbrace{-\ k_{CX}\ (1\ +\ \delta_{ICB}\ I_{CB})\ C_2\ X_1}_{\text{tumor killing by CTL}} \tag{2.1}$$

$$\underbrace{-k_{NX}(e^{-k_{RN}R_2} + e^{-k_{MN}M})\ N\ X_1}_{\text{tumor killing by NK}}. \tag{2.2}$$

The Eq. (2.1) refers to the ADPC cells. Tumor cell proliferation is positively regulated by the androgen presence, while tumor death and mutation are negatively affected by it. We assume that the evolution to AIPC occurs after androgen deprivation therapy, as a selective pressure is applied ("mutation" term). A key mechanism exploited by the tumor to evade the immuno-surveillance is the immune checkpoint activation, which reduces the CTL tumor-killing capacity [18]. ICB treatments are used to restore the T cell effector functions [96]. In our model, this biological process is described by the linear function $1 + \delta_{ICB}\ I_{CB}$ in the "tumor killing by CTL" term, in which the I_{CB} represents the amount of ICB drug (Eq. (2.21)). This function increases the value of the CTL killing capacity (k_{CX}) when the treatment is administered. The "tumor killing by NK" term depends on a multiplicative function of Treg (R_2) and MDSC cells (M)[97]. Following the approach of De Pillis *et al.*[21], this inhibition has been modeled by a sum of two negative exponential terms, which becomes close to zero when the amount of Treg or MDSC increases.

$$\frac{dX_2}{dt} = \underbrace{r_{p2}\ X_2}_{\text{proliferation}} \underbrace{-\ \mu_2\ X_2}_{\text{death}} \underbrace{+\ r_M\ (1\ -\ A)\ X_1}_{\textit{mutation}} \underbrace{-\ k_{CX}(1\ +\ \delta_{ICB}\ I_{CB})\ C_2\ X_2}_{\text{tumor killing by CTL}} \tag{2.3}$$

$$\underbrace{-\ k_{NX}(e^{-k_{RN}R_2} + e^{-k_{MN}M})\ N\ X_2}_{\text{tumor killing by NK}}. \tag{2.4}$$

The Eq. (2.3) describes the evolution in time of the AIPC cells. The terms of this equation are similar to the ones described above, except for proliferation and death terms, no longer androgen (A) dependent.

$$\frac{dD_m}{dt} = \underbrace{a_{VD}\ V}_{\text{vaccine}}\ \underbrace{-\ m_D D_m}_{\text{migration}} \tag{2.5}$$

$$\underbrace{+\ a_{XD}\ (\ \mu_1(1-A)\ X_1\ +\ \mu_2\ X_2\ +\ k_{CX}\ (1+\delta_{ICB}\ I_{CB})\ C_2\ (X_1+X_2)}$$

$$\underbrace{+\ k_{NX}(e^{-k_{RN}R}+e^{-k_{MN}M})\ N\ (X_1+X_2))}_{\text{recruitment by tumor}}$$

The mature dendritic cells are described in the Eq. (2.5). The amount of dendritic cells increases when the vaccine (V) is administered, as described by the vaccine term. The variable V is 1 when vaccine is administered, 0 otherwise. The migration term represent the fraction of activated dendritic cells (D_m) that move to the lymphoid tissue compartment (D_f and D_r). The dendritic cell recruitment and activation occur within the inflammation site over tumor apoptosis [98; 99], as described by the recruitment term.

$$\frac{dC_2}{dt} = \underbrace{a_{DC}\ D_m}_{\substack{\text{activation}\\ \text{by } D_m}}\ \underbrace{+\ a_{IC}\ \frac{C_2\ I_2}{s_I\ +\ I_2}}_{\substack{\text{stimulation}\\ \text{by IL-2}}}\ \underbrace{+\ p_C\ m_C\ C_1}_{\text{migration}}\ \underbrace{-\ k_{RC}\ R_2\ C_2\ -\ k_{MC}\ M\ C_2}_{\text{inhibition by Treg and MDSC}}\ \underbrace{-\ \mu_C\ C_2}_{\text{death}}. \tag{2.6}$$

The Eq. (2.6) describes the dynamics of the CTLs, which are activated by dendritic cells (D_m) and IL-2 (I_2)[24]. A fraction of CTLs migrates out from lymphoid tissue and reaches the prostate gland with a probability p_C here set to 0.5[23], as described by the "migration" term. The equation takes into account the effect of the immune-suppressive tumor microenvironment, here represented by the "inhibition by Treg and MDSC" term, and the CTL physiological cell death, as a negative regulation of CTL dynamics.

$$\frac{dN}{dt} = \underbrace{\rho_N}_{\text{source}} \underbrace{- \mu_N\ N}_{\text{death}} \underbrace{- k_{XN}\ N(X_1 + X_2)}_{\text{inhibition}} \underbrace{+ a_{IN}\frac{N\ I_2}{s_N + I_2}}_{\text{stimulation by IL-2}} . \tag{2.7}$$

The Eq. (2.7) describes the NK cells dynamics. The source ρ_N has been estimated by imposing a steady state when the tumor is not present ($X_1+X_2 = 0$), assuming NK cells are not proliferating in absence of tumor-related inflammation. If we impose NK cells as constant, *i.e.* $\frac{dN}{dt} = 0$, $N(0) = 1$ and $X_1 + X_2 = 0$, we obtain:

$$\rho_N = \mu_N - \frac{a_{IN} I_2}{s_N + I_2}.$$

Given the values of a_{IN} and s_N (Table S1), the μ_N parameter results as $\mu_N >> \frac{a_{IN} I_2}{s_N + I_2}$, which leads to $\rho_N \approx \mu_N$.

For evaluating the death rate μ_N, part of the death term, we followed the method used in de Pillis *et al.*[21], where the authors considered the turnover rate of NK cells being inversely proportional to the term $\sqrt[4]{m}$, where m is the body mass of the organism:

$$\mu_N = \frac{K}{\sqrt[4]{m}}.$$

By considering the value of K provided in the de Pillis *et al.*[21] and by computing the mouse average mass[100; 101], we defined:

$$\mu_N = \frac{0.0371}{\sqrt[4]{m_{mice}}} = 0.09 \ \ day^{-1}.$$

The other terms of the equation describe regulatory mechanisms exerted by tumor and NK cells. Specifically, the "inhibition" term indicates NK inactivation after interaction with ADPC and AIPC, since PCa has the ability to impair NK cell function, establishing a strong immunosuppressive environment[102; 103]. Moreover, PCa development has been associated with NK cell reduction[104]. The "stimulation by IL-2" term, instead, is the promotion exerted by IL-2 on NK cell proliferation [102; 105] within the prostate gland compartment.

$$\frac{dR_2}{dt} = \underbrace{a_{DR}\, D_m}_{\substack{\text{production}\\ \text{by } D_m}} \underbrace{+\, a_{IR}\, I_2}_{\substack{\text{stimulation}\\ \text{by IL-2}}} \underbrace{+\, p_R\, m_R\, R_1}_{\text{migration}} \underbrace{+\, a_{XR}\, (X_1 + X_2)}_{\text{activation by tumor}} \underbrace{-\, \mu_R\, R_2}_{\text{death}} \underbrace{-\, k_{antiRR}\, anti_R\, R_2}_{\text{anti-Treg drug}}. \tag{2.8}$$

The Eq. (2.8) represents the Treg cells. Dendritic cell-mediated Treg production and IL-2 stimulation[61] contribute to the amount of Treg in the prostate gland. The migration term instead accounts for the Treg cells migrating from the lymphoid tissue compartment. Following the same modeling approach used for CTL, these cells reach the prostate gland with a fixed probability of $p_R = 0.5$[23]. "Activation by tumor" term describes the tumor ability to activate Treg cells as one of the tumor survival mechanisms [98]. Treg cells have a turnover rate of μ_R, as shown in the death term of the equation. Treg cells are inactivated by the anti-Treg drug ($anti_R$), which is set to 1 when administered, 0 otherwise.

$$\frac{dM}{dt} = \underbrace{\rho_M}_{\text{source}} \underbrace{-\, \mu_M\, M}_{\text{death}} \underbrace{+\, a_{XM} \frac{(X_1 + X_2)}{s_M + (X_1 + X_2)}}_{\text{activation by tumor}} \underbrace{-\, k_{antiMM}\, anti_M\, M}_{\text{anti-MDSC drug}}. \tag{2.9}$$

The Eq. (2.9) describes the MDSC dynamics in terms of MDSC source, death and tumor-dependent activation. The form of this equation is taken from Shariatpanahi *et al.* [106]. We adapted their parameter estimates to our non-dimensionalized model (Table 2.3). The source of MDSCs is constant, while their turn-over is MDSC amount-dependent. Prostate cancer preserves its growth by recruiting and activating MDSC within the prostate microenvironment as described by the "activation by tumor" term. MDSC are inactivated by the anti-MDSC drug ($anti_M$), which is set to 1 when administered, 0 otherwise.

$$\frac{dI_2}{dt} = \underbrace{a_{CI}\, C_2}_{\substack{\text{production}\\ \text{by CTL}}} \underbrace{-\, \mu_I\, I_2}_{\text{death}} \underbrace{-\, k_{antiIl}\, anti_I\, I_2}_{\text{anti-IL-2 drug}}. \tag{2.10}$$

The equation (2.10) describes the IL-2 dynamics. IL-2 is produced by several immune cells, mainly T cells [107]. As already modeled in other studies [21; 23; 26; 108; 109], our model considers CTLs

(C_2) as the main responsible for IL-2 production, described by the "production by CTL" term.

In the death and anti-IL-2 drug terms, IL-2 physiological degradation rate μ_I is enhanced by the anti-IL-2 drug variable ($anti_I$), which is $anti_I(0) = 1$ in case of anti-IL-2 treatment.

$$\frac{dA}{dt} = \underbrace{\lambda_A\ (1 - A)}_{\substack{\text{proliferation} \\ \text{and death}}} \underbrace{-\ \lambda_A\ 1_{CX}}_{\substack{\text{androgen} \\ \text{deprivation effect}}} . \tag{2.11}$$

The Eq. (2.11) describes two possible androgen (A) dynamics, depending on the value of the Boolean function 1_{CX}, which is set to 1 in case of androgen deprivation therapy, 0 otherwise. When $1_{CX} = 0$, the equation becomes:

$$\frac{dA}{dt} = \lambda_A(1 - A),$$

which is equal to zero by imposing the initial condition $A(0) = 1$, *i.e.* constant androgen level over time.

Conversely, when $1_{CX} = 1$, the androgen level exhibits an exponential decay with rate λ_A, calculated following the standard approach as:

$$\lambda_A = \frac{ln(2)}{t_{1/2}},$$

where $t_{1/2} = 7$ days is the androgen half-life[23].

Lymphoid tissue compartment

The lymphoid tissue compartment contains the immune system cells (D_f, D_r, CTLs and Tregs) and the IL-2.

$$\frac{dD_f}{dt} = \underbrace{p_D\ m_D\ D_m}_{\text{migration}} \underbrace{-\ a_{DfDr}\ D_f}_{\text{transformation}}, \tag{2.12}$$

$$\frac{dD_r}{dt} = \underbrace{a_{DfDr}\ D_f}_{\text{transformation}} \underbrace{-\ \mu_D\ D_r}_{\text{death}} \tag{2.13}$$

Eq.s (2.12) and (2.13) represent the dynamics of the functional (D_f) and regulatory (D_r) dendritic cells, respectively. A fraction of D_m cells migrates from the prostate gland to the lymphoid tissue, differentiating into functional dendritic cells with a probability p_D here set to 0.5[23] ("migration" term). A fraction of D_f differentiates into D_r within the lymphoid tissue compartment, as described by the "transformation" term, which reduces D_f in Eq. (2.12) and increases D_r in Eq. (2.13). D_r cells are ultimately reduced by the death term in Eq. (2.13).

$$\frac{dC_1}{dt} = \underbrace{a_{Df}\, D_f}_{\substack{\text{activation}\\ \text{by } D_f}} \underbrace{+ a_{IC}\frac{C_1\, I_1}{s_I + I_1}}_{\substack{\text{stimulation}\\ \text{by IL-2}}} \underbrace{- m_C\, C_1}_{\text{migration}} \underbrace{- k_{RC}\, R_1\, C_1}_{\text{inhibition by Treg}} \underbrace{- \mu_C\, C_1}_{\text{death}}. \tag{2.14}$$

CTLs are described by the Eq. (2.14). The action of D_f cells activates CTLs, as defined by the "activaton by D_f" term, and IL-2 promotes their proliferation, as described in the "stimulation by IL-2" term. CTLs have two possible fates, either reduced by the "inhibition by Treg" and "death" terms, or released from the lymphoid tissue compartment, as described by the "migration" term.

$$\frac{dR_1}{dt} = \underbrace{a_{DrR}\, D_r}_{\substack{\text{production}\\ \text{by } D_r}} \underbrace{+ a_{IR}\, I_1}_{\substack{\text{stimulation}\\ \text{by IL-2}}} \underbrace{- m_R\, R_1}_{\text{migration}} \underbrace{- \mu_R\, R_1}_{\text{death}} - \underbrace{k_{antiRR}\, anti_R\, R_1}_{\text{anti-Treg drug}}. \tag{2.15}$$

The Eq. (2.15) represents the Treg dynamics. D_r induces Treg differentiation, as defined by the "production by D_r" term, and IL-2 promotes their proliferation, as described in the "stimulation by IL-2" term. Tregs are either released from the lymphoid tissue, or induced to apoptosis by the "death" term and by the "anti-Treg drug" term, if administered ($anti_R = 1$).

$$\frac{dI_1}{dt} = \underbrace{a_{CI}\, C_1}_{\substack{\text{production}\\ \text{by CTL}}} \underbrace{- \mu_I\, I_1}_{\text{death}} \underbrace{- k_{antiI}\, anti_I\, I_1}_{\text{anti-IL-2 drug}}. \tag{2.16}$$

Eq. (2.16) defines IL-2 dynamics within the lymphoid tissue, similarly to Eq. (2.10) in the prostate gland compartment. Taking into account that CTLs and IL-2 are tissue-associated, all terms have been previously described.

Treatments

The model provides a description of seven treatments (Table 3.1), two of which are not described by a dedicated equation. In detail, the administration of androgen deprivation therapy is implemented by the term $-\lambda_A 1_{CX}$ in Eq. (2.11), while the injection of NK cells is simulated by changing the initial value of NK variable (see Section 2.5).

The other five treatments have been modeled using the following ODEs to represent the treatment decays:

$$\frac{dV}{dt} = -\lambda_V \, V; \tag{2.17}$$

$$\frac{danti_I}{dt} = -\lambda_{AI} \, anti_I; \tag{2.18}$$

$$\frac{danti_R}{dt} = -\lambda_{AR} \, anti_R; \tag{2.19}$$

$$\frac{danti_M}{dt} = -\lambda_{AM} \, anti_M; \tag{2.20}$$

$$\frac{dI_{CB}}{dt} = -\lambda_{ICB} \, I_{CB}. \tag{2.21}$$

The Eq.s (2.17), (2.18) and (2.19) have been presented in Peng *et al.*[23] and describe the dynamics of vaccine, anti-IL-2 and anti-Treg drugs, respectively. In our model, we introduce the decay of the anti-MDSC drug, described by Eq. (2.20), and the degradation of the ICB drugs as defined by Eq. (2.21). Each degradation rate has been calculated as explained in Eq. (2.11) description, considering the following half-lives:

- $t_{1/2}^{V} = 7$ days (as in [23]);
- $t_{1/2}^{AI} = 7$ days (as in [23]);
- $t_{1/2}^{AR} = 7$ days (as in [23]);
- $t_{1/2}^{AM} = 3.5$ hours [110];
- $t_{1/2}^{ICB} = 5$ days [111; 112].

2.2 Model calibration

The model comprehends 51 parameters, but 23 of these are directly taken from the literature or computed as specified in the equation description (e.g. Eq. (2.7)) without relying on numerical optimization methods. The remaining 28 parameters have been numerically estimated. Among these, 18 have been only refined by the optimization function in an interval close to their literature values, while the other 10 parameters have been entirely estimated in this work. For a detailed description of the estimation procedure, we refer to Table 2.3. Before calibrating the model, we also evaluated its structural identifiability by means of the Matlab toolbox GenSSI [84]. Despite some limitations of the employed algorithm, which imposed some restrictions on the inclusion of all the experimental data considered for model calibration, the analysis guarantees a local identifiability. We refer to Section 2.5 for further details.

2.2.1 Experimental data

Model calibration has been performed taking into account a wide range of published data [23; 91–93]. The authors from [23; 64; 92; 93] collected *in vivo* data measuring the amount of some variables included in our model, while from [91; 92] we extrapolated *in vitro* data. In the following we explain in detail the data becoming from each citied work.

For consistency purposes, our model includes data presented by Peng *et al.* [23], the starting model that we extended. The authors considered prostate-specific Pten -/- mice, which has been specifically selected to mimic the natural tumorigenesis of human prostate cancer development as well as the effects of treatment [113]. Starting at 14 weeks of mouse-life, when the developed prostate cancer reaches a volume large enough to be treated, tumor size, CTLs and Tregs populations were measured every 2.5 weeks for 5 weeks in both prostate gland and lymphoid tissues.

Wang *et al.* paper [64] collects *in vivo* data of prostate-specific Pten-/-Smd4-/- mice. They measured the percentage of several immune cells in prostate gland at 5, 8 and 14 weeks of age.

The paper from Garcia *et al.* [92] includes data of untreated prostate-specific Pten -/- mice. The authors collected time series of CTLs and MDSCs infiltrating prostate cancer at week 6, 9 and 16 of mouse-life. Moreover, they showed that the presence of MDSCs in the tumor microenvironment is able to reduce CTL's concentration of 42% *in vitro*.

To introduce the NK cells, we needed to estimate the NK-dependent tumor regression. Therefore, we considered data from Lin *et al.* [91] regarding two *in vitro* human prostate cancer cell lines. The experiments highlighted that the prostate cancer co-cultured with NK cells halved its growth after 48 hours.

The optimal NK injection dose has been calculated following Domogala *et al.*[95] indications. This paper reported that doses nine-times greater than the usual amount of circulating NK cells are well-tolerated in men.

The effects of androgen deprivation combined to either ICB or anti-MDSC alone or the two treatments together have been measured by Lu *et al.* [93]. They delivered the androgen deprivation to 14 weeks-old severely-mutated Pten mice and, 3 weeks later, the immunotherapy. The anti-MDSC and ICB were administered 3 times per week and everyday, respectively, for 4 weeks before endpoint analysis. Specifically, the ICB treatment was defined by a cocktail of anti-CTLA4 and anti-PD1 antibodies, while the anti-MDSC treatment has been performed by Cabozatinib alone.

2.2.2 Optimization objective function

The optimization function that we created to estimate the parameters is composed of the sum of three main parts that correspond to the experimental scenarios described in the previous subsection:

$$Opt = Opt_1 \ + \ Opt_2 \ + \ Opt_3.$$

The function Opt_1 has been defined integrating the Peng's experimental data to the other time series taken from Garcia *et al.* [92]. To properly adapt Garcia's quantitative data to Peng's

relative data, we needed to calculate the ratio between cell counts at 16 and 14 weeks, which is the simulation starting point. Since the Garcia's experimental data missed the cell count of 14 weeks-old mice, we extrapolated the corresponding amount of CTLs and MDSCs by the linear regression of the available data.

We fitted the model by minimizing the absolute difference between model-predicted variable dynamics and experimental data :

$$Opt_1 \;=\; \frac{1}{7}\sum_{i=1}^{7}\left[\frac{1}{M_i}\sum_{j=1}^{M_i}\left(\frac{1}{N_j}\sum_{k=1}^{N_j}|X_k-\overline{X}_k|\right)\right],$$

where 7 is the number of combination therapies considered in Peng *et al.*[23]. For each combination therapy, M_i is the number of variables requiring data extrapolation, while, for each variable, N_j is the number of time-point dependent data. X_k is the estimated variable value computed by simulating the model, and $\overline{X}_k$ is the corresponding experimental data.

The second term Opt_2 takes into account the *in vitro* human prostate cancer cell lines from Lin *et al.* [91] and the *in vitro* Pten null prostate cancer cell lines from Garcia *et al.* [92]. The initial values of all model variables not present in the experiments of interest have been set to zero. The initial values of NK and PCa have been reported in Wang *et al.*[64], while CTL and MDSC have been extrapolated from Garcia's experimental data [92] as previously described. We used a weighted least squares method to fit the experimental data:

$$Opt_2 \;=\; w_1\left(\frac{T_{NK}}{T}-0.5\right)^2 \;+\; w_2\left(\frac{C_M}{C}-0.42\right)^2.$$

w_1 and w_2 are the empirically estimated weights required to consistently scale the value of Op_2 with respect to the other two components Opt_1 and Opt_3. T_{NK} is the model-predicted tumor amount co-cultured with NK cells for 2 days, while T is the model-predicted tumor amount cultured without NK cells. C_M is the model-predicted number of CTLs co-cultured with MDSCs for 5 days, while C is the model-predicted count of CTLs cultured without MDSCs. The percentages

0.5 and 0.42 derive from experimental data.

Following a similar strategy, we used data of ICB and anti-MDSC drugs to define the last part of the optimization function Opt_3. In our model, immunotherapies have been administered reproducing the protocol of Lu *et al.* work [93]. We compared the castration-resistant tumor size after 7 weeks of either ICB or anti-MDSC drugs alone or their combination versus the immunotherapy-free control. The same procedure has been repeated for MDSCs. The two ratios have been optimized through weighted least squares method:

$$Opt_3 \;=\; \sum_{k=1}^{3} \hat{w}_k \cdot \left(\frac{T_k}{T_{cx}} - \overline{Rt}_k \right)^2 \;+\; \sum_{k=1}^{3} \tilde{w}_k \cdot \left(\frac{M_k}{M_{cx}} - \overline{Rm}_k \right)^2,$$

where the summations from 1 to 3 fit the three treatment conditions. $\hat{w}_k$ and $\tilde{w}_k$ are the empirically estimated weights required to consistently scale the value of Op_3 with respect to the other two components Opt_1 and Opt_2. T_k and M_k represent the model-predicted amount of tumor and MDSCs, respectively, when the therapy k is administered. These values are compared with T_{cx} and M_{cx} providing the model-predicted size of tumor and MDSC population under androgen deprivation alone. $\overline{Rt}_k$ and $\overline{Rm}_k$ represent the two ratios derived from the experimental data [93].

2.3 Model simulations and sensitivity analyses

In this section, we verify if the model herein developed could capture the effect of a variety of experimentally tested treatments. To keep the simulation consistent with the experimental data, the system was simulated for 7 weeks (49 days), starting from an already developed cancer (14 weeks of age of mice). In fact, 7 weeks is the longest period considered in the *in vivo* experiments carried out to generate the data included in our model (see section 2.2). The dynamics of the main system variables are described for all the experimental therapies considered for the model calibration [23; 92; 95]. The variable dynamics are expressed in terms of fold-change with

respect to their initial values. The experimental data (red dots) are compared to the simulated behaviors (solid lines). Within the tumor chart, the dark blue line represents the total tumor volume while green and the light blue lines represent the predicted ADPC and AIPC dynamics, respectively. The first scenario discussed is represented by the untreated case (Fig. 3.3), which

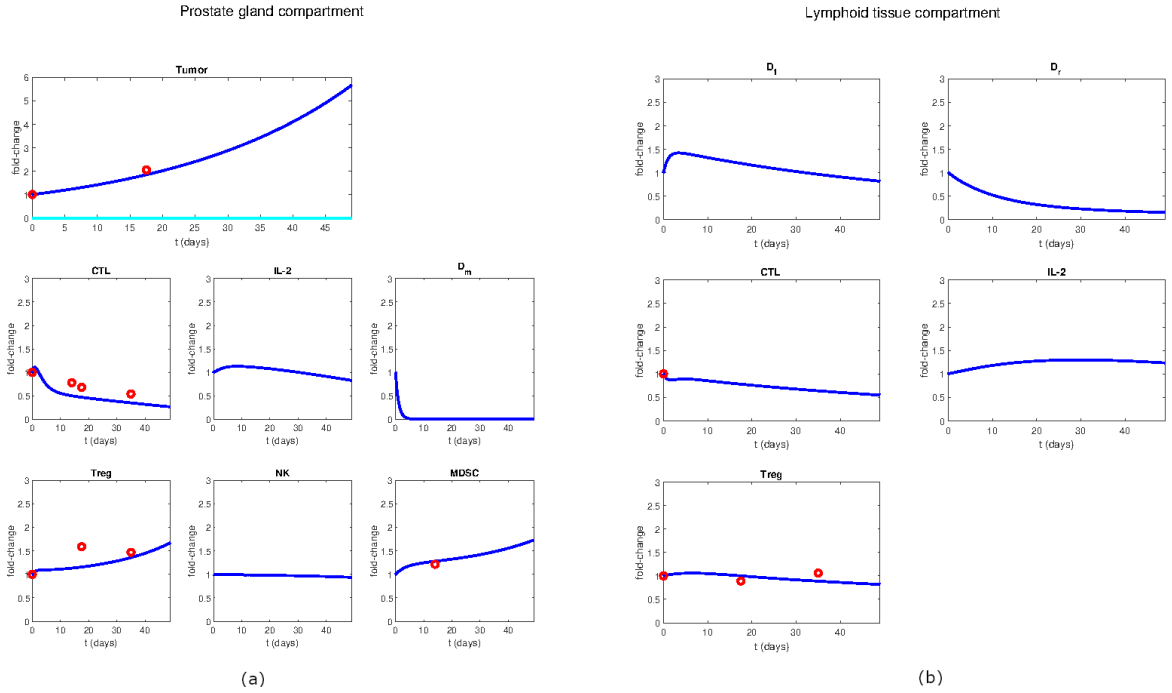

Figure 2.2: Mouse PCa model dynamics in untreated case. (a) Variables of the prostate gland compartment. (b) Variables of the lymphoid tissue compartment. The simulation time is 7 weeks (49 days). The variable dynamics are expressed in terms of fold-change with respect to their initial values. The experimental data (red dots) are compared to the simulated behaviors (solid lines). Within the tumor chart, the dark blue line represents the total tumor volume while the light blue line represents the predicted AIPC dynamics.

is the reference for evaluating the treatment effectiveness. In the absence of any treatments, the model simulation (Fig. 3.3) shows that the tumor expands up to six times its initial volume before reaching the endpoint (dark blue line in the tumor chart). In parallel, both Tregs and MDSCs increase almost twice within the 7 weeks. Conversely, the number of CTLs and mature dendritic cells decreases over time, showing a progressive establishment of an immunosuppressive tumor microenvironment. It is noteworthy that, in the absence of androgen deprivation therapy,

the entire tumor (dark blue line) is predicted to be androgen dependent. When the model is

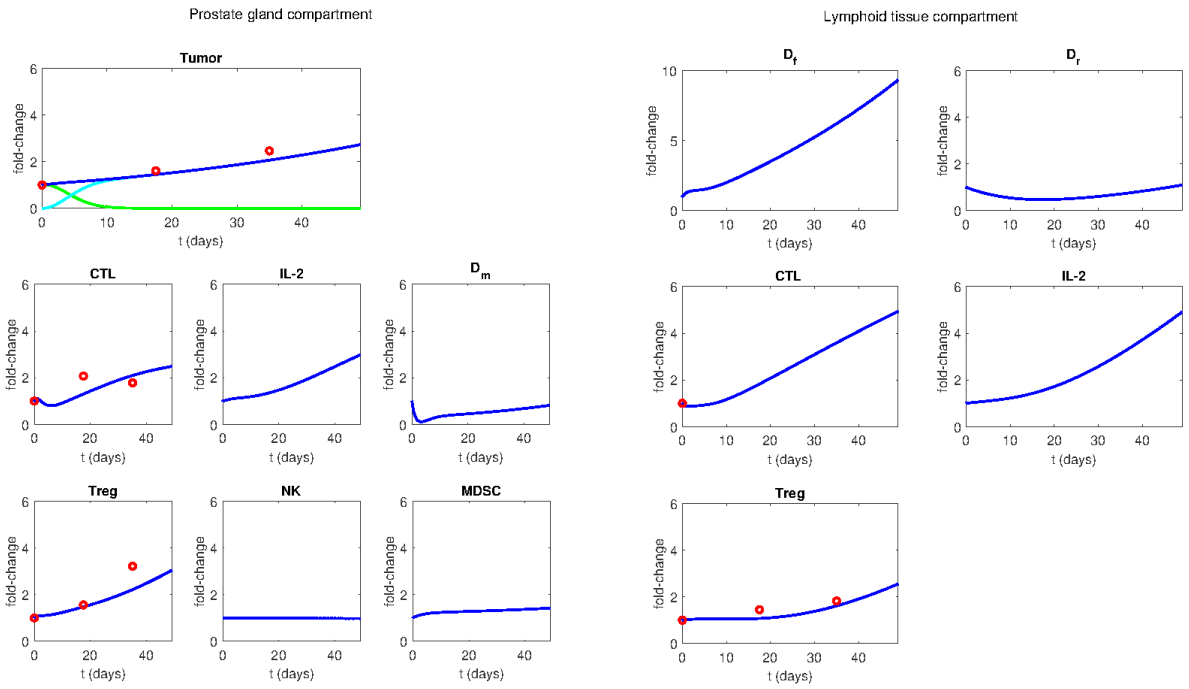

Figure 2.3: Mouse PCa model dynamics under androgen deprivation treatment. (a) Variables of the prostate gland compartment. (b) Variables of the lymphoid tissue compartment. The simulation time is 7 weeks (49 days). The variable dynamics are expressed in terms of fold-change with respect to their initial values. The experimental data (red dots) are compared to the simulated behaviors (solid lines). Within the tumor chart, the dark blue line represents the total tumor volume while green and the light blue lines represent the predicted ADPC and AIPC dynamics, respectively.

simulated with the androgen deprivation therapy, the tumor evolves to its AIPC form, as shown in Figure 3.4. In this scenario, the total tumor (dark blue line in the tumor chart) is growing at a slower pace than in the untreated simulation and, by the end of the simulation (7-week time point), it reaches a three-times smaller volume than in the untreated case. In the prostate gland compartment, we observed a marked increase in CTLs and Tregs, while mature dendritic cells showed a less pronounced growth. Unlike the untreated case, the androgen deprivation therapy induces an increase in the amount of dendritic cells as well as cytotoxic and regulatory T cells in the lymphoid tissue compartment.

We also considered data derived from experiments including the following immunotherapies:

anti IL-2, anti-Treg, vaccine, NK administration, ICB and anti-MDSC (2.9-2.16 in Section 2.6). The simulations of these scenarios show that androgen deprivation therapy is highly potentiated by ICB and anti-MDSC, in agreement with the experimental data [93]. In particular, our model predicts that the therapeutic scheme in which androgen deprivation is followed by a combination of ICB and anti-MDSC diminishes the tumor size by 30% at 7-week time point, a reduction greater than 70% compared to the untreated case (Fig. 2.16).

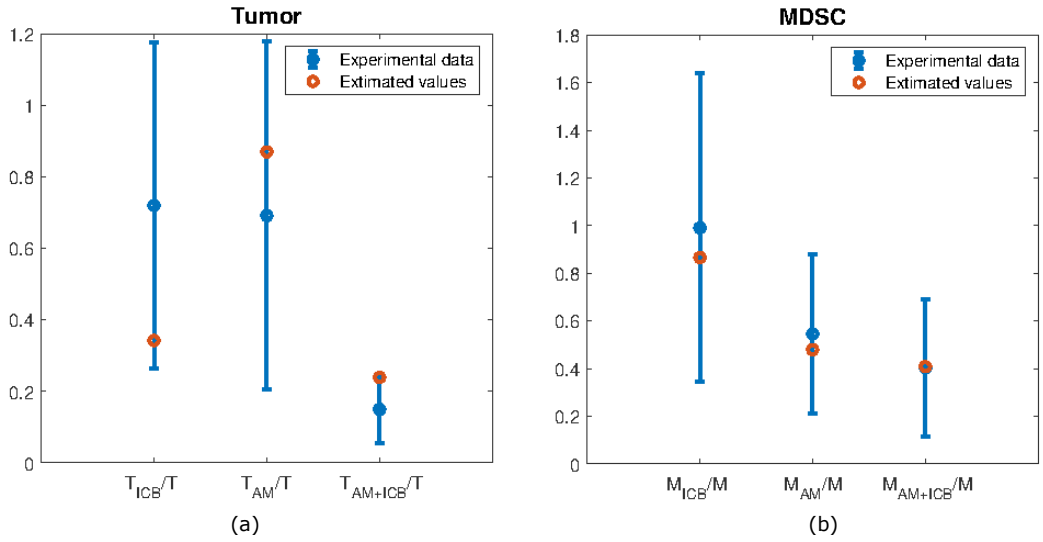

Figure 2.4: Mouse PCa model fitting experimental data of immune checkpoint blockade and anti-MDSC therapies. (a) Ratios of castration-resistant tumor (T) in immuno-treated prostate cancer to untreated. (b) Ratios of MDSCs population (M) in immuno-treated prostate cancer to untreated. Described immunotherapy scenarios: ICB treatment (ICB), anti-MDSC treatment (AM) and ICB combined to anti-MDSC therapies (AM+ICB). Experimental data[93] are representted as blue points with the corresponding standard deviations (blue bar). Model simulation results are shown as red points.

The experimental data related to the NK infusion, ICB and anti-MDSC treatments are not expressed as fold-changes between the baseline and the time-point of interest and, thus, these data are not shown in Figures 2.14-2.17. As explained in 2.2 section, the data used for estimating the ICB and anti-MDSC efficacy, are expressed as ratios. The Figure 2.4 shows the changing in castration-resistant tumor size (a) and in MDSC population (b) after either ICB or anti-MDSC single-therapies and after ICB and anti-MDSC dual-drug immunotherapy. The estimated values are compared with the experimental data derived by [93].

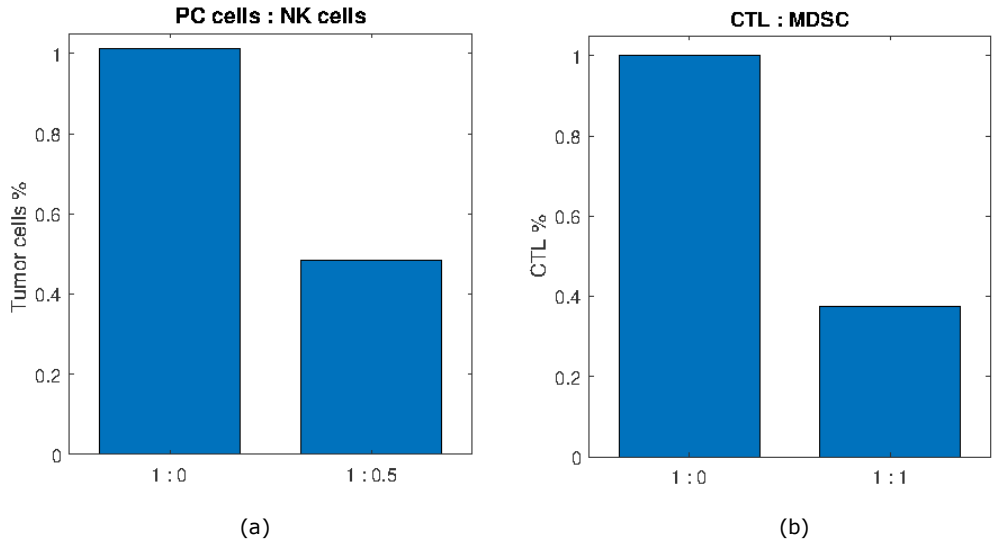

Figure 2.5: Mouse PCa model fitting experimental data of *in vitro* experiments. Cell proportions reported on the x axis are specified at each graph top side. (a) 100% tumor cells is the control sample, reduced by 50% after NK cell co-culture [91]. (b) 100% CTLs is the control sample, reduced by 42% after MDSCs co-culture [92].

The dosage of NK cells for the corresponding treatment has been chosen according to the literature [95], as described in the previous section. To estimate the NK efficacy we considered the *in vitro* data provided in [91], which highlight a 50% tumor size reduction after NK cell injection. Figure 2.5(a) shows the model validation of the described *in vitro* scenario. The 2.5(b), instead, refers to the model validation of the other *in vitro* data taken from [92], which shows the CTL population reduced by 42% after anti-MDSC treatment.

Overall, the model is in agreement with the considered data. It captures the temporal growth of the tumor volume and the modulation of immune cell levels, as well as the other described experimental data used for model calibration.

To evaluate the reliability of model predictions with respect to the uncertainty of parameter estimates, we performed a local and a global sensitivity analysis of the tumor variable defined as the sum of the ADPC and AIPC. The results of such analysis are reported in the Appendix A. The Local Sensitivity Analysis (LSA) highlights the obvious high dependence of tumor on its death and proliferation rates in all the reproduced experimental scenarios. Moreover, when

the ICB treatment is administered, also the CTL activity influences the tumor growth as well as the maximal effect of ICB drug δ_{ICB}, as expected. These results have been also confirmed by the Global Sensitivity Analysis (GSA), which predicts a hight dependence of tumor on its proliferation and death rates, as well as on those parameters which regulates the killing abilities of the immune system, such as the maximal killing rate of tumor by CTLs and NK cells (k_{CX} and k_{NT}, respectively). Moreover, also the parameters describing the action of Treg, MDSC and ICB are predicted to influence the tumor growth, especially when the corresponding therapies are administered. For example, in case of ICB therapy, the perturbation of the parameter δ_{ICB}, describing the effect of ICB drug on the CTL tumor killing rate, induces a strong variation in tumor size (Fig. A.8). The results of the LSA and the GSA suggest that the tumor dynamics is not significantly affected by parameter uncertainty, except for the few parameters that we expect playing a crucial role. For technical details see Section 2.5.

2.4 Identification of effective drug combinations for prostate cancer treatment

After having verified the capability of our model to reproduce the experimental data, we explored the possibility of using the model to predict the efficacy of the combination therapies. To compare all the treatment combinations, we defined a standard in silico protocol of drug administration. In these simulations, all treatments started simultaneously at week 0 and ended at week 4. The efficacy of the therapy was evaluated comparing the predicted tumor size at week 4 of therapy simulation with the tumor size in the untreated scenario at the same time point. A summary of the most and least successful therapies, divided by the number of included treatments, is reported in Table 2.2 and a graphical representation of the results for single-, dual- and triple-drug therapies is visualized in Fig. 2.6.

Number of combined treatments	**Best combination**	**Worst combination**
2	CX+ICB	V+AI
3	CX+V+ICB	V+AI+NK
4	V+AR+ICB+AM	V+AI+AR+AM
5	V+AR+NK+ICB+AM	CX+V+AI+AR+AM
6	CX+V+AR+NK+ICB+AM	CX+V+AI+AR+NK+AM

Table 2.2: Table of the model predicted best and worst treatment protocols for mouse PCa model. The most and the least efficacious combination therapies sorted by the total number of treatments included in each therapy. Therapies are indicated by the following abbreviations: Androgen Deprivation (CX), Anti-IL-2 (AI), Anti-Treg (AR), Anti-MDSC (AM), Vaccine (V), infusion of NK cells (NK) and Immune-Checkpoint Blockade (ICB).

When monotherapy is considered, our simulations indicate that castration is the the most effective treatment, with a 33% smaller tumor size at week 4 compared to the untreated. On the other hand, cancer vaccination is predicted to be the least beneficial one, with almost no effect on the tumor (Fig. 2.6(a)). In the case of dual-drug therapies, androgen deprivation combined with one immunotherapy is shown to increase the percentage of tumor reduction in all cases (Fig. 2.6(b)). In particular, androgen deprivation coupled with ICB is predicted to be the most effective therapy, with 64% tumor reduction compared with the untreated. Conversely, the addition of vaccination to androgen deprivation induces a less than one percent decrease, suggesting a minimal contribution of this immunotherapy to contain the tumor burden. However, vaccination is showing a complex behaviour and its contribution to the tumor-size reduction is highly dependent on the other drugs included in the combination therapy. For example, it shows an antagonistic behaviour with anti-IL2, anti-Treg and NK infusion, because the predicted tumor inhibition of these treatments, tested as single drugs, is higher than the one obtained by combining them with the vaccine. Conversely, vaccine exhibits an additive effect when combined with

(a)

Single-drug therapies	Tumor inhibition %
'V'	-0.51%
'AI'	-2.18%
'NK'	-7.04%
'AR'	-10.45%
'AM'	-12.61%
'ICB'	-26.06%
'CX'	-33.11%

(b)

Dual-drug therapies	Tumor inhibition %
'V+AI'	-1.79%
'V+NK'	-4.97%
'V+AR'	-10.13%
'AI+NK'	-13.16%
'AI+AR'	-13.17%
'V+AM'	-13.47%
'AI+AM'	-14.56%
'AR+AM'	-21.77%
'AI+ICB'	-30.26%
'NK+ICB'	-31.98%
'CX+V'	-33.60%
'CX+AI'	-34.06%
'CX+NK'	-37.12%
'CX+AR'	-39.58%
'CX+AM'	-41.77%
'AR+NK'	-43.43%
'ICB+AM'	-44.42%
'AR+ICB'	-44.93%
'NK+AM'	-49.04%
'V+ICB'	-54.27%
'CX+ICB'	-63.78%

(c)

Triple-drug therapies	Tumor inhibition %
'V+AI+NK'	-8.32%
'V+AI+AR'	-12.94%
'V+AI+AM'	-14.66%
'V+AR+AM'	-22.24%
'AI+AR+AM'	-24.35%
'CX+V+AI'	-34.24%
'CX+V+NK'	-36.31%
'V+AR+NK'	-38.98%
'AI+NK+ICB'	-39.19%
'CX+V+AR'	-39.69%
'CX+AI+NK'	-39.99%
'CX+AI+AR'	-41.19%
'CX+V+AM'	-42.40%
'CX+AI+AM'	-42.67%
'AI+AR+ICB'	-46.88%
'CX+AR+AM'	-47.58%
'V+NK+AM'	-48.20%
'AI+AR+NK'	-49.18%
'AI+ICB+AM'	-49.31%
'AI+NK+AM'	-52.56%
'V+NK+ICB'	-56.53%
'V+AI+ICB'	-59.15%
'CX+AR+NK'	-60.83%
'AR+ICB+AM'	-65.27%
'CX+NK+AM'	-65.71%
'CX+NK+ICB'	-65.76%
'CX+AI+ICB'	-66.64%
'AR+NK+ICB'	-67.48%
'AR+NK+AM'	-68.90%
'V+ICB+AM'	-69.49%
'NK+ICB+AM'	-69.60%
'CX+ICB+AM'	-73.58%
'V+AR+ICB'	-74.58%
'CX+AR+ICB'	-74.84%
'CX+V+ICB'	-75.40%

Figure 2.6: Predicted tumor inhibition percentages for different terapeutic protocols in mouse PCa model. The model-predicted effect of (a) single-, (b) dual- and (c) triple-drug therapies. Therapies have been sorted by their tumor inhibition percentage compared to the untreated case, after 4 weeks of therapy. Treatments are named by the following abbreviations: Androgen Deprivation (CX), Anti-IL-2 (AI), Anti-Treg (AR), Anti-MDSC (AM), Vaccine (V), injection of NK cells (NK) and Immune-Checkpoint Blockade (ICB).

androgen deprivation or anti-MDSC and a synergistic effect with ICB (Fig. 2.6(b)). Furthermore, when vaccine is administered in combination with androgen deprivation and ICB, we observed a 75% tumor reduction, reaching the highest percentage of tumor reduction among the triple-drug therapies (Fig. 2.6(c)). Additional simulations performed combining four, five, and six treatments are shown in Fig. 2.18.

To further explore the presence of synergistic effects among the treatments, we need of a sort of correlation measure. In the literature there are several methods to assess the synergy of combination therapies. A comprehensive review has been written by Foucquier and Guedj [114]. Among these techniques, we chose the Bliss combination index (BCI) [115], which is one of the most commonly used. The BCI is defined as a ratio between the efficacy of two therapies supposing that these do not interact and the efficacy of the same therapies administered together. To calculate this index, we need to express treatment effects as probabilities. Therefore, the first term of the ratio, describing the effect of non-interacting therapies A and B, is computed by using the law of total probability:

$$P(A \cup B) = P(A) + P(B) - P(A \cap B),$$

which, considering the independence between A and B, becomes:

$$P(A \cup B) = P(A) + P(B) - P(A)P(B).$$

If we consider the tumor inhibition percentages as probabilities, we define the BCI of two treatments A and B as:

$$BCI(A, B) = \frac{T_i(A) + T_i(B) - T_i(A)T_i(B)}{T_i(A + B)},$$

where $T_i(x)$ indicates the model-predicted percentage of tumor inhibition, compared to the untreated case, obtained by applying the therapy x. In the case of $T_i(A+B)$, this corresponds to the

model-predicted percentage of tumor inhibition given by the combination of the two treatments A and B.

When $BCI(A, B) < 1$, the model-predicted effect on tumor size of the combination therapy $A + B$ is stronger than the one of the two non-interacting therapies A and B. Therefore, the two therapies are predicted to be synergistic. Conversely, when $BCI(A, B) > 1$, the two therapies are considered antagonist.

Considering dual-drug therapies, this analysis identified anti-MDSC and NK infusion as the most synergistic treatments (BCI = 0.38), as shown in Figure 2.7(a). Despite being highly synergistic, this therapy does not reach the highest control of tumor size, that is, instead, obtained coupling CX and ICB, as described above. Indeed, the BCI of CX + ICB is 0.79, indicating a modest synergy that is nonetheless sufficient to reach a 64% tumor inhibition (Fig. 2.6(b)). In addition to the dual-drug therapies, the BCI can be computed for all treatment combinations. We observe that also the BCI of more than two treatments has been evaluated by considering couple of therapies. Indeed, for determining the BCI of three therapies A, B and C, we computed $BCI(A + B, C)$, $BCI(A, B + C)$ and $BCI(A + C, B)$, obtaining different values. The complete table is reported in the supplementary file available at `https://www.cosbi.eu/fx/0293/BCI.xlsx`. By considering all the possible combinations, the most synergistic therapy is given by the the addition of AM to a therapy that includes V and NK infusion.

We also attempted to use these results to estimate the minimal dose to maintain a satisfactory treatment efficacy. For this analysis, the minimal satisfactory tumor inhibition was fixed to the theoretical value obtained assuming that the two drugs have no interaction ($A \cup$B in Eq. (**??**)). If we consider the most promising dual-drug therapy, CX and ICB, half-dose of ICB is enough to obtain the same effect of $ICB \cup CX$ (Fig. 2.7(b)).

The results obtained from synergy analysis and tumor inhibition evaluation are complementary and their combination is essential for a more complete view of the system behavior. Hence, we built a decision tree that integrates the computed synergistic effect and the predicted percentage of tumor inhibition (Fig. 2.8). Motivated by the lack of efficacious treatments for advanced castration resistant PCa, we set out to identify an effective immunotherapy for subjects with

AIPC, which in our model develops after androgen deprivation therapy. For this reason, the androgen deprivation therapy has been set as the root of the decision tree. The immunotherapies have been included as internal nodes, connected to each other and to the root by edges, annotated with the BCI value. Only edges with a synergistic value (BCI ¡=0) are reported. The paths from the root to the terminal nodes represent the possible combined therapies and the position of the nodes along the tree reflects the efficacy of the therapies in inhibiting the tumor growth, according to the scale reported on the right (the most effective therapies are positioned lower down). This chart highlights that adding ICB to CX seems the most promising therapeutic combination to keep under control the tumor growth, notwithstanding the need to add at least one additional treatment to reduce more than 3% the tumor size compared to the baseline. If additional therapies are added, our simulations suggest vaccination as the most effective, leading to a 34% tumor reduction compared to baseline and 75% compared to the untreated.

	CX	V	AI	AR	NK	ICB	AM
CX	-						
V	1.00	-					
AI	1.01	1.50	-				
AR	1.01	1.08	0.94	-			
NK	1.02	1.51	0.69	0.39	-		
ICB	**0.79**	0.49	0.91	0.75	0.98	-	
AM	0.99	0.97	1.00	1.00	**0.38**	0.80	-

(a)

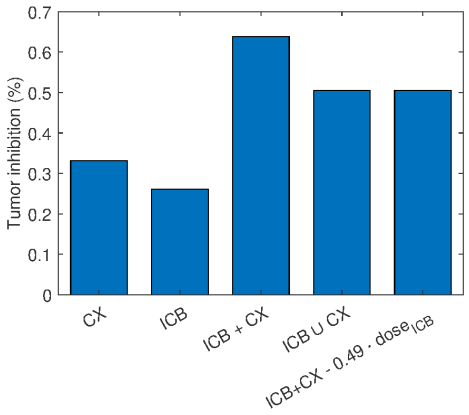

(b)

Figure 2.7: Mouse PCa model - synergistic treatments. (a) Treatment BCIs calculated between the corresponding column and row label. BCIs of the most synergistic treatments among all (NK + AM) and the most synergistic treatments relative to androgen deprivation (CX + ICB) have been highlighted in bold. (b) Tumor inhibition rates of CX and ICB as monotherapies, of ICB and CX interacting as a dual-therapy, of ICB and CX not interacting (ICB∪ CX), and of ICB half-dosage and CX interacting as a dual-therapy.

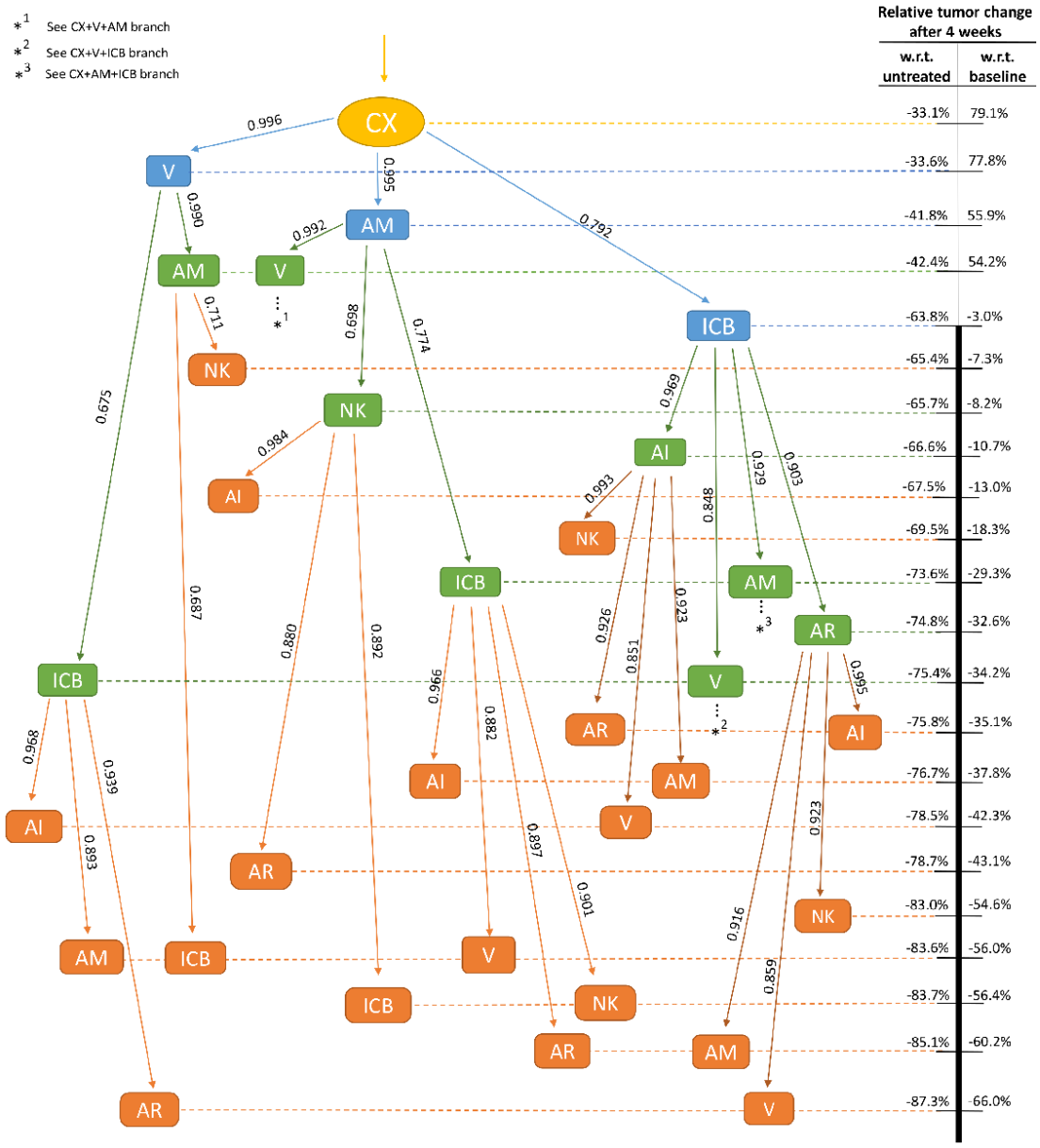

Figure 2.8: Mouse PCa model - treatment decision tree. Limiting the tree to androgen deprivation as root node, therapies have been step-wise combined to synergise (BCI reported on the corresponding edge). Each node position has been computed according to the relative tumor change after 4 weeks (scale on the right). Combined therapies at the bottom are the most effective on the tumor size. The scale thickness emphasizes the nodes able to decrease the tumor size with respect to (w.r.t.) the baseline. For simplicity, branches showing the same pattern have been replaced by stars indicating the branch of reference ($*^1$ = CX+V+AM, $*^2$ = CX+V+ICB, $*^3$ = CX+AM+ICB). Treatments are named by the following abbreviations: Androgen Deprivation (CX), Anti-IL-2 (AI), Anti-Treg (AR), Anti-MDSC (AM), Vaccine (V), injection of NK cells (NK) and Immune-Checkpoint Blockade (ICB).

2.5 Materials and methods

Computational environment

The model has been implemented as a set of Matlab functions [116], which have been simulated by the state-of-the-art *ode15s* integrator. For the model calibration, we used the evolutionary strategy provided in the optimization toolbox of Matlab: the genetic algorithm (*ga*). The optimization algorithm has been parameterized considering a population size of 200 individuals, a crossover fraction of 0.9 and a tolerance function of 10^{-2}.

Structural identifiability analysis

A structural identifiability analysis has been performed by means of the Matlab toolbox GenSSI [84]. The software requires: (i) a list of all the model variables and their relations inside the mathematical model; (ii) a list of all the model parameters, by also specifying the ones that have to be estimated; (iii) the model initial conditions for running the simulations; and (iv) a list of the experimentally observed quantities, which can be model variables or a function of these. Unfortunately, the algorithm has some limitations that prevent the complete specification of all the experimental data employed during the model calibration phase. In particular, we excluded from this analysis the *in vitro* data and the ratios of the system variables in different experimental conditions (see section 2.2 for a complete description of the experimental data). Despite these limitations, the analysis guarantees a local identifiability.

Sensitivity analyses

A local and a global sensitivity analysis have been performed on tumor size, which is the main variable discussed in this work. To conduct the Local Sensitivity Analysis (LSA), we considered the total amount of tumor as X = X1 + X2 and we evaluated the tumor LSA value of a model parameter p by using the logarithmic LSA introduced in the Chapter 1. Starting from the Eq.

(1.8), we approximated $\frac{\partial X(t,p)}{\partial p}$ by the central finite difference, obtaining:

$$LSA(p) = \frac{X(t_f, p + \Delta p) - X(t_f, p - \Delta p)}{2 \cdot \Delta \cdot X(t_f, p)},$$

where t_f is the last simulated time point (49 days).

For implementing the Global Sensitivity Analysis (GSA), we computed the median value of 1000 LSAs for each model parameter, starting from random parameter estimates inside the model parameter space. To increase the reliability of the analysis, we computed the GSA by considering the complete LSA profiles:

$$LSA(p) = \int_0^{t_f} \frac{X(t, p + \Delta p) - X(t, p - \Delta p)}{2 \cdot \Delta \cdot X(t, p)} \, dt,$$

while in the previous LSA we computed the tumor sensitivity only at the last simulated time point. This choice allowed to better capture the sensitivity of the overall tumor dynamics with respect to each parameter perturbation. The parameter space has been defined according to the following constraints. For the 28 parameters estimated by optimization methods, we used the same range of variability considered for the model calibration. For all the remaining parameters, we considered a variation of 30% their initial literature estimate. The results of both LSA and GSA obtained by fixing $\Delta = 1\%$ are shown in the Appendix A.

2.6 Additional Figures

This appendix is devoted to the inclusion of additional figures discussed in this chapter.

Figures 2.9-2.17 shows the variable dynamics expressed in terms of fold-change with respect to their initial values. The simulation time is fixed to 7 weeks. The experimental data (red dots) are compared to the simulated behaviors (solid lines). Within the tumor chart, the dark blue line represents the total tumor volume while the light blue line represents the predicted AIPC dynamics.

Figure 2.18 includes the tumor inhibition percentages corresponding to all the possible combination therapies of the seven treatments implemented.

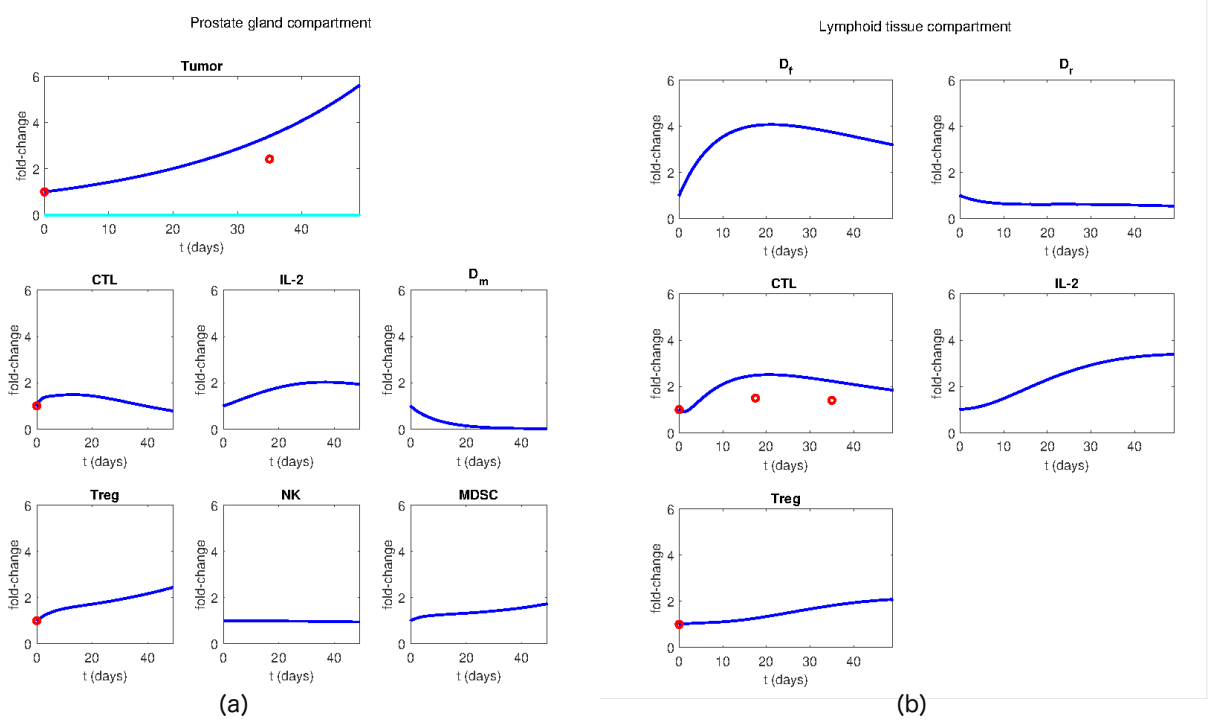

Figure 2.9: Mouse PCa model dynamics under vaccine therapy. (a) Variables of the prostate gland compartment. (b) Variables of the lymphoid tissue compartment.

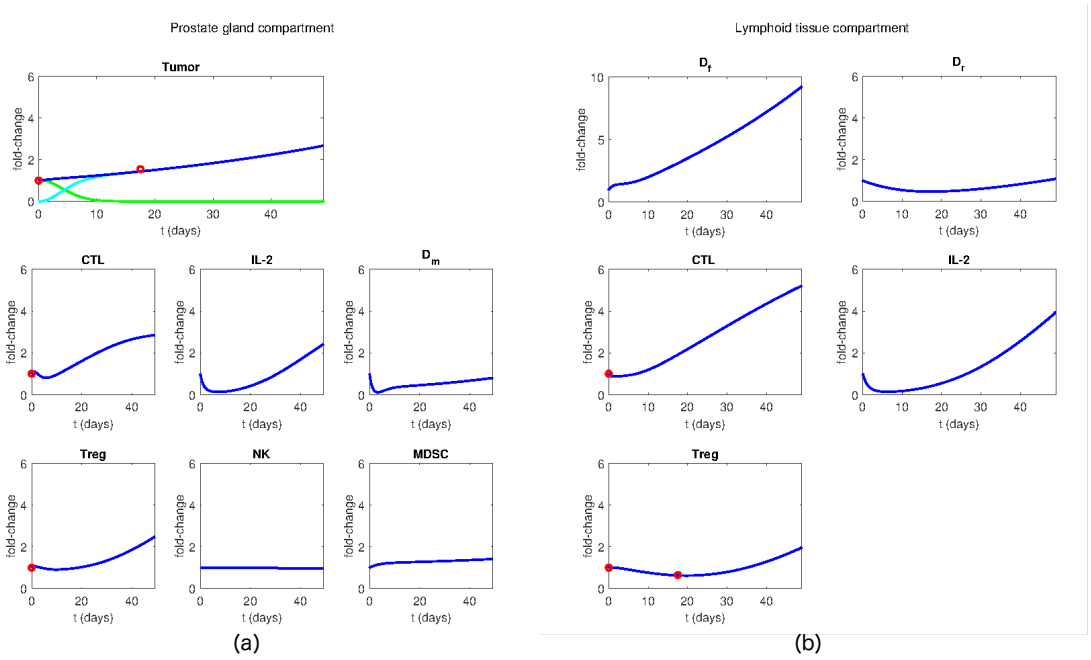

Figure 2.10: Mouse PCa model dynamics under androgen deprivation + anti-IL2 combintion therapy. (a) Variables of the prostate gland compartment. (b) Variables of the lymphoid tissue compartment.

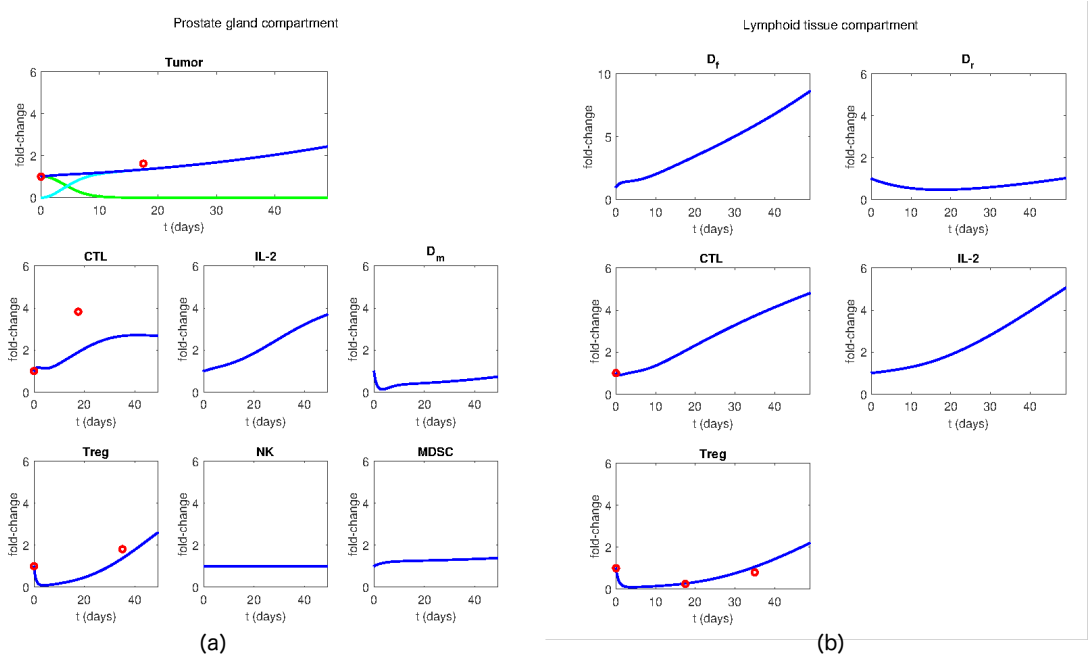

Figure 2.11: Mouse PCa model dynamics under androgen deprivation + anti-Treg combination therapy. (a) Variables of the prostate gland compartment. (b) Variables of the lymphoid tissue compartment.

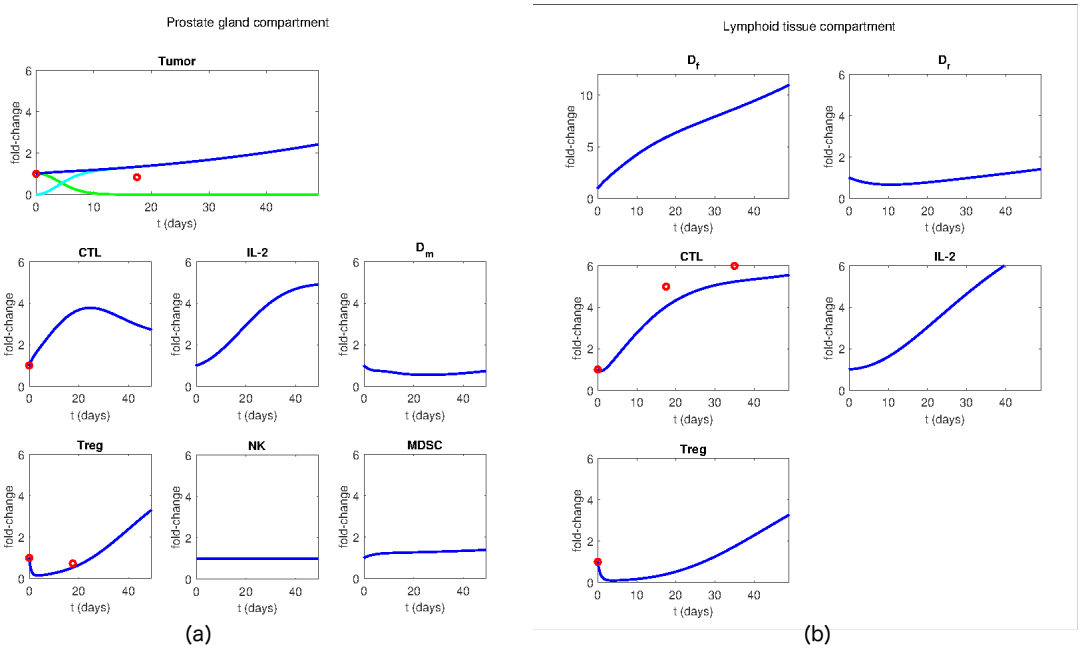

Figure 2.12: Mouse PCa model dynamics under androgen deprivation + vaccine + anti-Treg combination therapy. (a) Variables of the prostate gland compartment. (b) Variables of the lymphoid tissue compartment.

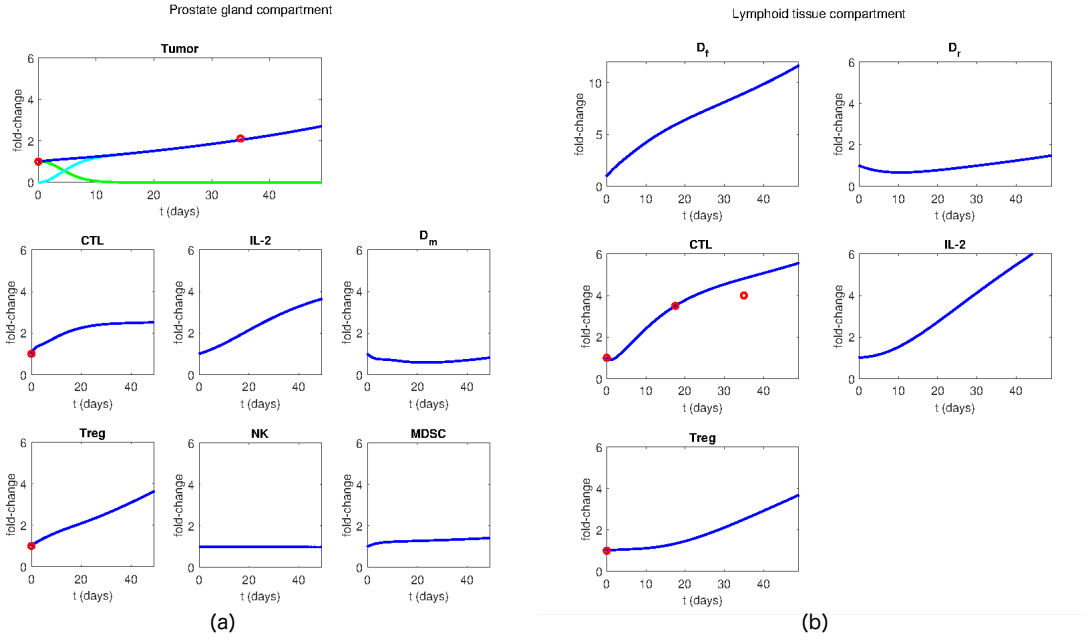

Figure 2.13: Mouse PCa model dynamics under androgen deprivation + vaccine combination therapy. (a) Variables of the prostate gland compartment. (b) Variables of the lymphoid tissue compartment.

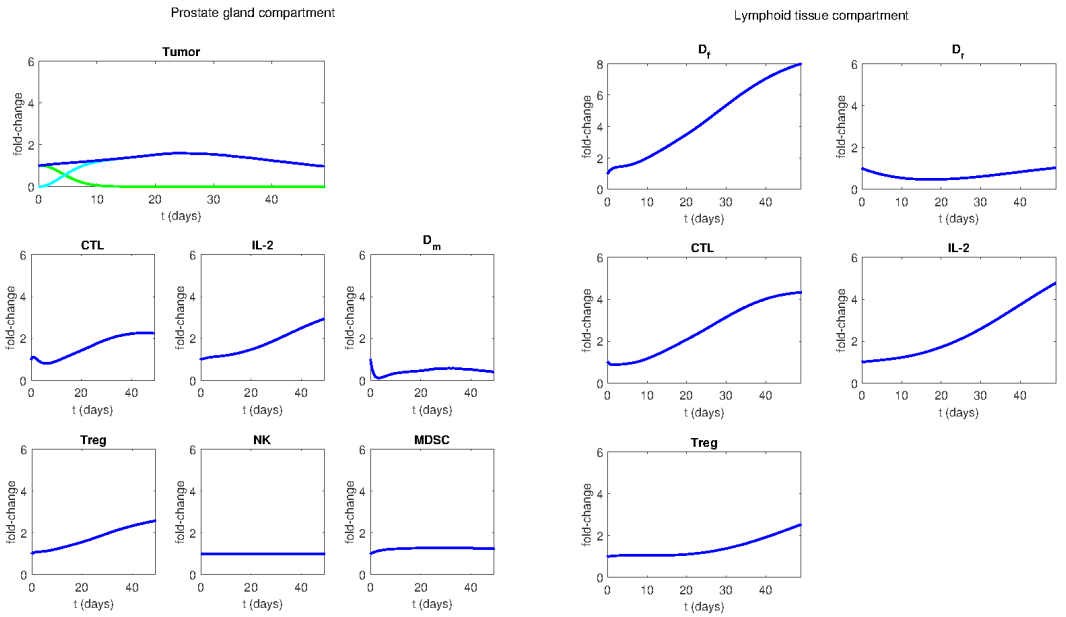

Figure 2.14: Mouse PCa model dynamics under androgen deprivation + ICB combination therapy. (a) Variables of the prostate gland compartment. (b) Variables of the lymphoid tissue compartment.

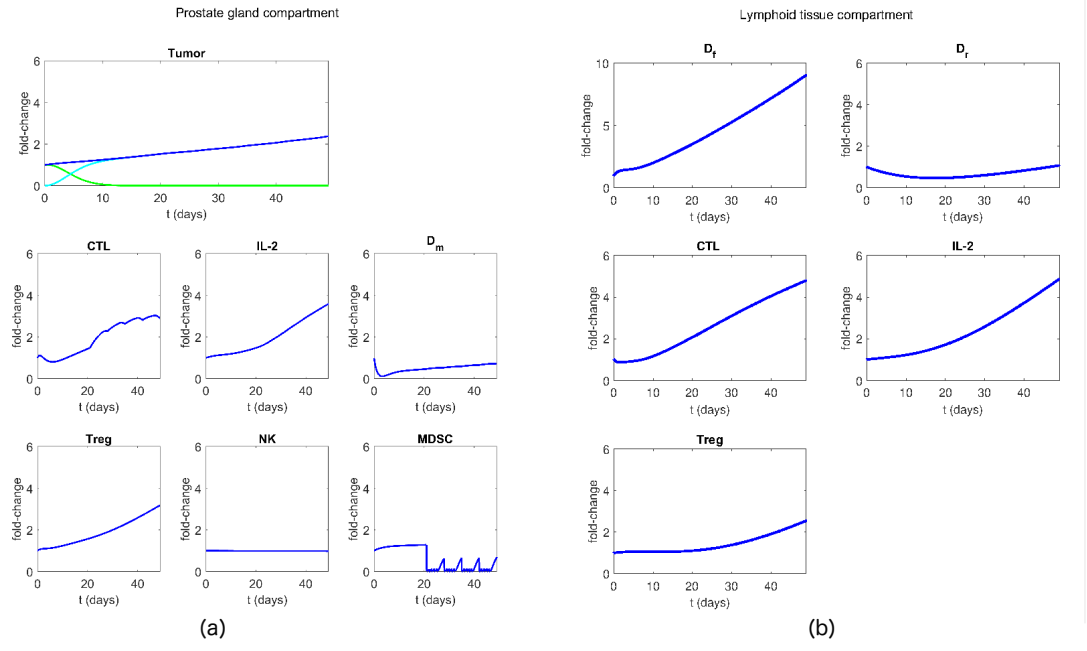

Figure 2.15: Mouse PCa model dynamics under androgen deprivation + anti-MDSC combination therapy. (a) Variables of the prostate gland compartment. (b) Variables of the lymphoid tissue compartment.

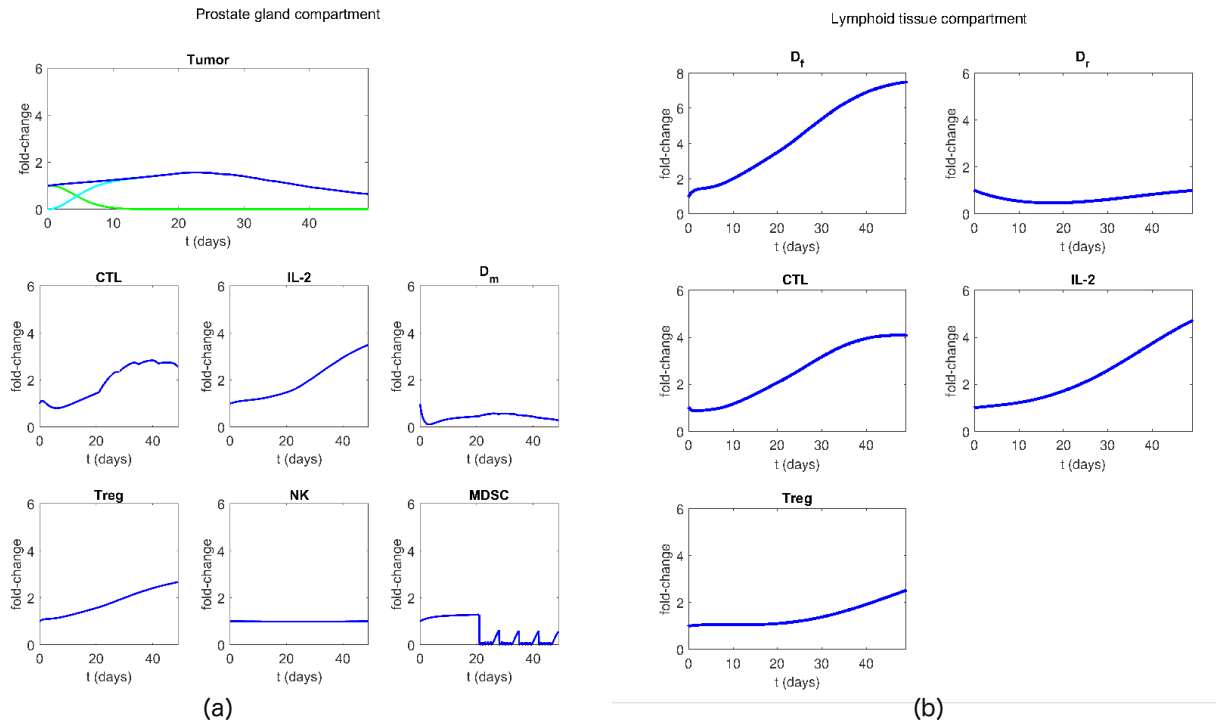

Figure 2.16: Mouse PCa model dynamics under androgen deprivation + ICB + anti-MDSC combination therapy (a) Variables of the prostate gland compartment. (b) Variables of the lymphoid tissue compartment.

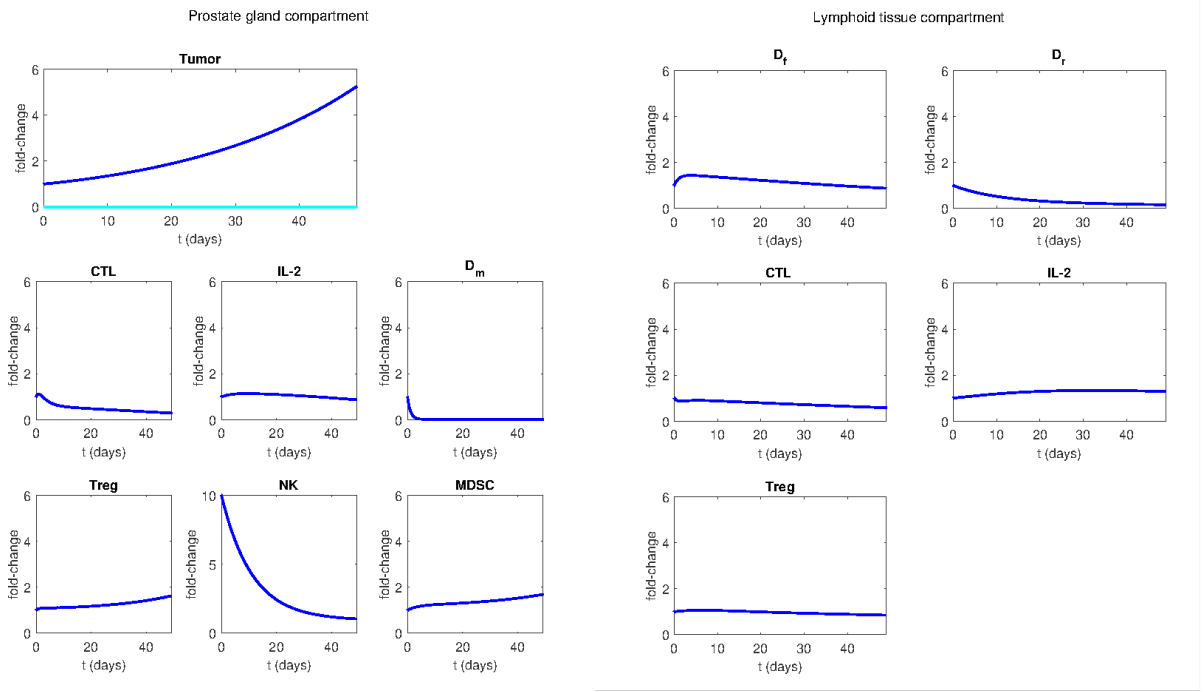

Figure 2.17: Mouse PCa model dynamics under NK infusion. (a) Variables of the prostate gland compartment. (b) Variables of the lymphoid tissue compartment. To reproduce the infusion of NK cells with a dose nine times grather than the physiological NK amount [95], we increased NK initial value assuming the same multiplicative factor.

Treatments	Tumor inhibition percentage (after 4 weeks)
'V'	-0,51%
'V+AI'	-1,79%
'AI'	-2,18%
'V+NK'	-4,97%
'NK'	-7,04%
'V+AI+NK'	-8,32%
'V+AR'	-10,13%
'AR'	-10,45%
'AM'	-12,61%
'V+AI+AR'	-12,94%
'AI+NK'	-13,16%
'AI+AR'	-13,17%
'V+AM'	-13,47%
'AI+AM'	-14,56%
'V+AI+AM'	-14,66%
'AR+AM'	-21,77%
'V+AR+AM'	-22,24%
'AI+AR+AM'	-24,35%
'V+AI+AR+AM'	-24,77%
'ICB'	-26,06%
'AI+ICB'	-30,26%
'NK+ICB'	-31,98%
'CX'	-33,11%
'CX+V'	-33,60%
'CX+AI'	-34,06%
'CX+V+AI'	-34,24%
'CX+V+NK'	-36,31%
'CX+NK'	-37,12%
'CX+V+AI+NK'	-37,94%
'V+AR+NK'	-38,98%
'AI+NK+ICB'	-39,19%
'CX+AR'	-39,58%
'CX+V+AR'	-39,69%
'CX+AI+NK'	-39,99%
'CX+AI+AR'	-41,19%
'CX+V+AI+AR'	-41,29%
'CX+AM'	-41,77%
'CX+V+AM'	-42,40%
'CX+AI+AM'	-42,67%
'CX+V+AI+AM'	-43,05%
'AR+NK'	-43,43%
'ICB+AM'	-44,42%
'AR+ICB'	-44,93%
'V+AI+AR+NK'	-45,16%
'AI+AR+ICB'	-46,88%
'CX+AR+AM'	-47,58%
'CX+V+AR+AM'	-48,15%
'V+NK+AM'	-48,20%
'NK+AM'	-49,04%
'CX+AI+AR+AM'	-49,07%
'AI+AR+NK'	-49,18%
'AI+ICB+AM'	-49,31%
'CX+V+AI+AR+AM'	-49,58%
'V+AI+NK+AM'	-50,06%
'AI+NK+AM'	-52,56%
'V+ICB'	-54,27%
'V+NK+ICB'	-56,53%
'CX+V+AR+NK'	-58,21%
'V+AI+ICB'	-59,15%
'CX+AR+NK'	-60,83%
'CX+V+AI+AR+NK'	-62,09%
'V+AI+NK+ICB'	-62,17%
'CX+ICB'	-63,78%
'CX+AI+AR+NK'	-64,57%
'AR+ICB+AM'	-65,27%
'CX+V+NK+AM'	-65,36%
'CX+NK+AM'	-65,71%
'CX+NK+ICB'	-65,76%
'CX+V+AI+NK+AM'	-66,36%
'AI+AR+ICB+AM'	-66,64%
'CX+AI+ICB'	-66,64%
'V+AR+NK+AM'	-66,69%
'AR+NK+ICB'	-67,48%
'CX+AI+NK+AM'	-67,51%
'AR+NK+AM'	-68,90%
'CX+AI+NK+ICB'	-69,47%
'V+ICB+AM'	-69,49%
'NK+ICB+AM'	-69,60%
'V+AI+AR+NK+AM'	-70,28%
'AI+AR+NK+ICB'	-71,15%
'AI+AR+NK+AM'	-72,38%
'CX+ICB+AM'	-73,58%
'AI+NK+ICB+AM'	-73,95%
'V+AR+ICB'	-74,58%
'V+AI+ICB+AM'	-74,60%
'CX+AR+ICB'	-74,84%
'CX+V+ICB'	-75,40%
'V+AI+AR+ICB'	-75,75%
'CX+AI+AR+ICB'	-75,76%
'CX+V+NK+ICB'	-76,35%
'CX+AI+ICB+AM'	-76,75%
'CX+V+AR+NK+AM'	-77,43%
'CX+V+AI+ICB'	-78,47%
'CX+AR+NK+AM'	-78,74%
'CX+V+AI+NK+ICB'	-79,65%
'CX+V+AI+AR+NK+AM'	-79,71%
'CX+AI+AR+NK+AM'	-81,01%
'V+NK+ICB+AM'	-82,42%
'CX+AR+NK+ICB'	-83,04%
'V+AR+NK+ICB'	-83,49%
'CX+V+ICB+AM'	-83,58%
'CX+NK+ICB+AM'	-83,70%
'CX+AI+AR+NK+ICB'	-84,79%
'CX+AR+ICB+AM'	-85,13%
'V+AI+AR+NK+ICB'	-85,49%
'CX+AI+AR+ICB+AM'	-85,80%
'V+AI+NK+ICB+AM'	-85,82%
'CX+AI+NK+ICB+AM'	-86,16%
'CX+V+AI+ICB+AM'	-86,65%
'CX+V+AR+ICB'	-87,31%
'AR+NK+ICB+AM'	-87,74%
'CX+V+AI+AR+ICB'	-87,94%
'V+AR+ICB+AM'	-88,59%
'AI+AR+NK+ICB+AM'	-89,23%
'V+AI+AR+ICB+AM'	-89,26%
'CX+V+NK+ICB+AM'	-89,85%
'CX+V+AR+NK+ICB'	-91,01%
'CX+V+AI+NK+ICB+AM'	-91,91%
'CX+V+AI+AR+NK+ICB'	-92,04%
'CX+AR+NK+ICB+AM'	-93,40%
'CX+AI+AR+NK+ICB+AM'	-94,17%
'CX+V+AR+ICB+AM'	-94,46%
'CX+V+AI+AR+ICB+AM'	-94,82%
'V+AR+NK+ICB+AM'	-95,46%
'V+AI+AR+NK+ICB+AM'	-96,07%
'CX+V+AR+NK+ICB+AM'	-97,44%
'CX+V+AI+AR+NK+ICB+AM'	-97,78%

Figure 2.18: Predicted tumor inhibition percentages for different terapeutic protocols in mouse PCa model - complete scheme. The model predicted effect of all the possible combination therapies. Therapies have been sorted by their tumor inhibition percentage compared to the untreated case, after 4 weeks of therapy. Treatments are named by the following abbreviations: Androgen Deprivation (CX), Anti-IL-2 (AI), Anti-Treg (AR), Anti-MDSC (AM), Vaccine (V), injection of NK cells (NK) and Immune-Checkpoint Blockade (ICB).

2.7 Table of parameters

Parameter	Description	Value	Estimation Procedure
a_{CI}	Activation rate of IL-2 by CTLs	5.84 10^{-2} day^{-1}	taken from [23]
a_{DC}	Activation rate of CTLs by Dendritic cells	4.24 10^{-1} day^{-1}	optimized around the value from [23] +/- 30%
a_{DfDr}	Transformation rate of functional Dendritic cells into regulatory Dendritic cells	1.43 10^{-2} day^{-1}	taken from [23]
a_{DR}	Activation rate of Treg by mature Dendritic cells	1.06 10^{-1} day^{-1}	taken from [23]
a_{DrR}	Activation rate of Tregs by regulatory Dendritic cells	6.75 10^{-2} day^{-1}	taken from [23]
a_{IC}	Maximal activation rate of CTLs by IL-2	7.70 10^{2} day^{-1}	unconstrained optimization
a_{IN}	Maximal activation rate of NK by IL-2	7.43 10^{-2} day^{-1}	optimized around the value from [21] after non-dimensionalization +/- 30%

a_{IR}	Activation rate of Treg by IL-2	5.06 10^{-2} day^{-1}	taken from [23]
a_{VD}	Activation rate of mature Dendritic cells by Vaccine	8.08 10^{-1} day^{-1}	optimized around the value from [23] +/- 30%
a_{XD}	Activation rate of mature Dendritic cells by Tumor	2.73 10^{-1}	optimized around the value from [23] +/- 30%
a_{XM}	Maximal activation rate of MDSC by Tumor	6.70 10^{+2} day^{-1}	optimized around the value from [106] after non-dimensionalization +/- 30%
a_{XR}	Activation rate of Treg by Tumor	2.06 10^{-2} day^{-1}	taken from [23]
k_{antiII}	Inhibition rate of IL-2 by anti-IL-2 drug	7.14 10^{-1} day^{-1}	taken from [23]
k_{antiMM}	Inhibition rate of MDSC by the drug Cabozatinib	7.57 10^{+1} day^{-1}	optimized in $[0, 100]$
k_{antiRR}	Inhibition rate of Treg by anti-Treg drug	1.43 day^{-1}	taken from [23]

k_{CX}	Killing rate of tumor by CTLs	6.55 10^{-4} day^{-1}	optimized in $[0, k_{CX}^{Peng}]$, where k_{CX}^{Peng} is the k_{CX} estimated in [23]
k_{MC}	CTL cytotoxic effect MDSC-dependent inhibition	9.62 10^{-2} day^{-1}	optimized in $[0.001, 10]$
k_{MN}	NK cytotoxic effect MDSC-dependent inhibition	3.88	optimized in $[0.001, 10]$
k_{NX}	Maximal killing rate of Tumor by NK cells	7.22 10^{-3} day^{-1}	optimized in $[0.001, 10]/7$
k_{RC}	CTL cytotoxic effect Treg-dependent inhibition	1.00 10^{-1} day^{-1}	optimized in $[0, k_{RC}^{Peng}]$, where k_{RC}^{Peng} is the k_{RC} estimated in [23]
k_{RN}	NK cytotoxic effect Treg-dependent inhibition	2.07	optimized in $[0.001, 10]$
k_{XN}	Inactivation rate of NK by Tumor	1.60 10^{-3} day^{-1}	optimized in $[0.0001, 1]$

m_C	Migration rate of CTLs out of the lymphoid tissue	4.29 10^{-1} day^{-1}	optimized around the value from [23] +/- 30%
m_D	Migration rate of mature Dendritic cells out of the prostate gland	9.36 10^{-1} day^{-1}	optimized around the value from [23] +/- 30%
m_R	Migration rate of Treg out of the lymphoid tissue	1.43 10^{-2} day^{-1}	taken from [23]
p_C	Probability of migrating CTLs to reach the prostate gland	0.5	taken from [23]
p_D	Probability of migrating mature dendritic cells to reach the lymphoid tissue	0.5	taken from [23]
p_R	Probability of migrating Treg cells to reach the prostate gland	0.5	taken from [23]
r_M	Mutation rate of ADPC into AIPC	8.11 10^{-1} day^{-1}	optimized around the value from [23] +/- 30%

r_{p1}	Proliferation rate of Androgen Dependent Prostate Cancer cells (ADPC)	3.63 10^{-2} day^{-1}	optimized around the value from [23] +/- 30%
r_{p2}	Proliferation rate of Androgen Independent Prostate Cancer cells (AIPC)	1.70 10^{-1} day^{-1}	optimized around the value from [23] +/- 30%
s_I	IL-2 saturation level for CTL clonal expansion	7.72 10^{4}	optimized around the value from [24] +/- 30%
s_M	Tumor cells saturation level for MDSC clonal expansion	1.82 10^{+4}	optimized around the value from [106] after non-dimensionalization +/- 30%
s_N	IL-2 saturation level for NK clonal expansion	1.49 10^{+2}	optimized around the value from [21] after non-dimensionalization +/- 30%
δ_{ICB}	Effect of ICB drugs on CTL killing rate	1.09 10^{+1}	optimized in $[1, 100]$

λ_A	Decay rate for Androgens under androgen deprivation therapy	9.90 10^{-2} day^{-1}	computed as explained in the description of Eq. (2.11)
λ_{AI}	Decay rate for anti-IL-2	9.90 10^{-2} day^{-1}	computed as explained in the description of Eq. (2.11) by considering the correspondent anti-IL-2 drug half-life
λ_{AM}	Decay rate for Cabozatinib	4.75 day^{-1}	computed as explained in the description of Eq. (2.11) by considering the correspondent anti-MDSC drug half-life

λ_{AR}	Decay rate for anti-Treg	9.90 10^{-2} day^{-1}	computed as explained in the description of Eq. (2.11) by considering the correspondent anti-Treg drug half-life
λ_{ICB}	Decay rate for ICB	1.39 10^{-1} day^{-1}	computed as explained in the description of Eq. (2.11) by considering the correspondent ICB drug half-life
λ_V	Decay rate for Vaccine	9.90 10^{-2} day^{-1}	computed as explained in the description of Eq. (2.11) by considering the correspondent vaccine half-life
μ_1	ADPC death rate	1.01 10^{-2} day^{-1}	optimized around the value from [23] +/- 30%

μ_2	AIPC death rate	1.48 10^{-1} day^{-1}	optimized around the value from [23] +/- 30%
μ_C	CTL death rate	1.46 10^{-1} day^{-1}	optimized around the value from [23] +/- 30%
μ_D	Dendritic cell death rate	9.29 10^{-2} day^{-1}	taken from [23]
μ_I	IL-2 death rate	3.05 10^{-2} day^{-1}	taken from [23]
μ_M	MDSC death rate	2.94 10^{-1} day^{-1}	optimized around the value from [106] after non-dimensionalization +/- 30%
μ_R	Treg death rate	8.07 10^{-2} day^{-1}	taken from [23]
μ_N	NK cell death rate	9.00 10^{-2} day^{-1}	calculated as in [21] (see NK Eq. (2.7) for details)

ρ_M	MDSC source	3.24 10^{-1}	optimized around the value from [106] after non-dimensionalization +/- 30%
ρ_N	NK cell source	9.00 10^{-2} day^{-1}	computed by imposing the steady state as explained in NK Eq. (2.7)

Table 2.3: Table of mouse PCa model parameters. The table provide the parameter estimates, with the corresponding descriptions, values and estimation procedure.

Chapter 3

A mathematical model of castration-resistant prostate cancer immunotherapy in humans

In this chapter we propose a mathematical model of human prostate cancer developing the castration-resistant form. The purpose of this contribution is to study the qualitative behavior of the system when different immunotherapies are administered, evaluating their effects for long times. Unlike the model presented in the Chapter 2, which has been calibrated on pre-clinical data, this work includes parameters estimated from literature human data. Therefore, this model represents an improvement in the direction of mathematical models as tool for supporting clinical decisions.

The model extends a previous one presented by Rutter and Kuang [24]. The authors described the CTL tumor inhibition and the mutation from Androgen Dependent Prostate Cancer (ADPC) cells to Androgen Independent Prostate Cancer (AIPC) cells, but they did not consider the capacity of the immune system to regulate immune reactions. In order to further increase the accuracy of the model in capturing the cancer dynamics, we include in the system the description of the immune-suppressive tumor microenvironment by means of the Treg cells. Moreover, in

addition to the androgen deprivation and dendritic cell vaccine considered in the Rutter and Kuang paper, we also include a treatment with the drug *ipilimumab*, a particular anti-CTLA4 currently under clinical trial for advanced prostate cancers (NCT03061539, NCT02985957).

This chapter mainly consists of the results included in the submitted work *"Modeling the effect of immunotherapies on human castration-resistant prostate cancer"*. The limitation and possible future extensions are discussed in the final Chapter 4.

3.1 Mathematical model

The presented mathematical model is composed of 8 ordinary differential equations describing the evolution in time of the following variables:

X_1: amount of androgen dependent prostate cancer cells (number of cells);

X_2: amount of androgen independent prostate cancer cells (number of cells);

C: amount of circulating CTLs (number of cells);

R: amount of circulating regulatory T cells (number of cells);

I_L: concentration of interleukin-2 in blood (ng/ml);

D: amount of circulating dendritic cells (number of cells);

A: concentration of androgen (ng/ml);

I_P: amount of *ipilimumab* (mg).

Figure 3.1 shows a schematic representation of the model-variable interactions. PCa is represented by its two forms. The ADPC grows stimulated by the androgens but, when the androgen level decreases as result of the androgen deprivation therapy, the ADPC undergoes apoptosis. However, the androgen reduction contributes to create an ideal microenvironment for AIPC cells proliferation. The CTL can counteract the tumor by killing both forms of cancer cells. The CTL

activity is down-regulated by the Treg cells, which inactivate them, allowing the tumor grow. The inteleukin-2 (IL-2) stimulates the activation of T cells, both Treg and CTL, which, however, are mainly activated by the dendritic cells.

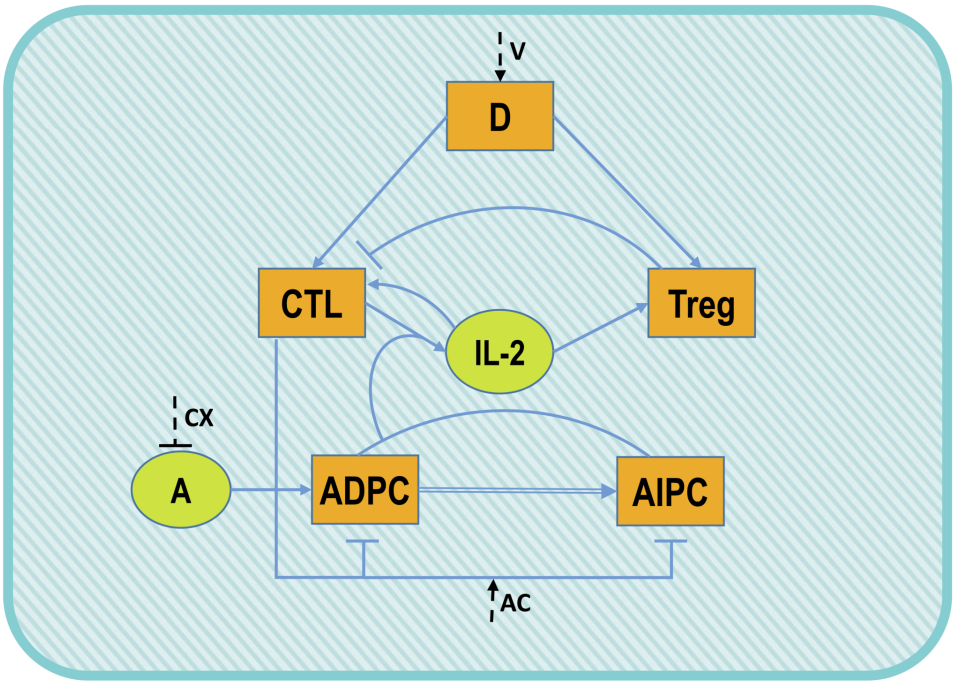

Figure 3.1: Human PCa model diagram. Cells are represented in orange squared boxes, while molecules in green rounded ones. The cancer is in its two forms: Androgen Dependent Prostate Cancer (ADPC) and Androgen Independent Prostate Cancer (AIPC). Other players involved: Dendritic cells (D), regulatory T cells (Treg), Cytotoxic T Lymphocytes (CTL), Androgens (A) and Interleukin-2 (IL-2). Double arrow represents transformations, single lines represent promotions and inhibitions, while dashed lines depict the three implemented treatments: androgen deprivation therapy (CX), vaccine (V) and anti-CTLA4 drug (AC).

The dashed lines in the diagram represent the treatments considered. We include androgen deprivation therapy (CX), vaccine (V), as an infusion of dendritic cells, and anti-CTLA4 drug (AC), with *ipilimumab*. Table 3.1 shows a schematic description of these treatments.

Therapy	Abbreviation	Description	Reference
androgen deprivation therapy	CX	chemical or surgical castration	[24]
vaccine	V	continuous administration of dendritic cells	[24]
anti-CTLA4	AC	single or multiple doses of 3 mg/kg of *ipilimumab*	[117]

Table 3.1: Table of the treatments for human PCa model. Summary of the treatments implemented in the mathematical model.

In the following we introduce the system equation. Eq. (3.1) describes the dynamics of ADPC cells:

$$\frac{dX_1}{dt} = \underbrace{r_1\ A\ X_1\ (1-\frac{X_1+X_2}{K})}_{\text{tumor proliferation}} - \underbrace{\mu_1\ (1-\frac{A}{a_0})\ X_1}_{\text{death}} - \underbrace{m_1\ (1-\frac{A}{a_0})X_1}_{\text{mutation}} - \underbrace{C\ X_1\ \left(\frac{e_{CX}}{g_{CX}+(X_1+X_2)}\ +\ k_{Ip}\ I_P\right)}_{\text{tumor killing by CTL}}. \tag{3.1}$$

The first term represents the tumor proliferation, which is supposed to be logistic according to [24], while the second one is the death term. We observe that both the proliferation and the death terms depend on the androgen concentration. Indeed, since the steady state value of the androgens is the basal level $a_0 = 30\ ng/ml$, in the untreated scenario, the tumor death rate is zero. On the contrary, when the castration is considered, the androgen level reaches a concentration close to zero and, accordingly, the proliferation rate decreases, while the death term increases, by determining the extinction of these cells. However, the androgen reduction increases the mutation rate ("mutation" term), which turns the ADPC into AIPD, describing the effect of the selective pressure due to the androgen deprivation therapy. The "tumor killing by CTL" term is composed by two expressions. The first describes the standard cytotoxic effect

of CTLs, which is negatively regulated by the amount of cancer cells as in [24], reflecting the tumor ability to bypass the immune control by reducing the CTL efficacy. Against this inhibition of the immune reaction, the second part of this term describes the anti-CTLA4 therapy, herein represented by the drug *ipilimumab*. We model the effect of this ICB treatment by enhancing the CTL tumor-killing capacity, according to biological evidences [96; 117]. Experimental studies, indeed, show an increasing number of tumor-infiltrating T cells after *ipilimumab* administration, thus intensifying the CTL-tumor interactions [118].

Eq. (3.2) refers to the AIPC cells:

$$\begin{aligned}\frac{dX_2}{dt} &= \underbrace{r_2\ X_2\left(1-\frac{X_1+X_2}{K}\right)}_{\text{tumor proliferation}} + \underbrace{m_1\ (1-\frac{A}{a_0})X_1}_{\text{mutation}} \\ &- \underbrace{C\ X_2\ \left(\frac{e_{CX}}{g_{CX}+(X_1+X_2)}\ +\ k_{Ip}\ I_P\right)}_{\text{tumor killing by CTL}}.\end{aligned} \tag{3.2}$$

In this case, the "tumor proliferation" term does not depend on the androgen level. The other terms replace those described above for the Eq. (3.1).

Eq (3.3) describes the CTL dynamics:

$$\frac{dC}{dt} = \underbrace{e_C\frac{D}{g_C+D}}_{\substack{\text{CTL activation}\\ \text{by } D_m}} + \underbrace{\frac{e_{IC}\ C\ I_L}{g_{IC}+I_L}}_{\substack{\text{CTL activation}\\ \text{by IL-2}}} - \underbrace{\mu_C\ C}_{\text{death}} - \underbrace{k_R\ C\ R}_{\substack{\text{CTL inactivation}\\ \text{by Treg}}}. \tag{3.3}$$

CTLs are activated by dendritic cells and IL-2 as described in the first two activation terms. The CTLs are either reduced by the death term or inactivated by Treg cells, as described by the last term. This inactivation term is supposed to be proportional to the amount of CTL and Treg cells by a mass action law.

The Treg dynamics is explained in Eq. (3.4):

$$\frac{dR}{dt} = \underbrace{a_R\ D}_{\substack{\text{Treg proliferation}\\ \text{by } D_m}} - \underbrace{\mu_R\ R}_{\text{death}} + \underbrace{a_{IR}\ I_L}_{\substack{\text{Treg proliferation}\\ \text{by IL-2}}} . \tag{3.4}$$

The first two terms reproduce the Treg proliferation and death as in Kronik *et al.*[119]. The last proliferation term has been included to describe the role of IL-2 in Treg activation [120].

The dedritic cells dynamics is described in Eq. (3.5):

$$\frac{dD}{dt} = \underbrace{s_D}_{\text{source}} + \underbrace{v}_{\text{vaccine}} - \underbrace{\mu_D\ D}_{\text{death}}. \tag{3.5}$$

Unlike the description provided in Rutter and Kuang paper [24], we considered that there is a baseline level of circulating dendritic cells due to the source term s_D. The last two terms, instead, are maintained from the original model, and they represent the effect of the vaccine and the death term, respectively. The vaccine is herein simulated as a constant infusion of dendritic cells and, when it is not administered, it is set to zero.

The Eq. (3.6) refers to the IL-2:

$$\frac{dI_L}{dt} = \underbrace{e_I\ \frac{C\ (X1 + X2)}{g_I + (X1 + X2)}}_{\substack{\text{IL-2 proliferation}\\ \text{by tumor and CTL}}} + \underbrace{\mu_I\ (i_0\ -\ I_L)}_{\text{proliferation and death}} . \tag{3.6}$$

The first term represents the IL-2 proliferation due to tumor cells and CTLs as described in [24]. The death term from [24] ($-\mu_I\ I_L$) has been slightly modified by the parameter i_0, which represents the baseline level of IL-2 in healthy condition .

The androgen Eq. (3.7) is the only equation maintained as in [24] without modifications:

$$\frac{dA}{dt} = \underbrace{\gamma_A\ (a_0\ -\ A)}_{\text{proliferation and death}} - \underbrace{\gamma_A\ a_0\ 1_{CX}}_{\substack{\text{androgen deprivation}\\ \text{effect}}} . \tag{3.7}$$

It shows two different behaviors of the androgen level according to the value of the boolean function 1_{CX}, which is set to 1 when the the androgen deprivation therapy is considered, otherwise is set to 0. Indeed, when $1_{CX} = 0$, the equation becomes:

$$\frac{dA}{dt} \; = \; \gamma_A(a_0 \; - \; A),$$

which maintains the derivative equal to zero as $A(0) = a_0$. Conversely, when $1_{CX} = 1$, the androgen level exhibits an exponential decay with rate γ_A.

Eq. (3.8) describes the variation in time of the drug *ipilimumab*, which is the anti-CTLA4 considered in our model:

$$\frac{dI_p}{dt} = - \underbrace{\lambda_P \; I_p}_{\substack{\text{ICB} \\ \text{degradation}}} \quad . \tag{3.8}$$

This drug is supposed to degrade with a rate λ_P. At the times of *ipilimumab* administration, we assumed that the value of I_p is instantaneously increased of a fixed amount corresponding to the dosage.

In addition to the PCa dynamics and its interactions with the immune system, the model describes the evolution of the Prostate Specific Antigen (PSA) concentration, which is supposed to be linear with the amount of cancer cells, in accordance with other modeling approaches [24; 121; 122]:

$$PSA(t) \; = \; c_{PSA} \; (X_1(t) \; + \; X_2(t)). \tag{3.9}$$

3.2 Model calibration

Before estimating the model parameter, we performed an *a priori* structural identifiability analysis by the Matlab toolbox GenSSI [84], which guaranteed the global parameter identifiability (see technical detail in Section 2.5). In the following, we explain in detail, for each equation, the estimation procedure for the parameter identification. For a complete overview of the parameter estimations we refer to the Table 3.5.

Eq. (3.1) and (3.2) The prostate tumor is represented by two different equations describing the dynamics of ADPC and AIPC. The proliferation, death and mutation rates of both ADPC and AIPC cells are taken from the original model [24], but we changed the estimate of the parameter K, expressing the tumor carrying capacity. Following the procedure exposed by Rutter and Kuang [24], we adapted the parameter K to the experimental data used for model calibration. Indeed, the authors considered K as a ratio between the average prostate weight (11 mg) and the average prostate cells weight (1 ng). However, the average prostate weight in patients with advanced castration-resistant prostate cancer is often higher than 11 mg, as reported in several papers [123–125]. We extrapolated this information from [124] in which the prostate volume is associated with the Gleason score (GS), an indicator of the aggressiveness of cancer (high GS value corresponds to aggressive cancer). We fixed the GS as 8 (the higher GS considered in that paper) and we observed in the Figure 2 of [124] the column corresponding to the major percentage of patients with GS = 8. We found that the prostate volume is between 100 cm^3 and 114.9 cm^3, thus we consider the average value of 107 cm^3. Since the prostate volume is a good approximation of the prostate weight [126], 107 cm^3 = 107 g. Therefore:

$$K = 107\ 10^9 cells.$$

This constant K represents a saturation for cancer cell growth , because we supposed that the tumor reaches its maximal expansion occupying the most of the prostate volume in the high stage of disease.

The parameters regarding the CTL tumor killing capacity in untreated condition was also maintained as in [24]. However in our model we added the description of the anti-CTLA4 treatment, which increases the activity of the immune reaction against the tumor. To include this treatment, we considered the Small *et al.* paper [117]. This study involved patients with metastatic castration-resistant prostate cancer treated with a single dose of *ipilimumab* of 3 mg/Kg. Since Small *et al.* did not observe an increment in CTL number in peripheral blood (Figure 1.B in [117]), we reproduced the effect of *ipilimumab* as an increasing in the CTL tumor-killing capac-

ity. Therefore, we added a term in the tumor equations, which is proportional to the amount of drug, the number of CTL and the number of tumor cells by a parameter k_{Ip}. To estimate this parameter, we considered data extrapolated from Figure 3 in [117], showing the variation in time of PSA of the two patients with major PSA decline after the *ipilimumab* infusion. We collected data from day 7 (when a dose of *ipilimumab* was injected) to the second month. Then, we computed the mean values reported in Table 3.2. To estimate k_{Ip}, we set the initial values

Time (day)	**PSA** ($\frac{ng}{mL}$)
7	31.31
14	22.35
28	26.18
60	18.14

Table 3.2: Experimental data used for human PCa model calibration. The mean values for the PSA level registered in the two patients reported in the Figure 3 of [117].

according to the experimental protocol followed by Small *et al.*. They considered patients subject to androgen deprivation therapy with advanced castration-resistant prostate cancer that, in our model, means a small value for $X_1(0)$ and $A(0)$. To evaluate the amount of castration-resistant cancer cells, we focused on the PSA level registered at the time of injection in Figure 3 of [117] and we use the Eq. (3.9) to calculate the total amount of cancer cells:

$$X_1(0) + X_2(0) = \frac{PSA(0)}{c_{PSA}} = \frac{31.31}{1.93\ 10^{-9}} = 16.2\ 10^9\ cells. \tag{3.10}$$

Once we fixed the amount of androgen and cancer cells, we simulated the system with androgen deprivation therapy (see the blue line in Figure 3.4) and we checked the values of the other variables at the time point in which the total tumor corresponds to $16.2\ 10^9\ cells$. Precisely, we set:

$$X_1(0) = 0.0001\ 10^9\ cells, \quad X_2(0) = 16.2227\ 10^9\ cells, \quad C(0) = 2.79\ 10^4\ cells,$$

$$R(0) = 2.103\ 10^9\ cells; \quad D(0) = 4.26\ 10^7\ cells,$$

$$I(0) = 0.01161\ ng/mL, \quad A(0) = 0.0001\ ng/mL.$$

In order to define the *ipilimumab* dose, we needed the average weigh of patients considered in the Small *et al.* experiments [117]. Although the authors did not include the patient weights in their study, they reported the median age (70 years) and race, divided in Caucasian (86%) and Hispanic (14%). By considering these characteristics, we focused on Fryar *et al.* paper [127] that compare the mean body weight over the last years. We fixed the average weights of men around 70 years old and we computed the weighted arithmetic mean taking into account the percentages of Caucasian and Hispanic men in Small *et al.* experiment as:

$$W \ = \ w_C\ 0.86 \ + \ w_H\ 0.14 \ = \ 88.5\ kg. \tag{3.11}$$

Therefore, we found $I_p(0) = 3\ mg/kg\ 88.5\ kg \ = \ 265.5\ mg$.

Simulating the system with the anti-CTLA4 therapy, we minimized the weighted square differences between the model output and the data in Table 3.2, obtaining the estimate $k_{Ip} = 5.44\ 10^{-9} \frac{1}{day\ mg\ cells}$. The data fit is shown in Figure 3.2.

Eq. (3.3) The parameters regulating the first three terms has been maintained as in the original model [24]. However, our model includes the regulative term representing the CTL inactivation mediated by Treg cells: $-k_R\ R\ C$.

To estimates k_R, we considered a *no-tumor* equilibrium point, from de Pillis *et al.* [21]:

$$C_0 = 2.4\ 10^4 cells/L, \quad R_0 = 1.1\ 10^8 cells/L, \quad I_0 = 2.99\ 10^{-3} ng/mL,$$

and we set the baseline of androgen as $A_0 = 30 ng/mL$, according to [24]. For the baseline level of dendritic cells, instead, we referred to Fearnley *et al.* [128], in which is reported $D_0 = 9.8\ 10^6 cells/L$. We considered an average blood volume of 5 L to convert these concentrations in

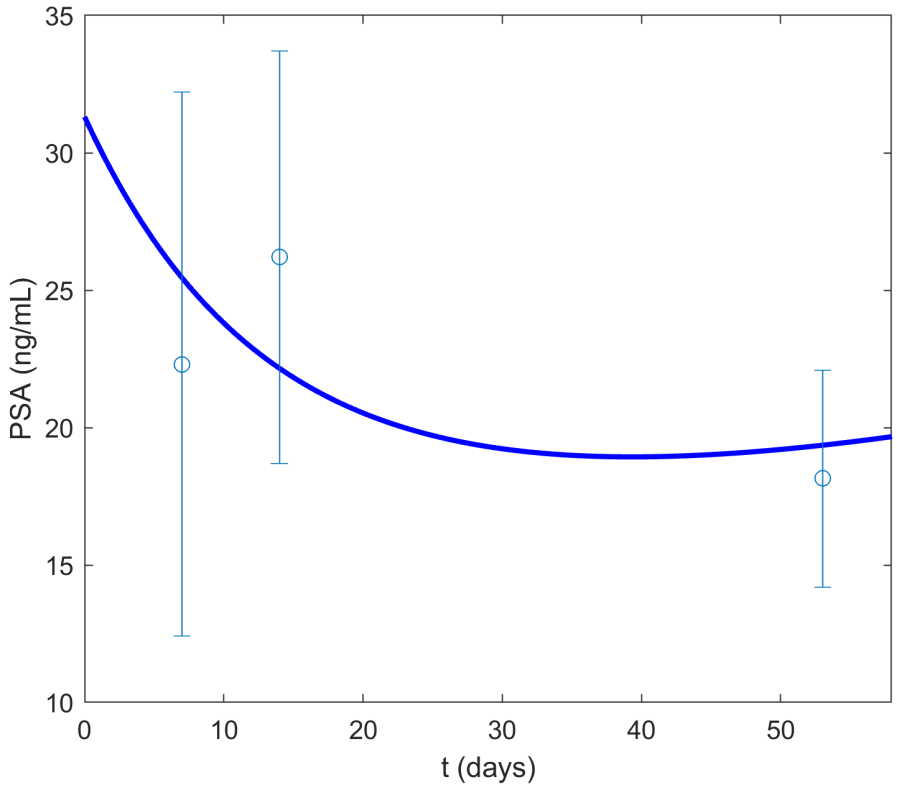

Figure 3.2: Human PCa model fitting experimental data. The model predicted PSA dynamics in case of treatment with *ipilimumab*. The experimental data taken from Figure 3 in Small *et al.* paper [117] are reported as points with the relative error bars.

number of cells::

$$C_0 = 1.2\ 10^5 cells; \quad R_0 = 5.5\ 10^8 cells; \quad D_0 = 4.9\ 10^7 cells; \tag{3.12}$$

$$I_0 = 2.99\ 10^{-3} ng/mL; \quad A_0 = 30 ng/mL.$$

Therefore, we imposed:

$$\dot{C} = 0 \iff \frac{e_C\ D_0}{g_C + D_0} - \mu_C\ C_0 + C_0 \frac{e_{IC} I_0}{g_{IC} + I_0} - k_R\ R_0\ C_0 = 0$$

from which $k_R = 32.81\ 10^{-9}\ (cells\ d)^{-1}$.

Eq. (3.4) The first two terms in the Treg equation are taken from Kronik *et al.* model [119]. The authors explored the prostate cancer growth by means of its interactions with the immune system, represented by dendritic cells, CTL and Treg cells, and they described the latter by the equation:

$$\dot{R} = a_R D_R - \mu_R R,$$

where D_R represents the regulatory dendritic cells. Kronik *et al.* did not consider the IL-2, which is included in our starting model and has a role in Treg activation and functions [120]. In order to describe this regulation, we added the "Treg proliferation by IL-2" term in the Treg equation. We assumed that the presence of IL-2 stimulates the production of Treg by a mass action term like other mathematical models [23; 129; 130].

The two parameters a_R and μ_R are estimated by Kronik *et al.* from the literature. The rate of Treg proliferation induced by dendritic cells, a_R, has been computed considering that the dendritic cells induce the activation of 0.36 Treg cells in 120 hours [131], so $a_R \approx 3\ 10^{-3}\ h^{-1} = 0.072\ d^{-1}$. The death rate of Treg cells, μ_R, has been approximated by fitting data from [132]. They obtained $a_R \approx 3\ 10^{-2}\ h^{-1} = 0.72\ d^{-1}$. The parameter a_{IL}, regarding the activation rate of Treg by the IL-2, is estimated by imposing the *no-tumor* steady state (3.12). Therefore, we obtained:

$$\dot{R} = 0 \quad \Longleftrightarrow \quad a_R\ D_0 - \mu_R\ R_0 + a_{IL}\ I_0 = 0$$

from which $a_{IL} = 131.26\ 10^9\ \frac{cells}{d}\ \frac{mL}{ng}$.

Eq. (3.5) and (3.6) In order to make consistent our system with the *no-tumor* steady state (3.12), we modified the dendritic and IL-2 equations taken from [24]. We supposed that there is a baseline level for both dendritic cells and IL-2 in healthy conditions. To describe this, we added the source term s_D in the Eq. (3.5) and i_0 in the Eq. (3.6), computed by imposing the *no-tumor* steady state (3.12) : $s_D = 0.686\ 10^7\ \frac{cells}{d}$ and $i_0 = 2.99\ 10^{-3} ng/mL$.

Eq. (3.7) The equation regarding the androgen level has been taken from [24] without changing the single terms or parameters.

Eq.(3.8) The degradation rate of the drug *ipilimumab* has been computed following the standard approach as:

$$\lambda_P = \frac{ln(2)}{t_{1/2}},$$

where $t_{1/2} = 12.5$ days is the *ipilimumab* half-life [117].

Eq. (3.9) We supposed that the PSA is linearly correlated with tumor volume, as in [24; 121; 122], so:

$$PSA(t) \;=\; c_{PSA}\;(X_1(t) + X_2(t)). \tag{3.13}$$

We estimated the value of c_{PSA} according to biological data from Konyaliouglu *et al.* paper [125]. The authors measured the average PSA level and tumor volume in prostate cancer patients as 10.6 ng/mL and 5.5 cm^3, respectively. Since the volume and the prostate weight are close [126], by considering the average weight of a cells as 1 ng [24], we computed the average amount of prostate cancer cells as:

$$(X_1 + X_2)_M \;=\; \frac{5.5\ g}{10^{-9}\ g} \;=\; 5.5\ 10^9 cells,$$

therefore:

$$c_{PSA} \;=\; \frac{PSA_M}{(X_1 + X_2)_M} \;=\; \frac{10.6}{5.5\ 10^9}\frac{ng}{mL\ cells} \;=\; 1.93\ 10^{-9}\frac{ng}{mL\ cells}.$$

3.3 Model simulations and sensitivity analysis

The presented mathematical model can be used as a tool for simulating different scenarios. We set the simulation time to 7 years in order to reach the steady state for all the model variables and to study the effect of the therapies for long times.

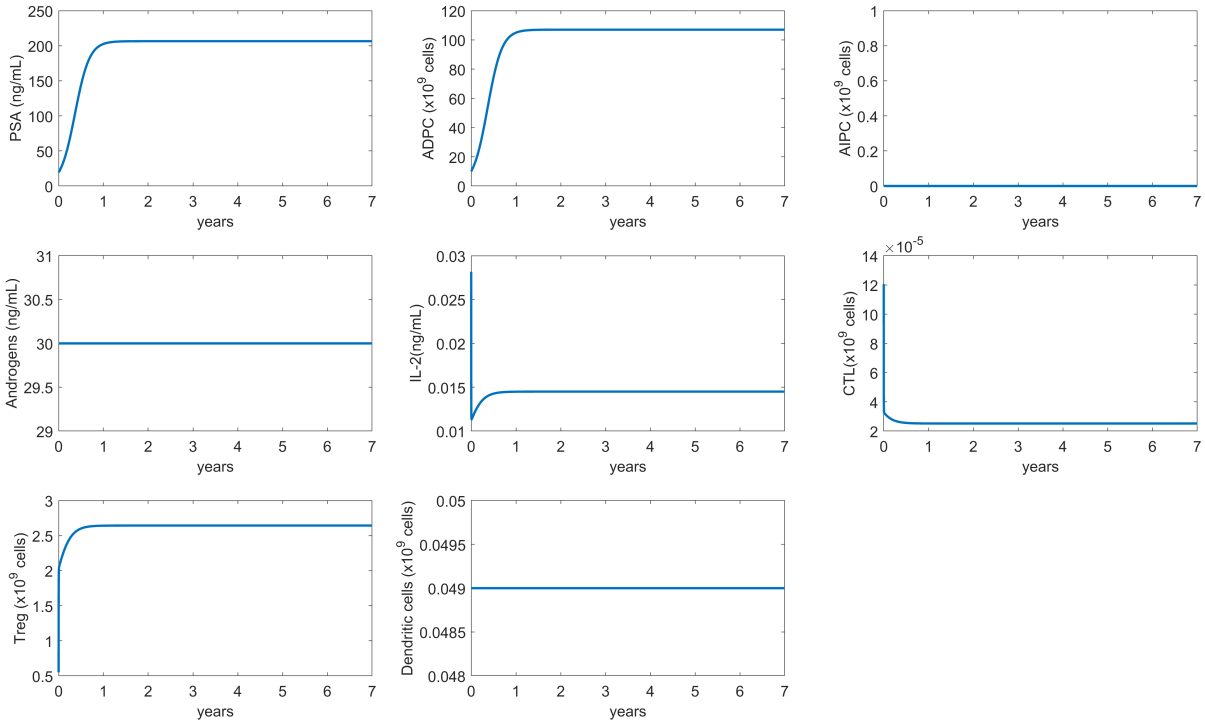

Figure 3.3: Human PCa model dynamics in untreated case. Dynamics of the system variables and PSA level without any treatment.

In the untreated case (Fig. 3.3), the predicted PSA level quickly reaches its maximal concentration, which means that the tumor grows, filling the most of the prostate volume. We observe that, without the castration therapy, the androgen level remains constant and the AIPC does not evolve, so the production of PSA is mainly due to the ADPC cells. The immune system reaches a steady state, which is the consequence of immunosuppressive mechanisms. Indeed, compared to the initial values corresponding to the *no-tumor* steady state, the CTLs decrease and the Treg cells increase stimulated by the tumor.

Our model includes three different therapies: androgen deprivation therapy, dendriric cell vaccine and anti-CTLA4. We consider the androgen deprivation therapy and its combination with the other two, because we are interested in evaluating the effects of the immunotherapies on the AIPC form, which is assumed to develop after androgen deprivation therapy.

Figure 3.4 shows the dynamics in case of both androgen deprivation therapy (blue lines) and

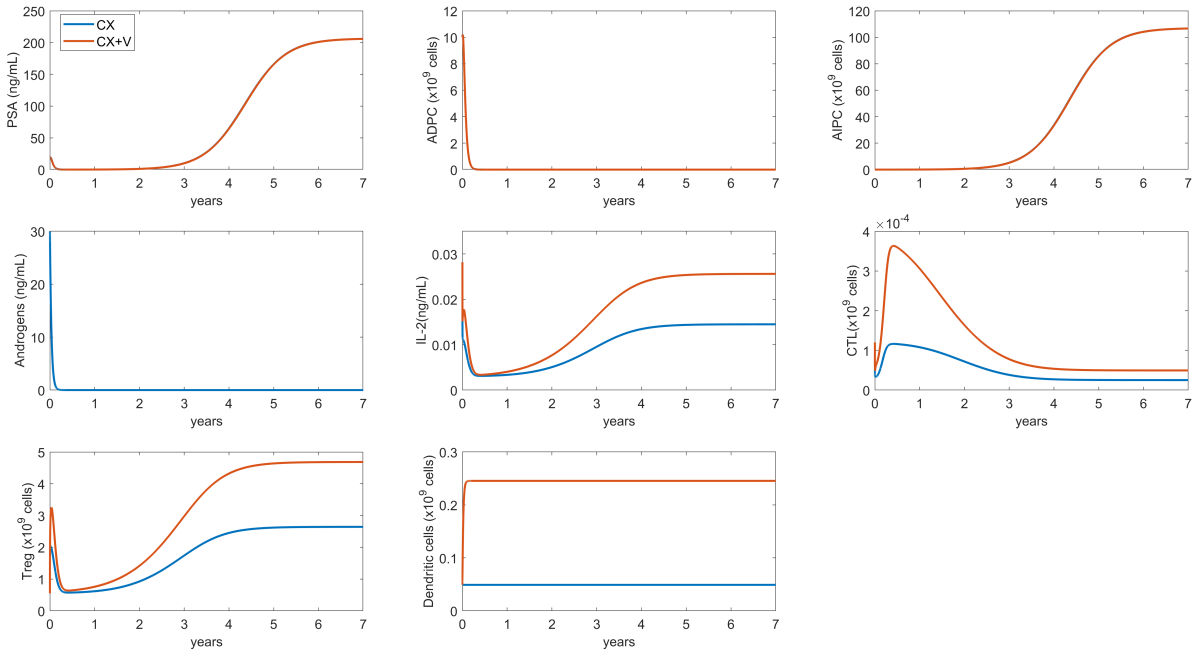

Figure 3.4: Human PCa model dynamics under androgen deprivation therapy and under androgen deprivation + vaccine combination therapy. Dynamics of the system variables and PSA level under androgen deprivation therapy (blue lines) and under androgen deprivation and vaccine combined therapy (orange lines).

in combination with dendritic vaccine (orange lines). Unlike the untreated case, the androgen deprivation leads to an initial reduction in PSA level as the ADPC cells undergo apoptosis, according to the reduction of the androgen level. The castration also promotes an immune reaction, by increasing the number of CTLs and by reducing the amount of Treg cells. However, the tumor develops into the AIPC form, which proliferates in an ideal environment deprived of androgens, and then the tumor volume starts to increase, producing PSA. Over the simulation time, the *high-tumor* steady state is reached, confirming that, when the AIPC cells develop, the androgen deprivation therapy does not lead to a tumor eradication. The presence of the dendritic cell vaccine does not change the scenario observed when only the castration is considered, except for an increasing in immune cell production.

The effect of the combination of androgen deprivation and anti-CTLA4 therapies is showed in Figure 3.5. Since the *ipilimumab* has a half-life of 12.5 days [117], this drug quickly degrades.

Therefore, we administered this therapy after the evolution of AIPC to observe its tumor inhibitory effect. At the time of *ipilimumab* infusion (highlighted in the charts with a red line), we can see a reduction of AIPC cells. However, this is not enough to control the tumor growth: after a while the AIPC starts increasing again and the system reaches the *high-tumor* steady state.

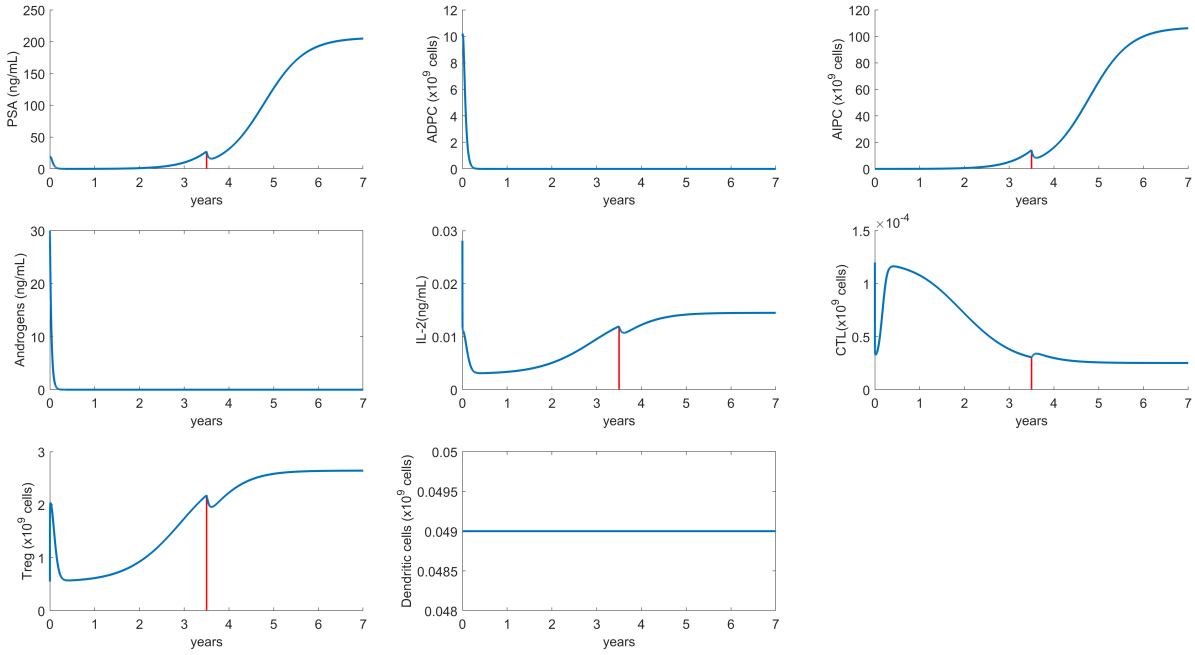

Figure 3.5: Human PCa model dynamics under androgen deprivation + single anti-CTLA4 combination therapy. Dynamics of the system variables and PSA level when androgen deprivation and anti-CTLA4 combined therapy is administered. The red line in the charts indicates the *ipilimumab* administration time.

The promising predicted effect of the anti-CTLA4 treatment and the rapid degradation of the drug *ipilimumab* suggest us that an intermittent administration protocol could be efficacious in the tumor control. In the literature there are clinical trials involving intermittent administration of *ipilimumab*, often combined with other therapies [133]. In particular, the study by Slovin *et al.* [134] evaluates the efficacy of drug escalating doses of ipilimumab, alone or in combination with radiotherapy, on patients with metastatic castration-resistant prostate cancer. The patients were treated with 3, 5 or 10 $\frac{mg}{kg}$, infused every 3 weeks for 4 doses. In order to reproduce this protocol, we needed to set the corresponding initial condition. To allow the tumor cells to proliferate as

AIPC, we simulated the system by imposing androgen deprivation therapy ($1_{CX} = 1$ in Eq. (3.7)). Thus, we detected the values for all the model variables according to the baseline PSA registered by Slovin *et al.*. Although this PSA values were different for each group of patients, to compare the efficacies of escalating dosage, we arbitrary set the initial state according to the baseline PSA of $91\frac{ng}{ml}$ detected in patients treated with low dosage ($3\ \frac{mg}{kg}$). Through this procedure, we found the following initial states for the model variables:

$$X_1 = 0\ cells; \qquad X_2 = 4.7 \cdot 10^10\ cells; \qquad C = 2.63 \cdot 10^4\ cells; \qquad R = 2.53 \cdot 10^10\ cells;$$
$$I_L = 1.38 \cdot 10^{-2}\ \frac{ng}{ml}; \qquad D = 4.9 \cdot 10^7\ cells; \qquad A = 0\ \frac{ng}{ml}.$$

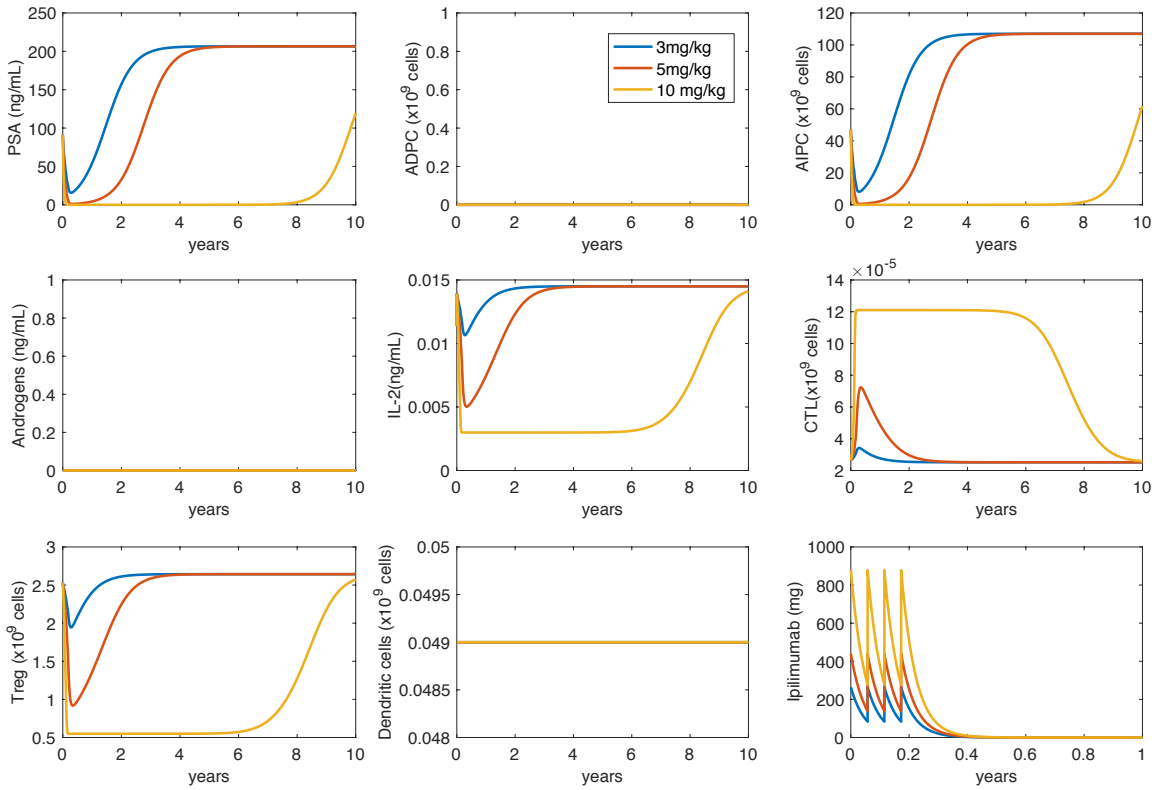

Figure 3.6: Human PCa model dynamics under intermittent anti-CTLA4 on castrated patients. Dynamics of the system variables and PSA level intermittent anti-CTLA4 combination therapy is administered on castrated patients. The simulations reproduce the experimental protocol proposed by Slovin *et al.* [134] (2013).

Figure 3.6 shows the numerical results for intermittent administration of *ipilimumab* by following the clinical trial proposed in Slovin *et al.* work [134]. The model predicts that low and medium doses of *ipilimumab* are not enough to arrest the tumor growth. When the intermittent administrations end, the tumor mass growths by reaching the high-tumor steady state. By increasing the dose of 10 $\frac{mg}{kg}$, the model predicts a sort of cancer dormancy. In fact, the tumor seems to be eradicated for years, until it starts increasing again, with an uncontrollable tumor growth.

Encouraged by the positive results obtained by implementing intermittent administration of anti-CTLA4, we reproduced an intermittent protocol repeated for years, coupled with the androgen deprivation therapy, in order to realize a long-term therapy which could be able to keep the tumor under control. Therefore, we simulated the system with one low-dose injection of *ipilimumab* per year, reproduced in Figure 3.7.

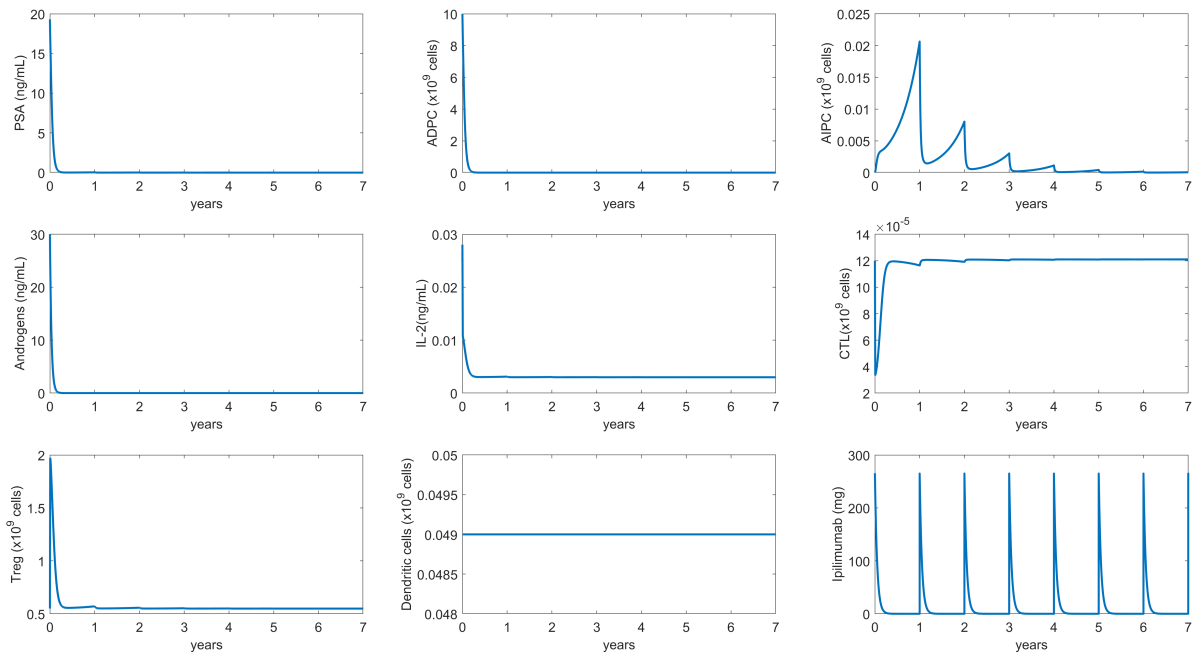

Figure 3.7: Human PCa model dynamics under androgen deprivation + long-term intermittent anti-CTLA4 combination therapy. Dynamics of the system variables and PSA level when androgen deprivation and long-term intermittent anti-CTLA4 combination therapy is administered. The subject receives one injection of 3 mg/kg of *ipilimumab* per year.

The model predictions provided in Figure 3.7 show a tumor reduction and all the variables of the system move close to the *no-tumor* steady state. One infusion per year for 7 years allows the control of tumor growth but it is not enough to eradicate the cancer. Indeed, by increasing the simulation time, the model suggests that, after some years, the AIPC proliferates and the system reaches again the *high-tumor* steady state. However, by extending the proposed intermittent therapy to 22 years, the *no-tumor* steady state becomes attractive, thus determining the extinction of tumor cells (see Figure 3.12).

In order to investigate the dependence of the model dynamics on these parameter estimates, we performed a Local Sensitivity Analysis (LSA). The corresponding results are shown in Appendix B. The LSA highlights the obvious high dependence of tumor on its death and proliferation rates, as well as on the tumor carrying capacity, in all the reproduced experimental scenarios. The tumor is also predicted to be influenced by the estimated parameter k_{I_P}, representing the CTL tumor killing rate due to the *ipilimumab* infusion, when the anti-CTLA4 therapy is administered. Moreover, the tumor shows a dependence on the androgen baseline level and their turnover rate, which decreases by increasing the simulation time (Figures B.1 and B.2).

3.4 Model reduction

In order to use more efficiently the qualitative analysis methods, we moved to a reduced model with constant parameters. First of all, we assumed that also *ipilimumab* is administered with a constant infusion, substituting (8) with

$$\frac{I_p}{dt} \;=\; d_P \;-\; \lambda_P I_p. \tag{8'}$$

In order to define the constant dosage for the drug *ipilimumab*, we focused on the proposed long-term therapy, corresponding to one injection per year. We have seen that, maintaining a dose of 265.5 mg of *ipilimumab* per year, but administering the drug with a constant infusion of $d_P = 0.737 mg/day$, the system dynamics observed in Figure 3.7 do not change (see Figure 3.14).

Therefore, we can consider constant infusion for long-term therapies without loss of generality.

We was interested in looking the evolution of castration-resistant cancer cells, that, in our model, develop after androgen deprivation therapy, thus we set this as the mainstay treatment. The androgen equation than becomes $\frac{dA}{dt} = -\gamma_A\ A$. Moreover, we observed that dendritic cells, interleukin 2 and androgens vary in time scales shorter that the one of the other cell populations, as shown in [24], as well as the drug *ipilimumab*. Since our modifications of the Rutter and Kuang's model did not impact on the time scale, we followed the procedure described in [24], by assuming a quasi-steady state (QSS) for these variables, which means:

$$\frac{dA}{dt} = 0 \quad \Longrightarrow \quad A^* = 0;$$

$$\frac{dD}{dt} = 0 \quad \Longrightarrow \quad D^* \ = \ \frac{s_D + v}{\mu_D};$$

$$\frac{dI_L}{dt} = 0 \quad \Longrightarrow \quad I_L(C, X_1, X_2) \ = \ i_0 \ + \ \frac{e_I\ C\ (X_1 + X_2)}{\mu_I\,(g_I + (X_1 + X_2))};$$

$$\frac{dI_p}{dt} = 0 \quad \Longrightarrow \quad I_p^* \ = \ \frac{d_P}{\lambda_P};$$

where the star notation indicates the variables becoming constant.

The obtained QSS-system is:

$$\begin{cases} \frac{dX_1}{dt} \ = -\mu_1\ X_1 \ - m_1\ X_1 \ - \frac{e_X\ C\ X_1}{g_X + (X_1 + X_2)} \ - \ k_{Ip}\ I_P^*\ C\ X_1, \\ \\ \frac{dX_2}{dt} \ = r_2\ X_2\left(1 - \frac{X_1 + X_2}{K}\right) \ + \ m_1\ X_1 \ - \frac{e_X\ C\ X_2}{g_X + (X_1 + X_2)} \ - \ k_{Ip}\ I_P^*\ C\ X_2, \\ \\ \frac{dC}{dt} \ = \ s_C \ - \ \mu_C\ C + \frac{C\ I_L(C, X_1, X_2)\ e_{IC}}{g_{IC} + I_L(C, X_1, X_2)} \ - \ k_R\ C\ R, \\ \\ \frac{dR}{dt} \ = \ s_R \ - \ \mu_R\ R \ + a_{IR}\ I_L(C, X_1, X_2), \end{cases}$$

where the source terms are:

$$s_R = a_R\ D^*, \tag{3.14}$$

$$s_C = e_C \frac{D^*}{g_C \ + \ D^*}. \tag{3.15}$$

We also observed that, in the androgen deprivation scenario, $\lim_{t\to\infty} X_1(t) = 0$ and $\frac{dX_1}{dt} < 0$, thus the limiting system (LS) is:

$$\begin{cases} \frac{dX_2}{dt} \ = r_2 \ X_2 \left(1 - \frac{X_2}{K}\right) \ - \frac{e_X \ C \ X_2}{g_X + X_2} \ - \ k_{Ip} \ I_P^* \ C \ X_2, \\ \\ \frac{dC}{dt} \ = \ s_C \ - \ \mu_C \ C + \frac{C \ I_L(C,0,X_2) \ e_{IC}}{g_{IC} + I_L(C,0,X_2)} \ - \ k_R \ C \ R, \\ \\ \frac{dR}{dt} \ = \ s_R \ - \ \mu_R \ R \ + a_{IR} \ I_L(C,0,X_2). \end{cases} \tag{LS}$$

We was interested in studying the equilibrium points, therefore we focused on the (LS) without loss of generality. To verify that the (LS) is a good approximation of our model, we plotted the solutions of the complete system versus the (LS) in Figure 3.8. For long times the solutions overlap, thus we studied the equilibrium points of the (LS).

3.5 Equilibrium points

In this section we perform a qualitative analysis of the (LS). We further analyze the equilibrium points, their stability and how these change with respect to the tumor proliferation rate. We analytically find a *no-tumor* equilibrium point and the conditions that ensure its stability. However, when the tumor is present, the simulations show another *high-tumor* equilibrium point. We study the stability of this numerical equilibrium by using MatCont [77], a Matlab toolbox that allows us to analyze the character of the equilibrium point by changing a fixed parameter. We evaluate how the system behavior changes when the immunotherapies are administered to assess which therapy leads to a major effect on tumor proliferation and we discuss these results from a biological point of view. All the immunotherapies considered in this analysis have been administered with continuous infusions, in order to avoid drug degradation and to allow the steady state analysis.

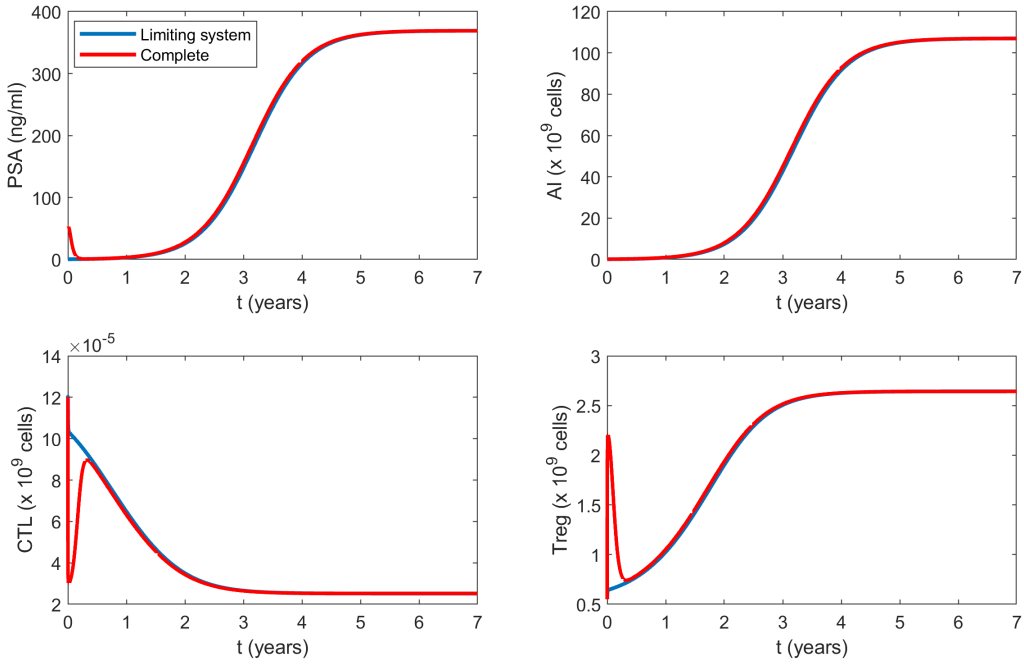

Figure 3.8: Human PCa model dynamics - complete system versus limiting system. Long time simulations for the complete system dynamics (red line) compared to the limiting system dynamics (blue line).

3.5.1 No-tumor equilibrium point

To compute the equilibrium point without tumor, we set $X_2 = 0$ in the (LS), and then we calculated the other variable steady-states:

$$\dot{C} = 0 \quad \Longleftrightarrow \quad s_C - \mu_C\, C + \frac{C\; I_L(C,0,X_2)\; e_{IC}}{g_{IC} + I_L(C,0,X_2)} - k_R\, C\, R = 0,$$

$$\dot{R} = 0 \quad \Longleftrightarrow \quad s_R - \mu_R\, R + a_{IR}\, I_L(C,0,X_2) = 0.$$

We observed that, in this condition and without any treatment, $I_L(C,0,0) = i_0$, $I_P^* = 0$, $v = 0$ and $D^0 = s_D/\mu_D = 0.049\ 10^9 cells$. The other variables of (LS) are:

$$R^0 = \frac{s_R + a_{IR}\, i_0}{\mu_R}$$

and

$$C^0 = \frac{s_C}{\mu_C + k_R R^0 - \frac{i_0\ e_{IC}}{g_{IC}+i_0}}\ , \tag{3.16}$$

where $C^0\ >\ 0$ only if $\mu_C + k_R R_0 > \frac{i_0\ e_{IC}}{g_{IC}+i_0}$, condition verified for our parameter estimates. Then, the *no-tumor* equilibrium point is

$$E_0\ =\ (X_2^0,\quad C^0,\quad R^0)\ =\ (0,\quad 1.2\cdot 10^5,\quad 5.5\cdot 10^8).$$

In order to study the stability of the *no-tumor* equilibrium point we evaluated the jacobian matrix in E_0:

$$J(E_0) = \begin{pmatrix} r_2 - \frac{e_X C^0}{g_X} & 0 & 0 \\ ... & -\mu_C - k_R R^0 + \frac{i_0 e_{iC}}{g_{IC}+i_0} & -k_R C^0 \\ ... & 0 & -\mu_R \end{pmatrix} \tag{3.17}$$

and the roots of its characteristic polynomial, which are:

$\lambda_1 = -\mu_R$;

$\lambda_2 = \frac{i_0 e_{Ic}}{g_{IC}+i_0} - \mu_C - k_R R^0$;

$\lambda_3 = r_2 - \frac{e_X C^0}{g_X}$.

We note that $\lambda_1 < 0$ and also $\lambda_2 < 0$ when C^0 exists, according to Eq. (3.16). Therefore, the *no-tumor* equilibrium point is stable if

$$r_2\ <\ \frac{e_X C^0}{g_X},$$

which, from a biological point of view, means that the tumor proliferation rate must be less than the CTL tumor killing capacity.

This condition allowed us to analyze the qualitative behavior of E_0 with respect to the tumor proliferation rate r_2. The equilibrium point changes its stability when the tumor proliferation

rate reaches the critical threshold $r^*_{BP} = \frac{e_X C^0}{g_X}$: for $r_2 < r^*_{BP}$ the *no-tumor* equilibrium point is stable, otherwise is unstable.

The point r^*_{BP} is associated to a transcritical bifurcation. To prove this, we followed the Boldin's approach [135], by adapting her results to our system. To this scope, we grouped the variables of the system (LS) into an invading population, composed of the tumor cells X_2 and a resident community composed of immune system cells $z = (C, R)$. Therefore, (LS) can be re-written as:

$$\begin{cases} \frac{dX_2}{dt} = G(X_2, z, r_2)X_2 \\ \frac{dz}{dt} = h(X_2, z, r_2) \end{cases} \tag{3.18}$$

where $G \in \mathscr{C}^1(\mathbb{R} \times \mathbb{R}^2 \times \mathbb{R}, \mathbb{R})$ and $h \in \mathscr{C}^1(\mathbb{R} \times \mathbb{R}^2 \times \mathbb{R}, \mathbb{R}^2)$ are defined as follows:

$$G(X_2, z, r_2) = r_2 \left(1 - \frac{X_2}{K}\right) - \frac{e_X C}{g_X + X_2}, \tag{3.19}$$

and

$$h(X_2, z, r_2) = h(X_2, z) = \begin{bmatrix} h_1(X_2, z) \\ h_2(X_2, z) \end{bmatrix} = \begin{bmatrix} s_C - \mu_C C + \frac{e_{IC} C I_L(C,0,X_2)}{g_{IC} + I_L(C,0,X_2)} - k_R\ C\ R \\ s_R - \mu_R R + a_{IR} I_L(C, 0, X_2) \end{bmatrix}. \tag{3.20}$$

Let us consider the equilibrium $E_0 = (0, z_0) = (0, C^0, R^0)$, and therefore, we linearize the system around E_0 by writing the Jacobian as:

$$J(0, z_0, r_2) = \begin{pmatrix} G(0, z_0, r_2) & 0 \\ h_{X_2}(0, z_0) & h_z(0, z_0) \end{pmatrix}, \tag{3.21}$$

where $h_{X_2}(0, z_0) = \frac{\partial h}{\partial X_2}(0, z_0)$ and $h_z(0, z_0) = \frac{\partial h}{\partial z}(0, z_0)$. Hence, the spectrum of the matrix (3.21) will be $\sigma(J(E_0, r_2)) = \sigma(G(E_0, r_2)) \cup \sigma(h_z(E_0))$. In particular, $\sigma(G(E_0, r_2))$ only contains the eigenvalue $\lambda = G(E_0, r_2) = r_2 - \frac{e_X C^0}{g_X} = r_2 - r^*_{BP}$. We can now prove that for $r_2 = r^*_{BP}$ a transcritical bifurcation occurs, by the following theorem:

Theorem 1. *Consider the system (3.18), such that there is an equilibrium $E_0 = (0, z_0)$ and for $r_2 = r^*_{BP}$, $\lambda = 0 \in \sigma(J(E_0, 0))$. Let $\frac{d}{dr_2}\left(G(E_0, r_2)\right)|_{r_2 = r^*_{BP}} > 0$, i.e. the function crosses the origin with non-zero derivative, and*

$$\frac{1}{2}M = \frac{\partial G}{\partial X_2}(E_0, r^*_{BP}) - \sum_{k=1}^{2} \frac{\partial G}{\partial z_k}(E_0, r^*_{BP}) \left(H_z^{-1} H_{X_2}\right)_k, \tag{3.22}$$

where $H_z = h_z(E_0)$ and $H_{X_2} = h_{X_2}(E_0)$. Therefore:

(i) if $M > 0$ there exists a positive equilibrium branch corresponding to a locally asymptotically stable steady state of the system (3.18), i.e. there is a supercritical transcritical bifurcation;

(ii) if $M < 0$ there exists a positive equilibrium branch corresponding to an unstable steady state of the system (3.18), i.e. there is a subcritical transcritical bifurcation.

In order to use this result, we evaluated:

$$\frac{d}{dr_2}\left(G(E_0, r_2)\right)|_{r_2 = r^*_{BP}} = 1 > 0,$$

$$\frac{\partial G}{\partial X_2}(E_0, r^*_{BP}) = r^*_{BP}\left(\frac{1}{g_X} - \frac{1}{K}\right),$$

$$\frac{\partial G}{\partial C}(E_0, r^*_{BP}) = -\frac{e_X}{g_X}, \quad \frac{\partial G}{\partial R}(E_0, r^*_{BP}) = 0$$

$$H_z^{-1} = \begin{bmatrix} \frac{1}{\beta} & \frac{-k_R R^0}{\mu_R \beta} \\ 0 & -\frac{1}{\mu_R} \end{bmatrix},$$

where $\beta = -\mu_C + \frac{i_0 e_{IC}}{g_{IC} + i_0} - k_R R^0$,

$$H_{X_2} = \begin{bmatrix} \frac{e_{IC} g_{IC} C^0 I_{X_2}(E_0)}{g_{IC} + i_0} \\ a_{IR} I_{X_2}(E_0) \end{bmatrix},$$

with $I_{X_2}(E_0) = \frac{\partial I_L}{\partial X_2}(E_0)$. By substituting the parameter estimates in Table 3.5, we found $M = 1.9 \cdot 10^{-5} > 0$.

The stability of the *no-tumor* steady state can be affected by immunotherapy administrations. Even though, in absence of tumor, studying the effect of a therapy might seem useless, this suggests which conditions make the steady state attractive in realistic pathological scenarios.

Considering the continuous vaccine therapy, the value of C^0 considerably increases because the infused dendritic cells activate CTLs. For instance, with an infusion rate of $v = 0.0275\ 10^9$ cells/day, $D_v^0 = (s_D + v)/\mu_D = 0.2454\ 10^9$ cells and, consequently, $s_C = e_C \frac{D_v^0}{g_C + D_v^0} = 7.6\ 10^{-3}$ cells/day, which determines an increasing of the critical value r_{BP}^*.

In the case of anti-CTLA4 therapy, we added an extra term to the equation, changing the jacobian $J(E_0)$, so that $\lambda_3 = r_2 - \frac{e_X C^0}{g_X} - k_P I_P^* C^0$ and the threshold becomes: $r_{BP}^* = \frac{e_X C^0}{g_X} + k_P\ I_P^*\ C^0$.

These results show a promising increase in the region of stability of E_0, for both vaccine and anti-CTLA4 therapies.

3.5.2 Positive equilibrium point

By looking at the numerical simulations we observed a positive equilibrium point. The tumor, indeed, for large times tends to a saturation level represented by the tumor carrying capacity K. The existence of this positive equilibrium point is due to the presence of the transcritical bifurcation for $r_2 = r_{BP}^*$, proved before. Indeed, when this bifurcation occurs, a positive equilibrium branch runs into a negative one, i.e. an eigenvalue of the Jacobian matrix crosses the zero with non-zero derivative. In the following we refer to the critical value r_{BP}^* as Branching Point (BP). Numerically we found the equilibrium:

$$E_1 \ = \ (X_2^1, \quad C^1, \quad R^1) \ = \ (107 \cdot 10^9, \quad 2.5 \cdot 10^4, \quad 2.6 \cdot 10^9).$$

Studying the stability of this positive equilibrium point by analytical methods is complicated, thus we observed its qualitative behavior by using MatCont [77]. As shown in Figure 3.9, without administering any immunotherapy, the positive equilibrium E_1 is stable with a number of cancer cells close to K (107 billion of cells), until the tumor proliferation rate reaches very low values.

When r_2 reaches the critical value r^*_{LP}, corresponding to a Limit Point (LP), the branch of positive equilibria turns backwards and becomes unstable. In other words, for $r_2 \in [r^*_{LP}, r^*_{BP}]$, both the *high-tumor* (blue line) and *no-tumor* equilibria are stable, and there exists an unstable *low-tumor* equilibrium (green line). Solutions are attracted to the *high-tumor* or the *no-tumor* dependently of the initial conditions. The *high-tumor* equilibrium is globally asymptotically stable for $r_2 > r^*_{BP}$. We observe that the order of magnitude of our estimated r_2 is 10^{-3} (Table 3.5), while the one of the critical values r^*_{LP} and r^*_{BP} is 10^{-6}. For this reason, we can suppose that, for all reasonable patient-specific tumor proliferation rates, this *high-tumor* equilibrium remains stable for each tumor initial condition different from zero, when immunotherapies are not considered.

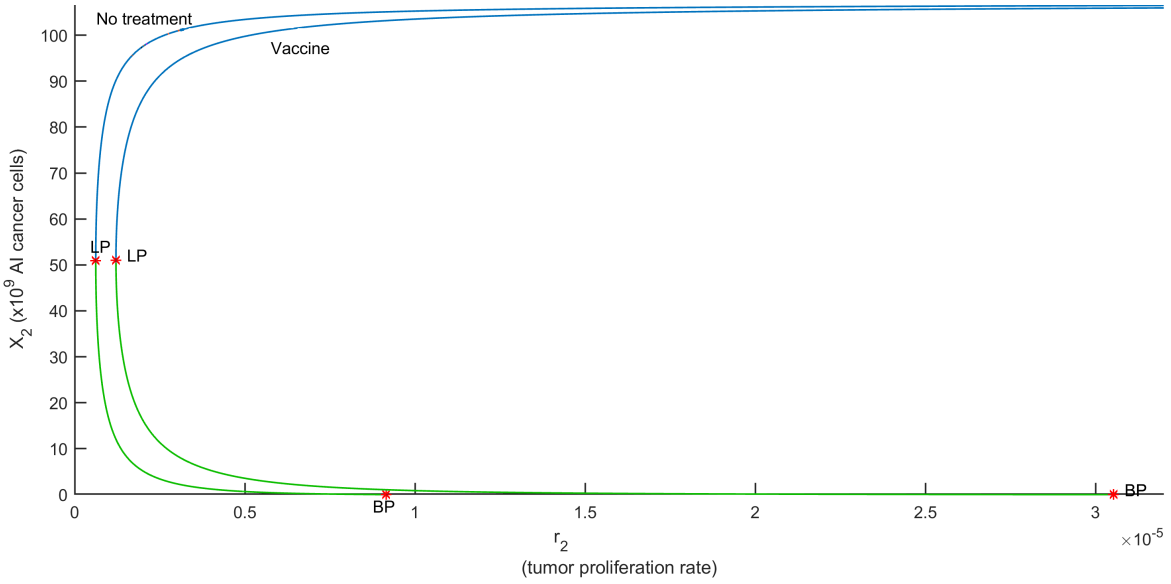

Figure 3.9: Positive equilibrium point of the human PCa model - vaccine versus untreated. Stability of the equilibrium E_1 when the tumor proliferation rate r_2 changes. The chart shows the equilibrium curve when no immunotherapies are administered (no treatment case) and under continuous vaccine with a dose of 0.0275 $10^9 cells/day$. The curves split into two branches: the *high-tumor* (blue line) and *low-tumor* (green line).

When the vaccine is administered, with a constant injection of $v = 0.0275\ 10^9$ cells/day, the branch of positive equilibrium discussed before moves to the right (see Figure 3.9). Although the BP in the vaccine case is much greater than the BP found without treatments, the LP is close to

the previous LP value, so the *high-tumor* equilibrium ceases to exist only for very small values of the proliferation rate. This property, combined with the shape of the curve, suggests that the basin of attraction of the *no-tumor* equilibrium point is small also in the vaccine case. This hypothesis has been confirmed by the Figures 3.16a and 3.16b, which highlight that, considering r_2 close to r^*_{BP}, for $X_2(0) > 10^9$ *cells*, the system converges to the *high-tumor* steady state. This result is very slightly affected by the vaccine dose. Indeed, also by increasing the infusion rate to 15-times stronger than the dosage considered, the curve slightly moves to the right, but both the critical values r^*_{LP} and r^*_{BP} maintain the same order of magnitude (see the Figure 3.13).

Administering the anti-CTLA4 therapy, the qualitative behavior of the branch of positive equilibria considerably changes as shown in Figure 3.10 (note the different scale of the x-axis in Fig. 3.10, compared to Fig. 3.9).

In this figure, the charts corresponding to a constant dosage of *ipilimumab* are compared to the no-treatment case. The effect of the anti-CTLA4 treatment on E_1 stability is evident: the equilibrium curve consistently moves to the right, reaching realistic critical values for r^*_{LP}. Indeed, the estimated value for r_2 $(6 \cdot 10^{-3})$ is lower than r^*_{BP}, suggesting that tumor eradication may be possible with this treatment. However, the values of the *low-tumor* branch for $r_2 \in [r^*_{LP}, r^*_{BP}]$ induce to suspect that the basin of attraction of the *no-tumor* steady-state is small. This has been confirmed by our simulations in Figure 3.17, showing that the *high-tumor* steady-state is attractive for low tumor initial conditions, for all the tumor proliferation rates in that range. This property seems to contradict the simulations in Figure 3.14, which show a tumor control with a constant *ipilimumab* infusion of 0.73 mg/day.

In order to investigate the conflicting behaviors, we reproduced two different administration protocols. We simulated the injection of 0.73 mg/day of *ipilimumab* administered with the androgen deprivation therapy (scenario 1 in Figure 3.11) and after 3 years of androgen deprivation therapy (scenario 2 in Figure 3.11). This *in silico* result highlights a different system behavior by changing the *ipilimumab* administration time. The scenario 2 confirms that, if the AIPC proliferates, the *ipilimumab* coupled with the androgen deprivation cannot control the tumor growth even if the value of X_2 at the start of the therapy is low. On the contrary, if we administer

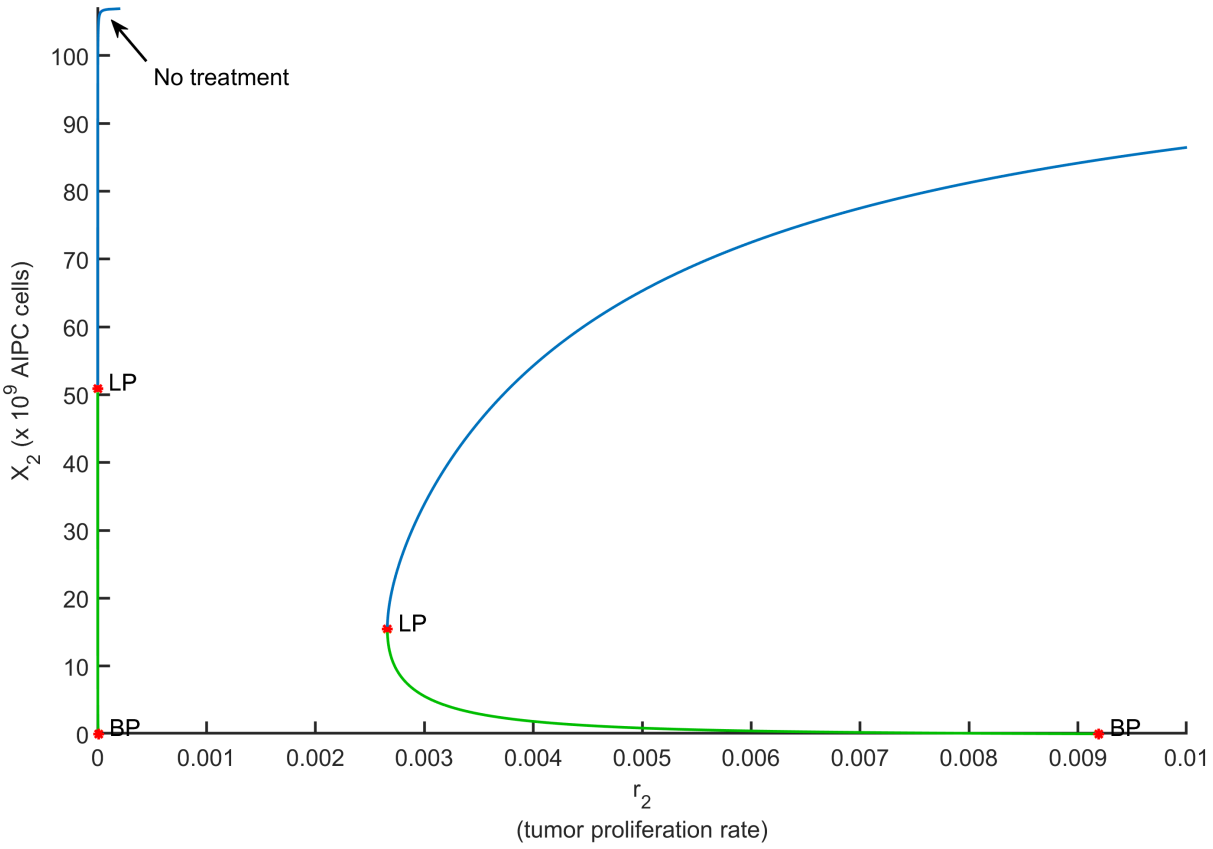

Figure 3.10: Positive equilibrium point of the humn PCa model - anti-CTLA4 therapy versus untreated. Stability of the equilibrium E_1 when the tumor proliferation rate r_2 changes. The chart shows the equilibria curve in case of anti-CTLA4 administered with constant infusion of $d_P = 0.73\ mg/day$, compared to the curve obtained without immunotherapies (no treatment case). The curves split into two branches: the *high-tumor* (blue line) and *low-tumor* (green line).

the two therapies together, the growth of AIPC cells can be restrained and the system reaches the *no-tumor* steady state.

3.6 Synergy between immunotherapies and hints for future works

In this section we introduce some preliminary results which are a first step for future extensions of the work presented in this chapter. The treatments included in our model can involve adverse

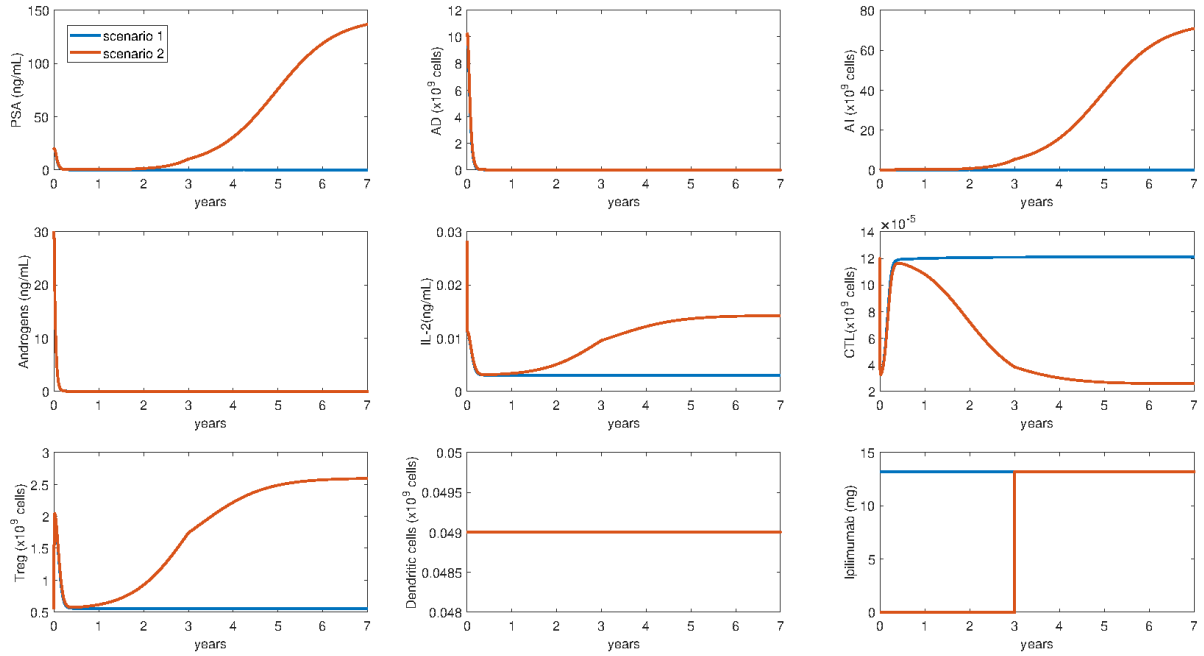

Figure 3.11: Human PCa model dynamics under anti-CTLA4 infusion - different scenarios. Dynamics of the system variables and PSA level when androgen deprivation therapy and continuous infusion of 0.73 mg/day of anti-CTLA4 are administered with two different protocols. The scenario 1 corresponds to the androgen deprivation and anti-CTLA4 combination therapy, while in the scenario 2 the anti-CTLA4 is administered 3 years after the androgen deprivation therapy.

events, which impact on the predicted efficacies of the therapies. Thus, future extensions of this work could consider the toxicity of the drugs. Moreover, since the model includes two different immunotherapies, they could be combined to evaluate the predicted effect of this drug combination. To this purpose, evaluating the synergy between these treatments represents a crucial starting point. Therefore, we estimated the synergy reproducing the procedure exposed by Lai *et al.* [32], which takes into account the drug toxicities. They considered two therapies, A and B, and compared the predicted tumor reduction of the combined therapy $A+B$ at standard doses γ_A and γ_B, with the one obtained with the single therapies administered with doses of $\gamma_A(1+\theta_A)$ and $\gamma_B(1+\theta_B)$. The parameters θ_A and θ_B are correlated with drug toxicities. Their values have been arbitrary chosen by the authors in $[0,1]$, where 1 represents no relevant toxicities and 0 corresponds to an irreversible adverse condition. Therefore, the synergy of the drugs A

and B has been defined as

$$\sigma(A,B) = \frac{E(\gamma_A,\gamma_B)}{\max\{E(\gamma_A\ (1+\theta_A),0),\ E(0,\gamma_B(1+\theta_B))\}} - 1, \tag{3.23}$$

where $E(x,y)$ represents the efficacy of a therapy with two treatments administered with doses x and y. If the efficacy of the combined therapy is greater than the efficacies of the single-drug administrations, $\sigma(\gamma_A,\gamma_B) > 0$ and the two drugs A and B are predicted to be synergistic. Conversely, if $\sigma(\gamma_A,\gamma_B) < 0$ the two drugs are antagonistic.

Following the approach introduced in [32], we focused on the (LS) system and we evaluated the synergy between vaccine (V) and anti-CTLA4 (AC) therapies for castrated patients developing the AIPC. For choosing realistic values of θ_V and θ_{AC}, we referred to experimental data. It has been demonstrated that, in castration-resistant prostate cancer patients, the dendritic cell vaccine *sipuleucel-T* exhibits Adverse Events (AEs) [136; 137]. The most of these side effects have been classified as grade 1 and 2 (68%). However, among the patients subjected of *sipuleucel-T* infusion, about the 31% of them presents severe AEs (grade 3, 4 or 5). All these side effects can be resolved within 1 or 2 days [137].

On the other hand, patients with metastatic melanoma treated with *ipilimumab* mainly show from mild to moderate AEs (grade 1 and 2) [138], but AEs of grade 3 or 4 have been shown in $20\%-45.8\%$ of the patients [139; 140]. The only available information regarding the AE resolution time refers to the Immune-Related Adverse Events (IRAEs), which represent the most common side effects, since they are observed in approximately the 60% of the treated patients [139; 140]. The average resolution time for IRAEs of grade ≥ 3 is 5.15 weeks [139; 140], while, for moderate IRAEs (grade 2) is approximatively 5.45 weeks [139–142] (for further details see Table 3.3). All the toxicities-related information are reported in Table 3.4, with the corresponding references.

These experimental results suggest that the toxicity of *ipilimumab* is higher than the one of the *sipuleucel-T* vaccine, which, according to the definition of the coefficient θ introduced in [32],

References	**Resolution time of IRAEs grade 2 (weeks)**	**Resolution time of IRAES grade $\geq$ 3 (weeks)**
[140]	4.9	4.9
[139]	6	8
[141]	-	3.7
[142]	-	4
Average	5.45	5.15

Table 3.3: Resolution times of the immune-related adverse events due to *ipilimumab* administration - experimental data. Resolution times of IRAEs in different clinical experiments.

References	% **AE**	% **AE grade** $\geq$ 3 w.r.t. total patients	% **AE grade** 1 **and** 2 w.r.t. total patients
[140]	96.9	44.4	52.5
[139]	80	22.9	61.68
Average	88.5	31	57

Table 3.4: Percentage of adverse events due to *ipilimumab* administration - experimental data. Percentages of patients showing Adverse Events (AEs) and Immune-Related Adverse Events (IRAE) in different clinical experiments.

means $\theta_{AC} < \theta_V$. Therefore, the values of θ_V and θ_{AC} have been chosen as:

$$\theta_x = 1 - T_x, \tag{3.24}$$

where T_x expresses the toxicity of the drug x and it has been defined according to the experimental data as:

$$T_x = \left(1 - \frac{1}{t_M^x}\right) P_M^x + \left(1 - \frac{1}{t_S^x}\right) P_S^x. \tag{3.25}$$

The variables t_M^x and P_M^x represent, respectively, the resolution time and the percentage of the patients who exhibit moderate AEs (grade 1 and 2) after the administration of the drug x. Conversely, t_S^x and P_S^x are the resolution time and the percentage of the patients who exhibit severe AEs (grade 3, 4 and 5), after the administration of the drug x. This definition of toxicity is a sort of weighted average of the percentages of patients showing moderate and severe AEs, in which the weights are represented by a function of the resolution times. We supposed that the optimal resolution time is 1 day and, for higher values of t^x, the contribution of the corresponding percentage P^x grows, increasing the value of the toxicity of x.

By considering the average experimental data of the *sipuleucel-T* and *ipilimumab* drugs reported before, and coupling Eq.s (3.24) and (3.25), we obtained $\theta_V = 0.67$ and $\theta_{AC} = 0.15$. By numerical simulation, we estimated the value of $\sigma(V, AC) = 0.2$, confirming the synergistic property of this combination therapy.

3.7 Materials and methods

Computational environment

The model has been implemented as a set of Matlab functions [116], which have been simulated by the state-of-the-art *ode15s* integrator. For the model calibration, we used the function *fmincon* within the Matlab optimization toolbox. To guarantee a complete exploration of the parameter space, the *fmincon* algorithm has been execute within a multi-start strategy by means of the *multistart* Matlab function.

Structural Identifiability analysis

A structural identifiability analysis has been performed by means of the Matlab toolbox GenSSI [84]. The software requires: (i) a list of all the model variables and their relations inside the mathematical model; (ii) a list of all the model parameters, by also specifying the ones that have

to be estimated; (iii) the model initial conditions for running the simulations; and (iv) a list of the experimentally observed quantities, which can be model variables or a function of these. The execution of the GENSSI algorithm confirmed the structural global identifiability of the model parameters.

Local Sensitivity Analysis

A LSA has been performed on tumor size. We considered the total amount of tumor as $X = X_1 + X_2$ and we evaluated the tumor LSA value of a model parameter p by using the logarithmic LSA introduced in the Chapter 1. Starting from the Eq. (1.8), we approximated $\frac{\partial X(t,p)}{\partial p}$ by the central finite difference, obtaining:

$$LSA(p) = \frac{X(t_f, p + \Delta p) - X(t_f, p - \Delta p)}{2 \cdot \Delta \cdot X(t_f, p)},$$

where t_f is the last simulated time point. The results obtained by fixing $\Delta = 1\%$ and two different simulation times ($t_f = 4$ months and $t_f = 6$) are shown in the Appendix B.

3.8 Additional figures

Figure 3.12 provides the system dynamics when the intermittent anti-CTLA4 therapy is administered for long time. The system shows two different dynamics for anti-CTLA4 therapy administered for 22 years and for 21 years. The charts show that, after 22 years of therapy, the *no-tumor* steady state becomes attractive, determining the eradication of the tumor, while, administering this therapy for 21 years, the system converges to the *high-tumor* steady state.

Figure 3.13 shows the qualitative behavior of the *high-tumor* steady state in case of vaccine. The chart provides two curves, regarding the effect of continuous vaccine in low dose ($2.75 \cdot 10^7$ $cells/day$) and high dose ($4.13 \cdot 10^8$ $cells/day$), in order to prove that the vaccine dose does not affect the qualitative behavior of the system.

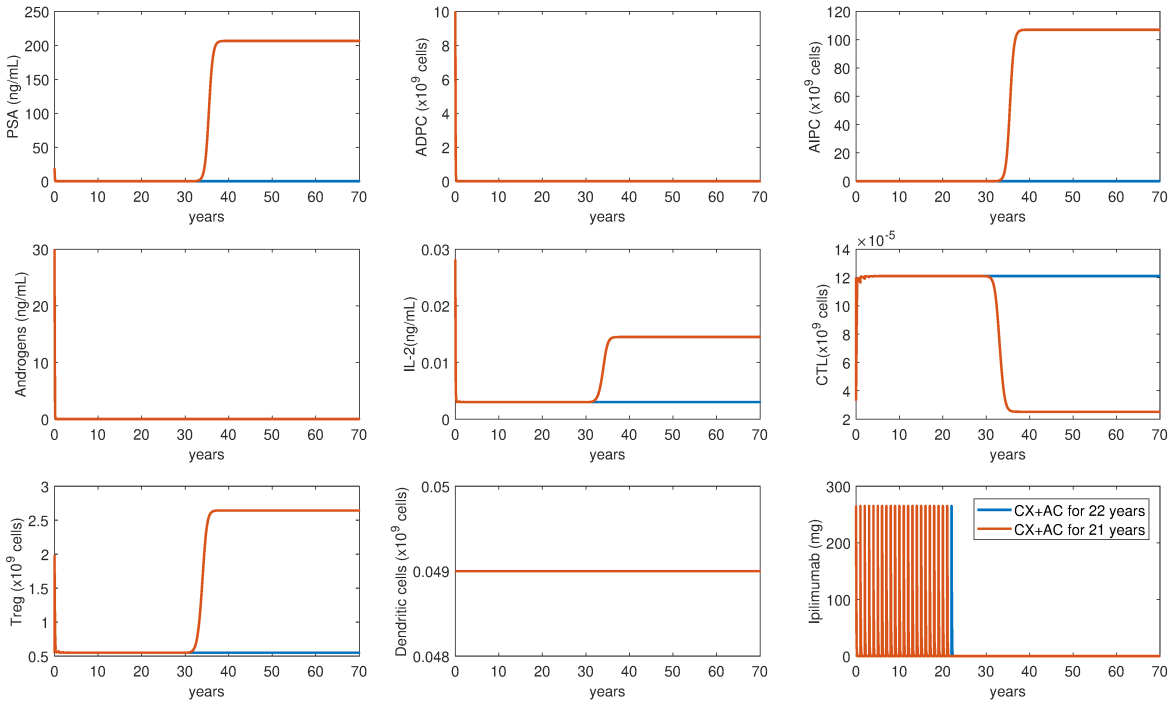

Figure 3.12: Human PCa model dynamics under androgen deprivation intermittent anti-CTLA4 infusion - long-term therapy. Dynamics of the system variables and PSA level when castrated patients are subject to intermittent infusion of 256.5 mg per year of the drug *ipilimumab* for 22 years (blue line) and for 21 years (orange line).

Figure 3.14 shows the dynamics in case of androgen deprivation combined with anti-CTLA4 therapy, comparing the intermittent and the continuous administration protocols of the drug *ipilimumab*. The figure highlights that the two different schedules do not affect the system dynamics for long period.

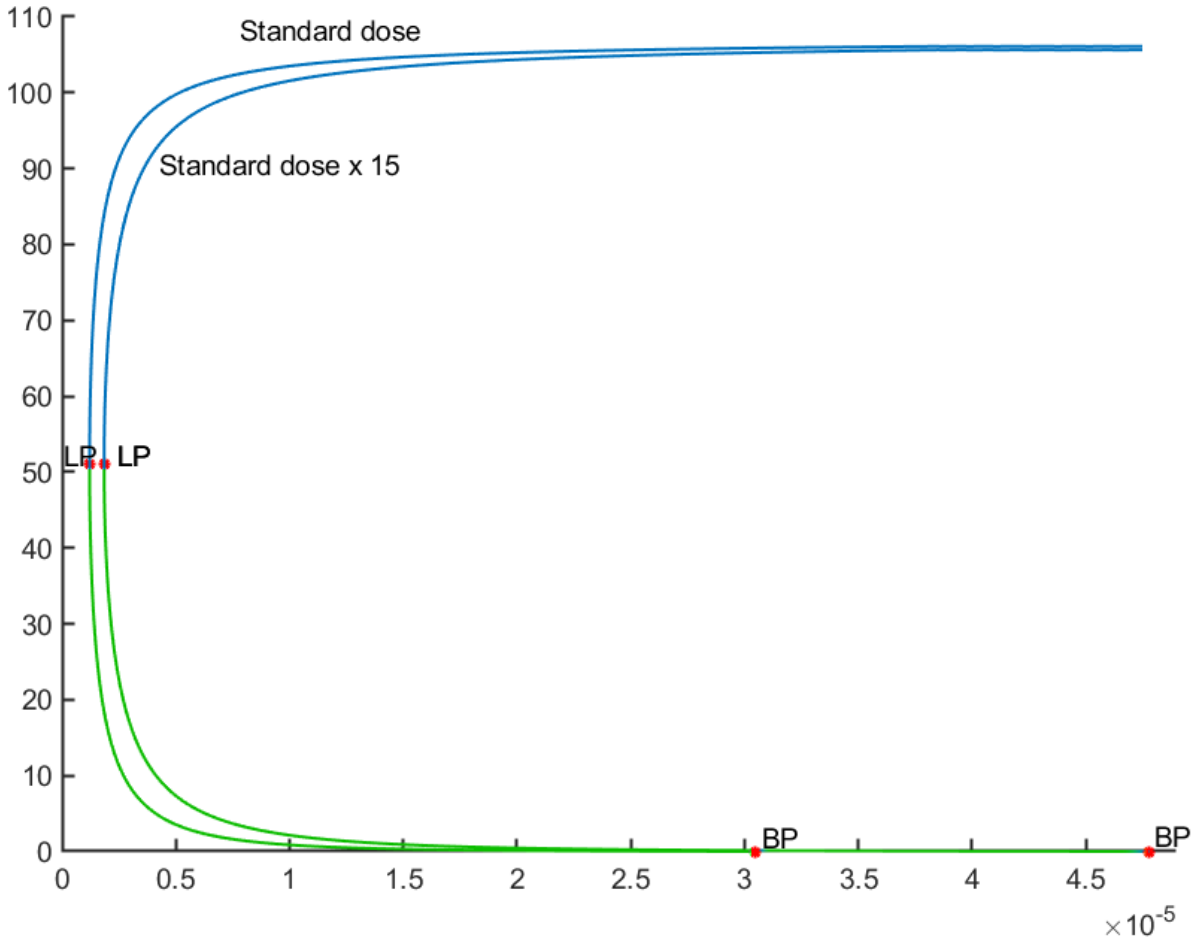

Figure 3.13: Positive equilibrium point of human PCa model - high versus low doses of vaccine. Stability of the equilibrium E_1 when the tumor proliferation rate r_2 changes. The chart shows the equilibria curves when the vaccine is administered in low ($2.75 \cdot 10^7 cells/day$) and high doses ($15 \cdot 2.75 \cdot 10^7 cells/day$). The curves split into two branches: the *high-tumor* (blue line) and *low-tumor* (green line).

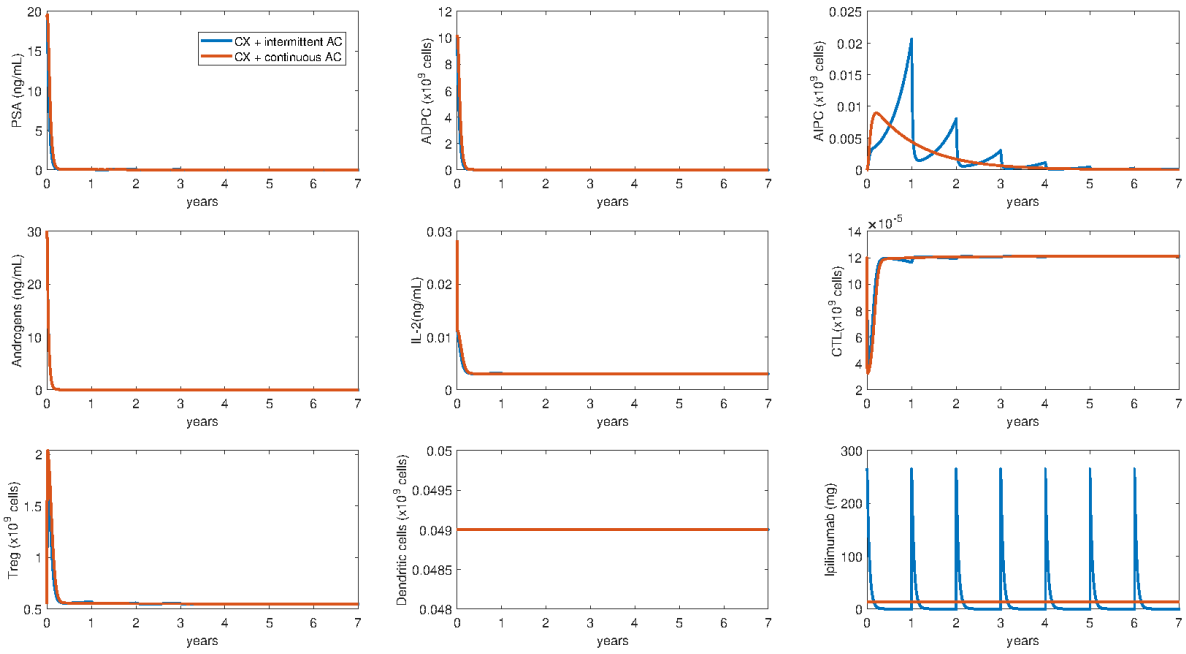

Figure 3.14: Comparison of human PCa model dynamics under androgen deprivation therapy combined to different administration protocols of anti-CTLA4 therapy. Dynamics of the system variables and PSA level when androgen deprivation therapy is combined with anti-CTLA4, which is administered with different protocols. The drug *ipilimumab* is injected every year with a dose of 265.5 mg (blue line), or with a constant infusion of 0.73 mg/day (orange line).

3.9 Basin of attractions

To further investigate the basin of attractions of the two steady states E_0 and E_1, we evaluate where the system converges by changing the initial point. We consider three main scenarios regarding different treatment conditions, where the critical interval of r_2 changes according to the different values of r^*_{BP} and r^*_{LP}:

- Scenario 1, without immunotherapies, where $r_2 \in [6.7 \cdot 10^{-7},\ 9.1 \cdot 10^{-6}]$.
- Scenario 2, with dendritic cell vaccine, where $r_2 \in [1.2 \cdot 10^{-6},\ 3 \cdot 10^{-5}]$.
- Scenario 3, with anti-CTLA4 therapy, where $r_2 \in [0.0027\ ,\ 0.0092]$.

We plot a two-dimensional grid describing the initial conditions of X_2 and R. We define the mesh on X_2R-plane and, by starting from the corresponding initial condition, we plot a red point if the system converges to the *hihg-tumor* steady state, and a blue point if the system converges to the *no-tumor* steady state. For each simulation we fix the value of $C(0)$ in $[2.5 \cdot 10^4, 1.3 \cdot 10^5]$ and the proliferation rate r_2.

The first row in the Figures 3.15, 3.16, and 3.17 represents the results for tumor proliferation rates close to the corresponding r^*_{BP}, by fixing $C(0) = C_{max} = 1.3 \cdot 10^5$ *cells* (first column) and $C(0) = C_{min} = 2.5 \cdot 10^4$ *cells* (second column). The second row, instead, refers to tumor proliferation rates close to the corresponding r^*_{LP}, by fixing $C(0) = C_{max} = 1.3 \cdot 10^5$ *cells* (first column) and $C(0) = C_{min} = 2.5 \cdot 10^4$ *cells* (second column). Figure 3.17 includes additional charts. For a detailed description see the figure captions.

In all the scenarios considered, the results show that the stability of the equilibrium points seems depend only on the initial condition of X_2. Moreover, we observe that the basin of attraction of E_0 is small for every realistic tumor proliferation rate, i.e. rates with order of magnitude of 10^{-4} or 10^{-3}.

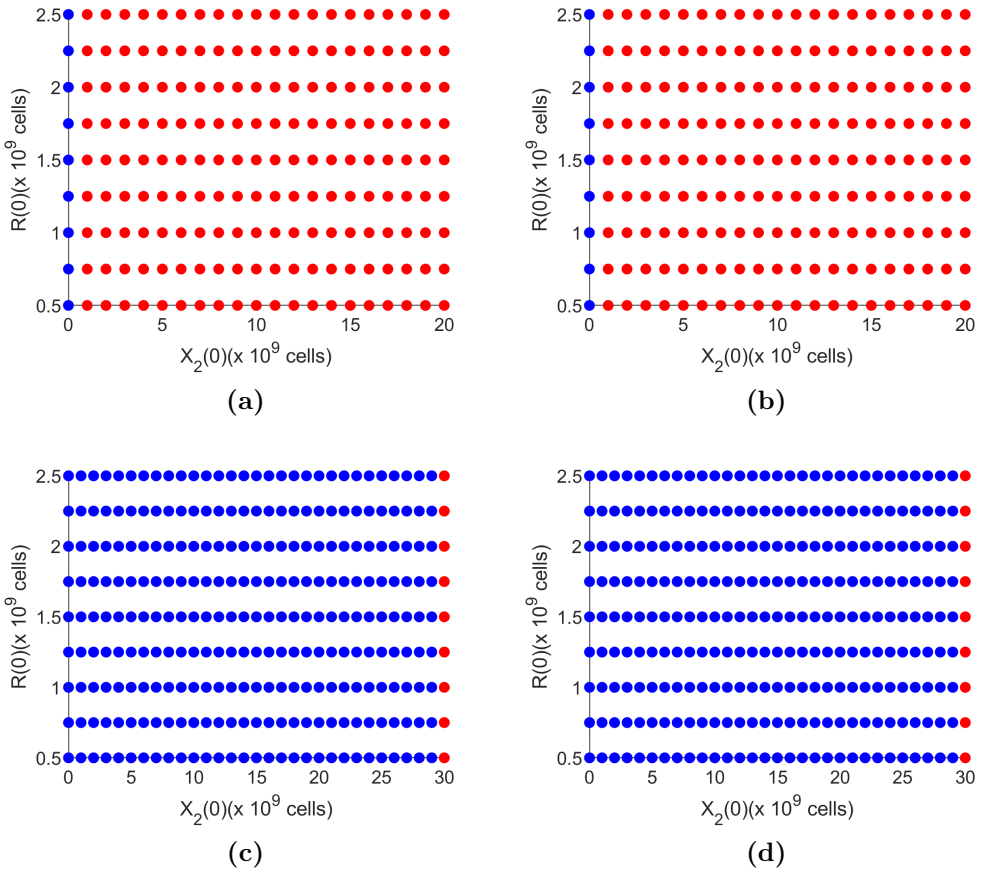

Figure 3.15: Basin of attractions of the human PCa model steady states - scenario 1. Basin of attraction of the steady states E_1 and E_0. By varying the initial condition of AIPC cells (on the x-axis) and of Treg cells (on the y-axis), the charts depict a blue point if the dynamics converge to E_0, while a red point if converge to E_1. For each simulation, the initial value of the CTLs is fixed in $[2.5 \cdot 10^4\ ,\ 1.3 \cdot 10^5]$ and the proliferation rate r_2 in $[6.7 \cdot 10^{-7},\ 9.1 \cdot 10^{-6}]$. (a) Simulation with high value of CTLs, $C(0) = 1.3 \cdot 10^5$ cells, and high tumor proliferation rate $r_2 = 8.1 \cdot 10^{-6}$. (b) Simulation with low value of CTLs, $C(0) = 2.5 \cdot 10^4$ cells, and high tumor proliferation rate $r_2 = 8.1 \cdot 10^{-6}$. (c) Simulation with high value of CTLs, $C(0) = 1.3 \cdot 10^5$ cells, and low tumor proliferation rate $r_2 = 7.2 \cdot 10^{-7}$. (d) Simulation with low value of CTLs, $C(0) = 2.5 \cdot 10^4$ cells, and low tumor proliferation rate $r_2 = 7.2 \cdot 10^{-7}$.

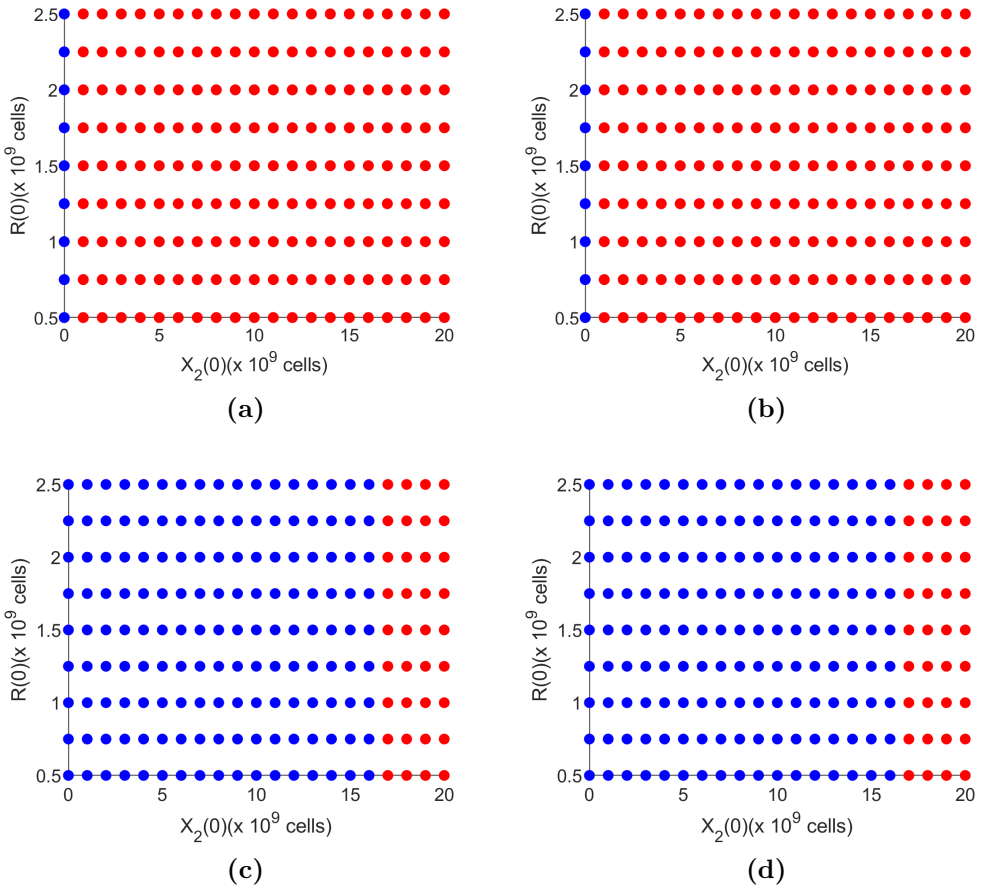

Figure 3.16: Basin of attractions of the human PCa model steady states - scenario 2. Basin of attraction of the steady states E_1 and E_0. By varying the initial condition of AIPC cells (on the x-axis) and of Treg cells (on the y-axis), the charts depict a blue point if the dynamics converge to E_0, while a red point if converge to E_1. For each simulation, the initial value of the CTLs is fixed in $[2.5 \cdot 10^4\ ,\ 1.3 \cdot 10^5]$ and the proliferation rate r_2 in $[1.2 \cdot 10^{-6},\ 3 \cdot 10^{-5}]$. (a) Simulation with high value of CTLs, $C(0) = 1.3 \cdot 10^5$ cells, and high tumor proliferation rate $r_2 = 2 \cdot 10^{-5}$. (b) Simulation with low value of CTLs, $C(0) = 2.5 \cdot 10^4$ cells, and high tumor proliferation rate $r_2 = 2 \cdot 10^{-5}$. (c) Simulation with high value of CTLs, $C(0) = 1.3 \cdot 10^5$ cells, and low tumor proliferation rate $r_2 = 2.2 \cdot 10^{-6}$. (d) Simulation with low value of CTLs, $C(0) = 2.5 \cdot 10^4$ cells, and low tumor proliferation rate $r_2 = 2.2 \cdot 10^{-6}$.

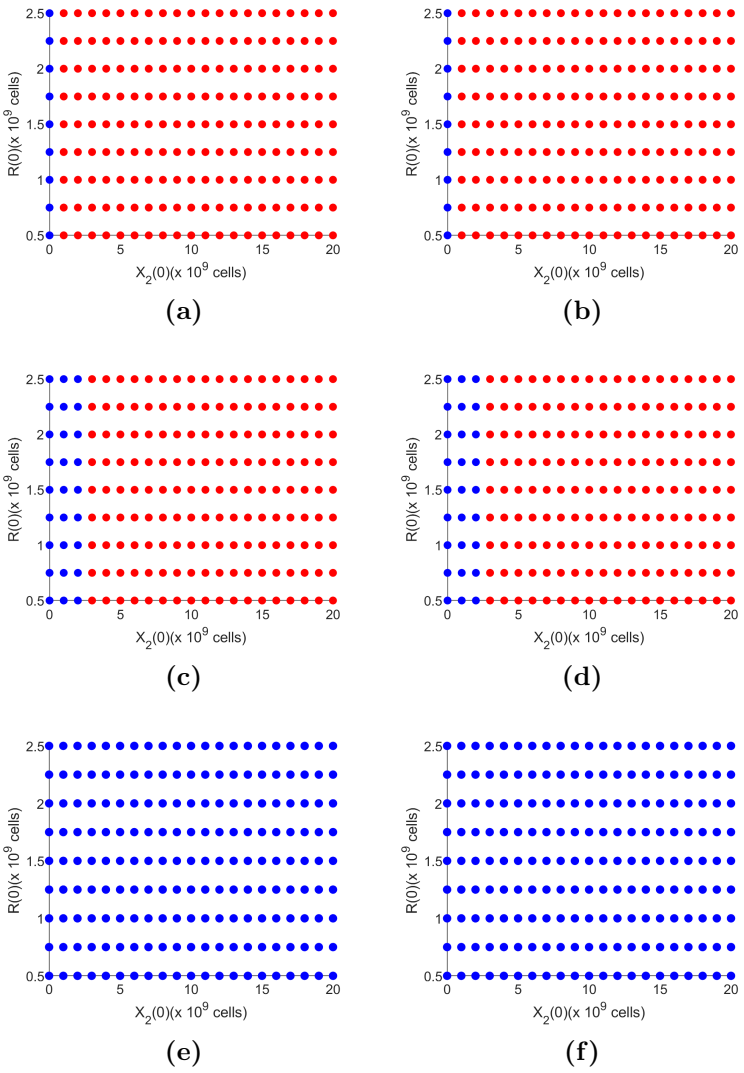

Figure 3.17: Basin of attractions of the human PCa model steady states - scenario 3. Basin of attraction of the steady states E_1 and E_0. By varying the initial condition of AIPC cells (x-axis) and of Treg cells (y-axis), the charts depict a blue point if the dynamics converge to E_0, while a red point if converge to E_1. For each simulation, the initial value of the CTLs is fixed in $[2.5 \cdot 10^4\ ,\ 1.3 \cdot 10^5]$ and the proliferation rate r_2 in $[0.0027\ ,\ 0.0092]$. (a) Simulation with high value of CTLs, $C(0) = 1.3 \cdot 10^5$ cells and high tumor proliferation rate $r_2 = 0.0082$. (b) Simulation with low value of CTLs, $C(0) = 1.3 \cdot 10^5$ cells and high tumor proliferation rate $r_2 = 0.0082$. (c) Simulation with high value of CTLs, $C(0) = 1.3 \cdot 10^5$ cells and low tumor proliferation rate $r_2 = 0.0037$. (d) Simulation with low value of CTLs, $C(0) = 1.3 \cdot 10^5$ cells and low tumor proliferation rate $r_2 = 0.0037$. (e) Simulation with high value of CTLs, $C(0) = 1.3 \cdot 10^5$ cells and tumor proliferation rate as the r^*_{BP} of vaccine case, $r_2 = 9 \cdot 10^{-6}$. (f) Simulation with low value of CTLs, $C(0) = 1.3 \cdot 10^5$ cells and tumor proliferation rate as the r^*_{BP} of vaccine case, $r_2 = 9 \cdot 10^{-6}$.

3.10 Table of parameters

Equation	Parameter	Description	Value	References
PCa Eqs. (3.1) and (3.2)	r_1	Proliferation rate of androgen dependent prostate cancer cells (ADPC)	5.67 10^{-4} day^{-1}	[24]
	K	Tumor carrying capacity	107 $10^9 cells$	3.2
	μ_1	Death rate of ADPC	0.064 day^{-1}	[24]
	m_1	Maximum mutation rate of ADPC into AIPC	0.5 10^{-4} day^{-1}	[24]
	e_{CX}	Maximal killing rate of tumor by CTL in untreated case	$0-1$ day^{-1}	[24]
	g_{CX}	CTL saturation level for tumor cells inhibition	10 10^9 $cells$	[24]
	k_{I_P}	Maximal killing rate of tumor by CTL due to the drug *ipilimumab*	5.44 10^{-9} $1/day$ $(mg\ cells)^{-1}$	3.2
	a_0	Baseline serum levels of androgen	30 ng/ml	[24]

PCa Eqs. (3.1) and (3.2)	r_2	Proliferation rate of androgen independent prostate cancer cells (AIPC)	0.006 day^{-1}	[24]
CTL Eq. (3.3)	e_C	Maximal activation rate of CTL by dendritic cells	0.02 10^9 $cells/day$	[24]
	g_C	Dendritic cells saturation level for T cell clonal expansion	0.4 10^9 $cells$	[24]
	e_{IC}	Maximal activation rate of CTL by IL-2	0.1245 day^{-1}	[24]
	g_{IC}	IL-2 saturation level for T cell clonal expansion	1000 ng/ml	[24]
	μ_C	Death rate of CTL	0.03 day^{-1}	[24]
	k_R	Inactivation rate of CTL by Tregs	32.81 10^{-9} $(day \cdot cells)^{-1}$	3.2
Treg Eq. (3.4)	a_R	Activation rate of Treg by mature dendritic cells	0.072 day^{-1}	[119]
	μ_R	Death rate of Treg	0.72 day^{-1}	[119]
	a_{IR}	Activation rate of Treg by IL-2	131.26 10^9 (ml/ng)(cells/day)	3.2

Dendritic cell Eq. (3.5)	s_D	Source of dendritic cells	$0.00686\ 10^9\ cells/day$	3.2
	v	Dendritic cells vaccine dose	$0.0275\ 10^9 cells/day$	[24]
	μ_D	Death rate of dendritic cells	$0.14\ day^{-1}$	[24]
IL-2 Eq. (3.6)	e_I	Maximal activation rate of IL-2 by CTL and tumor	$5\ 10^{-6}\ (ng/ml)(cells \cdot day)^{-1}$	[24]
	g_I	Tumor cells saturation level for CTL stimulation of IL-2	$10\ 10^9 cells$	[24]
	μ_I	Death rate of IL-2	$10\ day^{-1}$	[24]
	i_0	Baseline level of IL-2	$0.00299\ ng/ml$	3.2
Eq. (3.7)	γ_A	androgen turnover rate	$0.08\ day^{-1}$	[24]
Eq. (3.8)	λ_P	*Ipilimumab* death rate	$0.055\ day^{-1}$	3.2
Eq. (3.9)	c_{PSA}	Rate of PSA secreted by tumor cells	$1.93\ \ 10^{-9}\ (ng/ml)\ (1/day\ cells)$	3.2

Table 3.5: Table of human mathematical model parameters. The table provide the parameter estimates, with the corresponding descriptions, values and estimation procedure.

Chapter 4

Conclusion

This dissertation exposes the two mathematical models on PCa developed during my PhD period. The two works present substantial differences in both the model formulation and calibration, and the system analysis. Indeed, the first model, describing the evolution of PCa in mice, includes 19 ODEs and, compared with the existing PCa models [23; 24; 119; 121; 143–145], it comprehends more mechanistic details about the tumor microenvironment. This accurate description allowed us to test different types of immunotherapy, obtaining a comprehensive view of the treatment effects, which is the aim of this work. The second model, comprehending 8 ODEs, describes the dynamics of human PCa. This model has been reduced to a three-dimensional model and it has been studied by the steady-state analysis, comparing the efficacy of the two immunotherapies considered.

Chapter 2 is dedicated to the murine PCa mathematical model, which has been developed by starting from a preexistent model by Peng *et al.* [23]. In addition to the tumor-immune interactions described in the original model, we implemented the immuno-suppression exerted by MDSCs, immune cells that have been recently demonstrated to be important contributors to PCa progression [92; 93; 146–149]. Targeting MDSCs is emerging as an attractive therapeutic option to improve the response rate to immunotherapy and patient survival in several cancers [150]. Interestingly, a recent phase II clinical trial in melanoma (NCT02403778) showed that the

addition of an anti-MDSC agent to ICB therapy seems to be safe and it increases the number of activated T cells [151]. However, additional clinical studies are needed to evaluate the effectiveness of this approach. Furthermore, we added NK cells, components of the innate immune branch exerting a cytotoxic action without the need of prior antigen exposure [152; 153]. The potential of NK cells in cancer immunotherapy has been pointed out by numerous preclinical studies that showed several attractive features of these cells [154]. Above all, NK cells display an overall safe profile, given by their limited *in vivo* persistence, the lack of clonal expansion, and the absence of the immune rejection associated with allogeneic transplantation [155]. Despite these positive characteristics, the use of NK cell-based immunotherapy in clinical settings is still at the beginning and the availability of a mathematical model describing NK cell action could support the design of new studies. In addition, we included the ICB treatment as an increment in the CTL tumor-killing capacity, according to the biological evidences indicating that immune-checkpoints limit T cell effector functions [96; 117; 156]. The ICB therapies have been proven promising for several types of solid tumors, so much so that, in recent years, the FDA approved ICB treatments for metastatic melanoma and renal carcinoma [60]. These successes lead to an increasing interest also in the context of prostate cancer[157], and a combination of two different ICB drugs is currently under phase II clinical trial for metastatic castration-resistant prostate cancer [158] (NCT02985957).

Our model offers the possibility of testing *in silico* a variety of combinatorial immunotherapies and identifying the most promising ones. In particular, in this study we evaluated the effect of combination immunotherapies in subjects developing AIPC after androgen deprivation therapy, considering both the impact on tumor size and the synergistic effects. Given the high number of immunotherapies currently available, it is not feasible to test all combinations in animal models and clinical setting. Our mathematical model offers a cost-effective approach to identify *in silico* the most promising combination therapies. This is particularly relevant for prostate cancer, a type of tumor that so far did not respond well to immunotherapy. The ICB therapy, for example, despite the promising results in the treatment of other solid tumors, has not yet been approved for prostate cancer. A possible explanation of the lack of satisfactory results could be due to a

strong immuno-suppressive tumor microenvironment [56; 159; 160].

Interestingly, our simulations indicate that anti-MDSC combined with ICB almost double the efficacy of ICB alone (44% vs 26% tumor reduction compared to untreated). When considering dual-drug therapies, our results showed ICB as the most effective immunotherapy in subjects under androgen deprivation therapy. Supporting these findings, a phase II clinical trial testing androgen deprivation therapy and ICB reported a reduction in PSA levels and tumor reduction in 25% of patients [161].

The mathematical model presented in Chapter 2 has been developed with the aim of building a tool to test *in silico* the efficacy of cancer immunotherapies. To bypass the paucity of public data from human studies, the model has been calibrated using data derived from prostate cancer mouse models and *in vitro* experiments. Given the high number of parameters, we performed a identifiability analysis by the Matlab toolbox GenSSI, which guaranteed a local parameter identifiability. In addition, to investigate the impact of data availability on model predictions, we performed a local and a global sensitivity analyses on the tumor size, which is the main variable discussed in the result section (see Sections 2.2, 2.5 and the Appendix A). As expected, both the analyses showed that the tumor dynamics resulted to be highly influenced only by the tumor proliferation and death rates, and by the effect of CTL and NK cells killing abilities. Moreover, when the ICB is administered, also the CTL killing capacity due to this drug is predicted to influence the tumor size. Therefore, the results obtained from the sensitivity analyses suggest that the model predicted tumor size is poorly affected by parameter uncertainty, except for the few parameters playing a crucial role in tumor dynamics.

The results of both identifiability and sensitivity analyses provide an indication of the reliability of model predictions, but additional efforts could be devoted to identify a new calibration targeted to human data. In this case, it would be fundamental to add a peripheral compartment to the model, because most of the human data derives from peripheral tissues, such as blood. In this context, our model represents an initial step toward the development of a QSP model including the pharmacokinetics and pharmacodynamics descriptions. Future extensions could also address the mechanism of action of the drugs. For example, we could better describe MDSC and

Treg regulations, considering the intracellular signaling of these cells to identify new targets of anti-MDSC and anti-Treg drugs. Moreover, we could include a more detailed description of the IL-2 production and Treg dynamics [108; 162] with a specific focus on the mechanisms that can be potential targets of prostate cancer therapies. The model capabilities could also be enhanced by including in the tumor equations a stochastic "mutation" term, which describes the evolution from ADPC into AIPC considering both the mutation randomness and the selective pressure due to androgen deprivation therapy. An additional aspect that could be taken into account is the toxicity of the treatments. For example, some immunotherapies, by enhancing T cell activity, can induce strong, life-threatening immune reactions [163]. In this perspective, the availability of data related to the treatment side-effects would be highly beneficial because it would allow extending the synergy analysis by including the toxicity effect [32] and thus better supporting clinical decision-making.

In **Chapter 3**, we present the human PCa mathematical model, developed from the one proposed by Rutter and Kuang [24]. The model includes the androgen deprivation therapy, as classical treatment for PCa patients, and other two immunotherapies, the approved dendritic cell vaccine *sipuleucel-T* and an anti-CTLA4, the *ipilimumab* drug, the ICB currently under phase II clinical trial (NCT02985957, NCT03061539). By observing the model simulations, the vaccine is predicted to increase the immune cells activation, but it does not enhance the effect of the immune system on tumor cells. Therefore, the AIPC proliferates and the system goes to an *high-tumor* steady state. Conversely, the treatment with *ipilimumab* shows an inhibitory effect on tumor cells, which, however, in single dose, is not enough to control the tumor growth. Nevertheless, the *in silico* results suggest that intermittent administrations of the drug *ipilimumab*, combined with the androgen deprivation therapy, may reduce the tumor volume, confirming the potential anti-tumor effect of this combination therapy against prostate cancer.

To examine in depth the effect of the immunotherapies on the AIPC, we set the androgen-deprivation as the mainstay treatment and we focused on those cases in which the tumor evolves in the androgen-independent form as consequence of the castration therapy. We reduced the system to (LS) and we studied how the qualitative behavior of (LS) changes, depending on

the variation of the tumor proliferation rate, when the immunotherapies are administered with constant infusion. These results showed that the vaccine slightly enhances the effect of the androgen deprivation therapy, but the basin of attraction of the *no-tumor* equilibrium remain small and, for every reasonable values of the tumor proliferation rate, the *high-tumor* steady state is attractive. When we considered the *ipilimumab* constant infusion, the system was able to reach the *no-tumor* equilibrium point for reasonable values of the tumor proliferation rate, thus we observed a situation with two equilibria, the *high-tumor* and *no-tumor*, both attractive. The convergence of the system to a tumor eradication or a tumor uncontrollable growth seems to depend on the schedule of the therapies, since the model shows different behaviors by changing time schedules. Indeed, the model predicts a tumor control when the anti-CTLA4 treatment is administered at the same time with the androgen deprivation therapy. Conversely, if we administer the drug *ipilimumab* after 3 years, this allows the AIPC to start the proliferation and the system converges to the *high-tumor* steady state. Interestingly, there are biological evidences that highlight the synergistic effect of the *ipilimimuab* coupled with androgen deprivation therapy [164; 165].

The model presented in Chapter 3, compared to the murine PCa model introduced in the Chapter 2, represents a step forward for the mathematical description of human prostate cancer and, therefore, an improvement in the direction of mathematical models supporting medical decisions. Indeed, since the model calibration has been performed with human data, the presented results can be discussed from a clinical point of view. However, it is important to notice that, despite our results suggest the combination of castration and anti-CTLA4 as the most promising therapy, the combined administration could be unnecessary, since the androgen deprivation therapy is effective in most of patients [53], who do not necessitate of other additional treatments. Our model, in fact, considers only those cases in which the tumor evolves to the AIPC form, since the mutation from ADPC into AIPC is described by a deterministic term. This term represents the selective pressure due to the androgen deprivation but it does not consider the randomness of the mutations. Therefore, rather than supporting a combined administration of anti-CTLA4 and androgen deprivation therapies, the model highlights the importance of frequent clinical controls

for castrated patients, to prevent the development of the AIPC cells. Moreover, it is important to highlight that the effect of the anti-CTLA4 therapy has been estimated by using the only available experimental data provided in Small *et al.* paper [117], regarding patients who received the major benefits from this treatment. For this reason, the *ipilimumab* effect could be overestimated and a new calibration with a more wide range of clinical data should be performed. The LSA on tumor confirmed that this variable is influenced by the parameter k_{I_P}, representing the tumor killing rate by CTLS due to the drug *ipilimumab*. In addition, the presented description of the tumor microenvironment is limited to few variables; further extensions will include other important immune cells, such as myeloid derived suppressor cells and natural killer cells, as potential targets for PCa therapies [93; 148; 152; 154].

As for the work presented in Chapter 2, also the human PCa model does not consider the side effects of the treatments. Future extensions will comprehend the toxicity of the drugs, since, especially for the *ipilimumab*, adverse events could be consistent and they can affect the outcomes of clinical experiments [166; 167]. Moreover, future model analysis will include the effect of the vaccine and anti-CTLA4 combination therapy, which is under phase I clinical trial [168]. This study observes that this combination therapy is synergistic and well tolerated, showing a significant increase in serum antibodies specific for the prostate tumor-associated antigen. From this perspective, at the end of the Chapter 3, we evaluated the synergy between the two immunotherapies, the *sipuleucel-T* vaccine and the *ipilimumab* anti-CTLA4, taking into account their toxicities, and our estimate confirmed the expected synergy between the two drugs. To compute the coefficient of synergy, we extrapolated information from experimental data and we defined the toxicity for a generic drug x. At this stage of work, this value does not depend on the drug doses. However, studies on metastatic melanoma patients observed that the toxicity of *ipilimumab* dependents of its dose [169; 170]. In the future, we will improve this definition of the toxicity, introducing a dose-dependent function.

Appendix A

Local and Global Sensitivity Analyses of mouse PCa model

This appendix includes the results of the local and global sensitivity analyses on tumor size.

The LSA value has been computed by the formula:

$$LSA(p) = \frac{X(t_f, p + 1\%p) - X(t_f, p - 1\%p)}{0.02 \cdot X(t_f, p)},$$

by fixing the simulation time $t_f = 49$ days.

To implement the GSA we sampled the parameter space by 1000 random parameter sets and, for each of these sets, a LSA has been performed by the formula:

$$LSA(p) = \int_0^{t_f} \frac{X(t, p + 1\%p) - X(t, p - 1\%p)}{0.02 \cdot X(t, p)}\, dt.$$

Therefore, for each parameter, we extrapolated the GSA as the median of the LSA values computed for the different parameter sets.

These results are discussed in Section 2.2. Figures A.1-A.11 shown the LSA and GSA values, which are sorted by the highest GSA absolute values.

Untreated case					
LSA	abs LSA	GSA	abs GSA	Parameter	Prmeter description
8.99	8.99	61.96	61.96	rp1	Proliferation rate of ADPC
-0.14	0.14	-4.26	4.26	kNT	Maximal killing rate of tumor by NK
0.34	0.34	3.23	3.23	krn	NK cytotoxic effect Treg-dependent inhibition
0.00	0.00	2.82	2.82	kxn	NK inactivation by tumor
0.05	0.05	2.73	2.73	kmn	NK cytotoxic effect MDSC-dependent inhibition
-0.08	0.08	-2.67	2.67	kcx	Maximal killing rate of tumor by CTL
-0.05	0.05	-2.57	2.57	mum	MDSC death rate
0.04	0.04	2.21	2.21	rhoM	source of MDSC
-0.10	0.10	-2.08	2.08	rhoN	Source of NK
-0.24	0.24	-1.81	1.81	mur	Treg death rate
-0.02	0.02	-1.29	1.29	adc	Activation rate of CTLs by Dendritic cells
0.01	0.01	1.17	1.17	kmc	CTL inhibition by MDSC
0.14	0.14	1.03	1.03	air	Activation rate of Treg by IL-2
0.01	0.01	0.60	0.60	axm	Maximal activation rate of MDSC by tumor
-0.01	0.01	-0.60	0.60	sm	Tumor cells saturation level for MDSC clonal expansion
0.10	0.10	0.49	0.49	mun	NK death rate
-0.01	0.01	-0.43	0.43	mc	Migration rate of CTL out of Lympoid tissue
0.10	0.10	0.43	0.43	axr	Activation rate of Treg by tumor
0.02	0.02	0.37	0.37	muc	CTL death rate
0.01	0.01	0.31	0.31	adr	Activation rate of Treg by mature Dendritic cells
0.01	0.01	0.23	0.23	krc	CTL inhibition by Treg
0.01	0.01	0.22	0.22	adfdr	Transformation rate of D_f cells to D_r
-0.05	0.05	-0.20	0.20	mui	IL-2 death rate
0.06	0.06	0.18	0.18	aci	Activation rate of IL-2 by CTL
0.00	0.00	0.09	0.09	adrr	Activation rate of Treg by regulatory dendritic cells.
0.01	0.01	0.09	0.09	mr	Migration rate of Treg out of Lymphoid tissue
0.00	0.00	-0.05	0.05	mud	Dendritic cells death rate
0.00	0.00	-0.04	0.04	axd	Activation rate of mature dendritic cells by tumor
0.00	0.00	0.03	0.03	si	IL-2 saturation level for CTL clonal expansion
0.00	0.00	-0.03	0.03	aic	Maximal activation rate of CTL by IL-2
-0.01	0.01	0.01	0.01	md	Migration rate of mature Dendritic cells out of prostate
0.00	0.00	0.00	0.00	ain	Maximal activation rate of NK by IL-2
0.00	0.00	0.00	0.00	sn	IL-2 saturation level for NK clonal expansion
0.00	0.00	0.00	0.00	lamICB	Degradation rate of ICB
0.00	0.00	0.00	0.00	lamAM	Degradation rate of anti-MDSC
0.00	0.00	0.00	0.00	ra1	ADPC death rate
0.00	0.00	0.00	0.00	rm	Mutation rate of AD into AI
0.00	0.00	0.00	0.00	rp2	Proliferation rate of AIPC
0.00	0.00	0.00	0.00	ra2	AIPC death rate
0.00	0.00	0.00	0.00	avd	Activation rate of mature Dendritic cells by vaccine
0.00	0.00	0.00	0.00	lamA	death rate of androgens
0.00	0.00	0.00	0.00	kantirr	Inhibition rate of Treg by anti-Treg drug
0.00	0.00	0.00	0.00	kantiii	Inhibition rate of IL-2 by anti-IL-2 drug
0.00	0.00	0.00	0.00	deltaICB	Effect of ICB drug on CTL killing rate
0.00	0.00	0.00	0.00	kantiM	Inhibition rate of MDSC by anti-MDSC drug
0.00	0.00	0.00	0.00	lamV	Degradation rate of vaccine
0.00	0.00	0.00	0.00	lamAI	Degradation rate of anti-IL-2
0.00	0.00	0.00	0.00	lamAR	Dengradation rate of anti-Treg

Figure A.1: Sensitivity analyses of mouse PCa model in untreated case. Local and globl ensitivity analyses on tumor size in the untreated case. The values are sorted by the highest GSA absolute values.

Androgen deprivation therapy					
LSA	abs LSA	GSA	abs GSA	Parameter	Parameter description
38.07	38.07	210.28	210.28	rp2	Proliferation rate of AIPC
-33.16	33.16	-159.79	159.79	ra2	AIPC death rate
0.65	0.65	8.00	8.00	rp1	Proliferation rate of ADPC
-0.26	0.26	-6.18	6.18	kcx	Maximal killing rate of tumor by CTL
-0.11	0.11	-5.71	5.71	mum	MDSC death rate
-0.20	0.20	-4.61	4.61	adc	Activation rate of CTLs by Dendritic cells
0.09	0.09	4.45	4.45	rhoM	source of MDSC
-0.08	0.08	-3.89	3.89	kNT	Maximal killing rate of tumor by NK
0.08	0.08	3.36	3.36	rm	Mutation rate of AD into AI
0.06	0.06	3.04	3.04	kmc	CTL inhibition by MDSC
0.06	0.06	2.93	2.93	kmn	NK cytotoxic effect MDSC-dependent inhibition
-0.11	0.11	-2.43	2.43	axd	Activation rate of mature dendritic cells by tumor
0.00	0.00	2.40	2.40	kxn	NK inactivation by tumor
0.20	0.20	2.34	2.34	krn	NK cytotoxic effect Treg-dependent inhibition
-0.19	0.19	-2.29	2.29	mur	Treg death rate
-0.05	0.05	-1.68	1.68	rhoN	Source of NK
0.02	0.02	1.60	1.60	axm	Maximal activation rate of MDSC by tumor
-0.02	0.02	-1.60	1.60	sm	Tumor cells saturation level for MDSC clonal expansion
0.13	0.13	1.29	1.29	air	Activation rate of Treg by IL-2
-0.07	0.07	-1.10	1.10	mc	Migration rate of CTL out of Lympoid tissue
0.06	0.06	0.99	0.99	adr	Activation rate of Treg by mature Dendritic cells
0.09	0.09	0.87	0.87	muc	CTL death rate
0.12	0.12	0.86	0.86	krc	CTL inhibition by Treg
0.00	0.00	0.71	0.71	md	Migration rate of mature Dendritic cells out of prostate
-0.06	0.06	-0.67	0.67	ra1	ADPC death rate
0.05	0.05	0.50	0.50	mun	NK death rate
0.03	0.03	0.44	0.44	adfdr	Transformation rate of D_f cells to D_r
0.04	0.04	0.42	0.42	axr	Activation rate of Treg by tumor
0.06	0.06	0.31	0.31	aci	Activation rate of IL-2 by CTL
-0.16	0.16	0.23	0.23	lamA	death rate of androgens
-0.03	0.03	-0.21	0.21	mui	IL-2 death rate
0.01	0.01	0.19	0.19	adrr	Activation rate of Treg by regulatory dendritic cells.
-0.01	0.01	-0.12	0.12	mud	Dendritic cells death rate
0.01	0.01	0.09	0.09	si	IL-2 saturation level for CTL clonal expansion
-0.01	0.01	-0.09	0.09	aic	Maximal activation rate of CTL by IL-2
0.01	0.01	0.04	0.04	mr	Migration rate of Treg out of Lymphoid tissue
0.00	0.00	0.00	0.00	ain	Maximal activation rate of NK by IL-2
0.00	0.00	0.00	0.00	sn	IL-2 saturation level for NK clonal expansion
0.00	0.00	0.00	0.00	lamAM	Degradation rate of anti-MDSC
0.00	0.00	0.00	0.00	avd	Activation rate of mature Dendritic cells by vaccine
0.00	0.00	0.00	0.00	kantirr	Inhibition rate of Treg by anti-Treg drug
0.00	0.00	0.00	0.00	kantiii	Inhibition rate of IL-2 by anti-IL-2 drug
0.00	0.00	0.00	0.00	lamICB	Degradation rate of ICB
0.00	0.00	0.00	0.00	deltaICB	Effect of ICB drug on CTL killing rate
0.00	0.00	0.00	0.00	kantiM	Inhibition rate of MDSC by anti-MDSC drug
0.00	0.00	0.00	0.00	lamV	Degradation rate of vaccine
0.00	0.00	0.00	0.00	lamAI	Degradation rate of anti-IL-2
0.00	0.00	0.00	0.00	lamAR	Dengradation rate of anti-Treg

Figure A.2: Sensitivity analyses of mouse PCa model under androgen deprivation therapy. Local and global sensitivity analyses on tumor size under androgen deprivation therapy. The values are sorted by the highest GSA absolute values.

Vaccine					
LSA	ABS	GSA	abs GSA	Parameter	Description
8.95	8.95	60.98	60.98	rp1	Proliferation rate of ADPC
-0.20	0.20	-5.75	5.75	kcx	Maximal killing rate of tumor by CTL
-0.08	0.08	-4.83	4.83	mum	MDSC death rate
-0.14	0.14	-4.07	4.07	adc	Activation rate of CTLs by Dendritic cells
0.07	0.07	3.99	3.99	rhoM	source of MDSC
-0.06	0.06	-3.29	3.29	kNT	Maximal killing rate of tumor by NK
0.05	0.05	2.83	2.83	kmc	CTL inhibition by MDSC
0.05	0.05	2.57	2.57	kmn	NK cytotoxic effect MDSC-dependent inhibition
0.00	0.00	2.06	2.06	kxn	NK inactivation by tumor
-0.06	0.06	-1.78	1.78	avd	Activation rate of mature Dendritic cells by vaccine
-0.16	0.16	-1.71	1.71	mur	Treg death rate
0.17	0.17	1.58	1.58	krn	NK cytotoxic effect Treg-dependent inhibition
-0.04	0.04	-1.28	1.28	rhoN	Source of NK
0.06	0.06	1.19	1.19	lamV	Degradation rate of vaccine
0.02	0.02	1.09	1.09	axm	Maximal activation rate of MDSC by tumor
-0.02	0.02	-1.09	1.09	sm	Tumor cells saturation level for MDSC clonal expansion
-0.06	0.06	-1.09	1.09	mc	Migration rate of CTL out of Lympoid tissue
0.11	0.11	0.99	0.99	air	Activation rate of Treg by IL-2
0.08	0.08	0.93	0.93	muc	CTL death rate
0.09	0.09	0.74	0.74	krc	CTL inhibition by Treg
0.04	0.04	0.69	0.69	adr	Activation rate of Treg by mature Dendritic cells
0.04	0.04	0.53	0.53	adfdr	Transformation rate of D_f cells to D_r
-0.02	0.02	0.48	0.48	md	Migration rate of mature Dendritic cells out of prostate
0.04	0.04	0.35	0.35	mun	NK death rate
0.04	0.04	0.29	0.29	axr	Activation rate of Treg by tumor
0.06	0.06	0.24	0.24	aci	Activation rate of IL-2 by CTL
0.01	0.01	0.17	0.17	adrr	Activation rate of Treg by regulatory dendritic cells.
-0.03	0.03	-0.15	0.15	mui	IL-2 death rate
0.00	0.00	-0.11	0.11	axd	Activation rate of mature dendritic cells by tumor
-0.01	0.01	-0.10	0.10	mud	Dendritic cells death rate
0.01	0.01	0.09	0.09	si	IL-2 saturation level for CTL clonal expansion
-0.01	0.01	-0.09	0.09	aic	Maximal activation rate of CTL by IL-2
0.01	0.01	0.02	0.02	mr	Migration rate of Treg out of Lymphoid tissue
0.00	0.00	0.00	0.00	ain	Maximal activation rate of NK by IL-2
0.00	0.00	0.00	0.00	sn	IL-2 saturation level for NK clonal expansion
0.00	0.00	0.00	0.00	lamAM	Degradation rate of anti-MDSC
0.00	0.00	0.00	0.00	ra1	ADPC death rate
0.00	0.00	0.00	0.00	rm	Mutation rate of AD into AI
0.00	0.00	0.00	0.00	rp2	Proliferation rate of AIPC
0.00	0.00	0.00	0.00	ra2	AIPC death rate
0.00	0.00	0.00	0.00	lamA	death rate of androgens
0.00	0.00	0.00	0.00	kantirr	Inhibition rate of Treg by anti-Treg drug
0.00	0.00	0.00	0.00	kantiii	Inhibition rate of IL-2 by anti-IL-2 drug
0.00	0.00	0.00	0.00	lamICB	Degradation rate of ICB
0.00	0.00	0.00	0.00	deltaICB	Effect of ICB drug on CTL killing rate
0.00	0.00	0.00	0.00	kantiM	Inhibition rate of MDSC by anti-MDSC drug
0.00	0.00	0.00	0.00	lamAI	Degradation rate of anti-IL-2
0.00	0.00	0.00	0.00	lamAR	Dengradation rate of anti-Treg

Figure A.3: Sensitivity analyses of mouse PCa model under vaccine therapy. Local and global sensitivity analyses on tumor size under vaccine therapy. The values are sorted by the highest GSA absolute values.

Androgen deprivation therapy + vaccine					
LSA	abs LSA	GSA	abs GSA	Parameter	Description
38.08	38.08	210.09	210.09	rp2	Proliferation rate of AIPC
-33.17	33.17	-159.94	159.94	ra2	AIPC death rate
-0.35	0.35	-8.91	8.91	kcx	Maximal killing rate of tumor by CTL
0.65	0.65	7.90	7.90	rp1	Proliferation rate of ADPC
-0.12	0.12	-7.32	7.32	mum	MDSC death rate
-0.27	0.27	-7.12	7.12	adc	Activation rate of CTLs by Dendritic cells
0.11	0.11	5.74	5.74	rhoM	source of MDSC
0.07	0.07	4.49	4.49	kmc	CTL inhibition by MDSC
-0.05	0.05	-3.15	3.15	kNT	Maximal killing rate of tumor by NK
0.08	0.08	3.14	3.14	rm	Mutation rate of AD into AI
0.06	0.06	2.79	2.79	kmn	NK cytotoxic effect MDSC-dependent inhibition
-0.11	0.11	-2.52	2.52	axd	Activation rate of mature dendritic cells by tumor
-0.18	0.18	-2.29	2.29	mur	Treg death rate
0.02	0.02	1.88	1.88	axm	Maximal activation rate of MDSC by tumor
-0.02	0.02	-1.88	1.88	sm	Tumor cells saturation level for MDSC clonal expansion
0.00	0.00	1.87	1.87	kxn	NK inactivation by tumor
-0.11	0.11	-1.72	1.72	mc	Migration rate of CTL out of Lympoid tissue
-0.06	0.06	-1.53	1.53	avd	Activation rate of mature Dendritic cells by vaccine
0.19	0.19	1.52	1.52	krc	CTL inhibition by Treg
0.11	0.11	1.42	1.42	krn	NK cytotoxic effect Treg-dependent inhibition
0.13	0.13	1.37	1.37	air	Activation rate of Treg by IL-2
0.07	0.07	1.33	1.33	adr	Activation rate of Treg by mature Dendritic cells
0.12	0.12	1.31	1.31	muc	CTL death rate
0.00	0.00	1.19	1.19	md	Migration rate of mature Dendritic cells out of prostate
-0.02	0.02	-1.17	1.17	rhoN	Source of NK
0.05	0.05	0.95	0.95	lamV	Degradation rate of vaccine
0.05	0.05	0.70	0.70	adfdr	Transformation rate of D_f cells to D_r
-0.06	0.06	-0.67	0.67	ra1	ADPC death rate
0.07	0.07	0.39	0.39	aci	Activation rate of IL-2 by CTL
0.02	0.02	0.37	0.37	mun	NK death rate
0.03	0.03	0.35	0.35	axr	Activation rate of Treg by tumor
0.02	0.02	0.27	0.27	adrr	Activation rate of Treg by regulatory dendritic cells.
-0.03	0.03	-0.20	0.20	mui	IL-2 death rate
0.02	0.02	0.17	0.17	si	IL-2 saturation level for CTL clonal expansion
-0.02	0.02	-0.17	0.17	aic	Maximal activation rate of CTL by IL-2
-0.01	0.01	-0.16	0.16	mud	Dendritic cells death rate
-0.16	0.16	0.13	0.13	lamA	death rate of androgens
0.00	0.00	0.01	0.01	mr	Migration rate of Treg out of Lymphoid tissue
0.00	0.00	0.00	0.00	ain	Maximal activation rate of NK by IL-2
0.00	0.00	0.00	0.00	sn	IL-2 saturation level for NK clonal expansion
0.00	0.00	0.00	0.00	lamAM	Degradation rate of anti-MDSC
0.00	0.00	0.00	0.00	kantirr	Inhibition rate of Treg by anti-Treg drug
0.00	0.00	0.00	0.00	kantiii	Inhibition rate of IL-2 by anti-IL-2 drug
0.00	0.00	0.00	0.00	lamICB	Degradation rate of ICB
0.00	0.00	0.00	0.00	deltaICB	Effect of ICB drug on CTL killing rate
0.00	0.00	0.00	0.00	kantiM	Inhibition rate of MDSC by anti-MDSC drug
0.00	0.00	0.00	0.00	lamAI	Degradation rate of anti-IL-2
0.00	0.00	0.00	0.00	lamAR	Dengradation rate of anti-Treg

Figure A.4: Sensitivity analyses of mouse PCa model under androgen deprivation + vaccine combination therapy. Local and global sensitivity analyses on tumor size under androgen deprivation + vaccine combination therapy. The values are sorted by the highest GSA absolute values.

Androgen deprivation therapy + anti-IL2					
LSA	abs LSA	GSA	abs GSA	Parameter	Description
38.28	38.28	214.41	214.41	rp2	Proliferation rate of AIPC
-33.30	33.30	-161.46	161.46	ra2	AIPC death rate
0.66	0.66	8.23	8.23	rp1	Proliferation rate of ADPC
0.00	0.00	-6.69	6.69	kcx	Maximal killing rate of tumor by CTL
-0.02	0.02	-6.32	6.32	mum	MDSC death rate
0.06	0.06	5.08	5.08	krn	NK cytotoxic effect Treg-dependent inhibition
0.33	0.33	-5.03	5.03	kNT	Maximal killing rate of tumor by NK
-0.12	0.12	4.77	4.77	rhoM	source of MDSC
-0.23	0.23	-4.58	4.58	adc	Activation rate of CTLs by Dendritic cells
0.08	0.08	3.77	3.77	rm	Mutation rate of AD into AI
-0.01	0.01	-3.38	3.38	mur	Treg death rate
0.02	0.02	3.22	3.22	kmc	CTL inhibition by MDSC
0.00	0.00	3.20	3.20	kxn	NK inactivation by tumor
0.07	0.07	3.19	3.19	kmn	NK cytotoxic effect MDSC-dependent inhibition
0.00	0.00	-2.53	2.53	rhoN	Source of NK
0.09	0.09	1.98	1.98	adr	Activation rate of Treg by mature Dendritic cells
-0.07	0.07	-1.76	1.76	axd	Activation rate of mature dendritic cells by tumor
0.00	0.00	1.73	1.73	axm	Maximal activation rate of MDSC by tumor
-0.16	0.16	-1.73	1.73	sm	Tumor cells saturation level for MDSC clonal expansion
-0.07	0.07	-1.06	1.06	mc	Migration rate of CTL out of Lympoid tissue
-0.16	0.16	0.90	0.90	muc	CTL death rate
0.06	0.06	0.81	0.81	axr	Activation rate of Treg by tumor
0.04	0.04	0.75	0.75	air	Activation rate of Treg by IL-2
-0.06	0.06	-0.70	0.70	ra1	ADPC death rate
0.11	0.11	0.68	0.68	krc	CTL inhibition by Treg
0.00	0.00	0.67	0.67	mun	NK death rate
0.02	0.02	0.48	0.48	adfdr	Transformation rate of D_f cells to D_r
0.12	0.12	0.41	0.41	lamA	death rate of androgens
0.01	0.01	-0.38	0.38	kantiii	Inhibition rate of IL-2 by anti-IL-2 drug
0.08	0.08	0.29	0.29	aci	Activation rate of IL-2 by CTL
-0.30	0.30	0.28	0.28	adrr	Activation rate of Treg by regulatory dendritic cells.
-0.06	0.06	0.27	0.27	md	Migration rate of mature Dendritic cells out of prostate
0.00	0.00	0.22	0.22	lamAI	Degradation rate of anti-IL-2
0.11	0.11	-0.17	0.17	mud	Dendritic cells death rate
-0.28	0.28	0.12	0.12	mr	Migration rate of Treg out of Lymphoid tissue
-0.01	0.01	-0.05	0.05	mui	IL-2 death rate
0.10	0.10	0.04	0.04	si	IL-2 saturation level for CTL clonal expansion
0.01	0.01	-0.04	0.04	aic	Maximal activation rate of CTL by IL-2
-0.11	0.11	0.00	0.00	ain	Maximal activation rate of NK by IL-2
-0.01	0.01	0.00	0.00	sn	IL-2 saturation level for NK clonal expansion
0.00	0.00	0.00	0.00	lamAM	Degradation rate of anti-MDSC
0.00	0.00	0.00	0.00	avd	Activation rate of mature Dendritic cells by vaccine
-0.04	0.04	0.00	0.00	kantirr	Inhibition rate of Treg by anti-Treg drug
0.00	0.00	0.00	0.00	lamICB	Degradation rate of ICB
0.00	0.00	0.00	0.00	deltaICB	Effect of ICB drug on CTL killing rate
0.00	0.00	0.00	0.00	kantiM	Inhibition rate of MDSC by anti-MDSC drug
0.05	0.05	0.00	0.00	lamV	Degradation rate of vaccine
0.12	0.12	0.00	0.00	lamAR	Dengradation rate of anti-Treg

Figure A.5: Sensitivity analyses of mouse PCa model under androgen deprivation + anti-IL2 combination therapy. Local and global sensitivity analyses on tumor size under androgen deprivation + anti-IL2 combination therapy. The values are sorted by the highest GSA absolute values.

Androgen deprivation therapy + anti-Treg					
LSA	abs LSA	GSA	abs GSA	Parameter	Description
38.32	38.32	237.94	237.94	rp2	Proliferation rate of AIPC
-0.58	0.58	-173.89	173.89	kNT	Maximal killing rate of tumor by NK
-33.32	33.32	-173.58	173.58	ra2	AIPC death rate
-0.34	0.34	-105.06	105.06	rhoN	Source of NK
0.39	0.39	90.38	90.38	krn	NK cytotoxic effect Treg-dependent inhibition
-0.27	0.27	-79.23	79.23	kantirr	Inhibition rate of Treg by anti-Treg drug
0.01	0.01	65.11	65.11	kxn	NK inactivation by tumor
0.41	0.41	45.76	45.76	lamAR	Dengradation rate of anti-Treg
0.34	0.34	44.29	44.29	mun	NK death rate
0.27	0.27	38.16	38.16	air	Activation rate of Treg by IL-2
0.11	0.11	19.60	19.60	adr	Activation rate of Treg by mature Dendritic cells
-0.07	0.07	-19.47	19.47	md	Migration rate of mature Dendritic cells out of prostate
-0.06	0.06	16.82	16.82	axd	Activation rate of mature dendritic cells by tumor
0.66	0.66	15.77	15.77	rp1	Proliferation rate of ADPC
-0.12	0.12	-11.20	11.20	mur	Treg death rate
0.16	0.16	10.62	10.62	aci	Activation rate of IL-2 by CTL
-0.08	0.08	-8.80	8.80	mui	IL-2 death rate
-0.34	0.34	-7.68	7.68	kcx	Maximal killing rate of tumor by CTL
0.09	0.09	7.33	7.33	rm	Mutation rate of AD into AI
0.06	0.06	6.78	6.78	kmn	NK cytotoxic effect MDSC-dependent inhibition
-0.12	0.12	-6.00	6.00	mum	MDSC death rate
0.10	0.10	5.10	5.10	rhoM	source of MDSC
0.08	0.08	4.18	4.18	axr	Activation rate of Treg by tumor
0.06	0.06	-2.52	2.52	kmc	CTL inhibition by MDSC
-0.19	0.19	2.49	2.49	adc	Activation rate of CTLs by Dendritic cells
-0.16	0.16	2.04	2.04	lamA	death rate of androgens
0.01	0.01	1.10	1.10	mr	Migration rate of Treg out of Lymphoid tissue
-0.02	0.02	-1.04	1.04	sm	Tumor cells saturation level for MDSC clonal expansion
0.02	0.02	1.04	1.04	axm	Maximal activation rate of MDSC by tumor
-0.06	0.06	-1.00	1.00	ra1	ADPC death rate
0.10	0.10	-0.65	0.65	muc	CTL death rate
-0.06	0.06	0.47	0.47	mc	Migration rate of CTL out of Lympoid tissue
0.01	0.01	0.31	0.31	adrr	Activation rate of Treg by regulatory dendritic cells.
0.00	0.00	-0.28	0.28	ain	Maximal activation rate of NK by IL-2
0.00	0.00	0.27	0.27	sn	IL-2 saturation level for NK clonal expansion
-0.01	0.01	-0.22	0.22	mud	Dendritic cells death rate
0.04	0.04	0.03	0.03	adfdr	Transformation rate of D_f cells to D_r
0.09	0.09	-0.03	0.03	krc	CTL inhibition by Treg
-0.02	0.02	0.03	0.03	aic	Maximal activation rate of CTL by IL-2
0.02	0.02	-0.03	0.03	si	IL-2 saturation level for CTL clonal expansion
0.00	0.00	0.00	0.00	lamAM	Degradation rate of anti-MDSC
0.00	0.00	0.00	0.00	avd	Activation rate of mature Dendritic cells by vaccine
0.00	0.00	0.00	0.00	kantiii	Inhibition rate of IL-2 by anti-IL-2 drug
0.00	0.00	0.00	0.00	lamICB	Degradation rate of ICB
0.00	0.00	0.00	0.00	deltaICB	Effect of ICB drug on CTL killing rate
0.00	0.00	0.00	0.00	kantiM	Inhibition rate of MDSC by anti-MDSC drug
0.00	0.00	0.00	0.00	lamV	Degradation rate of vaccine
0.00	0.00	0.00	0.00	lamAI	Degradation rate of anti-IL-2

Figure A.6: Sensitivity analyses of mouse PCa model under androgen deprivation + anti-Treg combination therapy. Local and global sensitivity analyses on tumor size under androgen deprivation + anti-Treg combination therapy. The values are sorted by the highest GSA absolute values.

Androgen deprivation therapy + vaccine + anti-Treg					
LSA	abs LSA	GSA	abs GSA	Parameter	Description
38.20	38.20	227.82	227.82	rp2	Proliferation rate of AIPC
-33.26	33.26	-169.59	169.59	ra2	AIPC death rate
-0.45	0.45	-76.03	76.03	kNT	Maximal killing rate of tumor by NK
0.35	0.35	65.64	65.64	krn	NK cytotoxic effect Treg-dependent inhibition
-0.30	0.30	-58.72	58.72	kantirr	Inhibition rate of Treg by anti-Treg drug
-0.25	0.25	-41.74	41.74	rhoN	Source of NK
0.01	0.01	37.83	37.83	kxn	NK inactivation by tumor
0.43	0.43	31.39	31.39	lamAR	Dengradation rate of anti-Treg
0.13	0.13	25.50	25.50	adr	Activation rate of Treg by mature Dendritic cells
-0.07	0.07	-23.02	23.02	md	Migration rate of mature Dendritic cells out of prostate
0.30	0.30	20.49	20.49	air	Activation rate of Treg by IL-2
0.25	0.25	16.43	16.43	mun	NK death rate
-0.04	0.04	12.64	12.64	avd	Activation rate of mature Dendritic cells by vaccine
0.66	0.66	12.17	12.17	rp1	Proliferation rate of ADPC
-0.49	0.49	-11.22	11.22	kcx	Maximal killing rate of tumor by CTL
-0.16	0.16	-8.58	8.58	mum	MDSC death rate
-0.12	0.12	-7.59	7.59	mur	Treg death rate
0.14	0.14	7.21	7.21	rhoM	source of MDSC
0.19	0.19	7.08	7.08	aci	Activation rate of IL-2 by CTL
-0.09	0.09	6.60	6.60	axd	Activation rate of mature dendritic cells by tumor
0.04	0.04	-5.98	5.98	lamV	Degradation rate of vaccine
0.06	0.06	5.71	5.71	kmn	NK cytotoxic effect MDSC-dependent inhibition
0.08	0.08	5.43	5.43	rm	Mutation rate of AD into AI
-0.07	0.07	-4.27	4.27	mui	IL-2 death rate
0.06	0.06	2.89	2.89	axr	Activation rate of Treg by tumor
-0.31	0.31	-1.89	1.89	adc	Activation rate of CTLs by Dendritic cells
0.02	0.02	1.49	1.49	axm	Maximal activation rate of MDSC by tumor
-0.02	0.02	-1.49	1.49	sm	Tumor cells saturation level for MDSC clonal expansion
0.11	0.11	1.44	1.44	kmc	CTL inhibition by MDSC
-0.16	0.16	1.19	1.19	lamA	death rate of androgens
-0.06	0.06	-0.88	0.88	ra1	ADPC death rate
0.00	0.00	0.51	0.51	mr	Migration rate of Treg out of Lymphoid tissue
-0.11	0.11	-0.46	0.46	mc	Migration rate of CTL out of Lympoid tissue
0.18	0.18	0.43	0.43	muc	CTL death rate
0.06	0.06	0.37	0.37	adfdr	Transformation rate of D_f cells to D_r
0.01	0.01	0.31	0.31	adrr	Activation rate of Treg by regulatory dendritic cells.
-0.01	0.01	-0.21	0.21	mud	Dendritic cells death rate
0.17	0.17	0.21	0.21	krc	CTL inhibition by Treg
0.00	0.00	-0.11	0.11	ain	Maximal activation rate of NK by IL-2
0.00	0.00	0.11	0.11	sn	IL-2 saturation level for NK clonal expansion
0.05	0.05	0.08	0.08	si	IL-2 saturation level for CTL clonal expansion
-0.05	0.05	-0.08	0.08	aic	Maximal activation rate of CTL by IL-2
0.00	0.00	0.00	0.00	lamAM	Degradation rate of anti-MDSC
0.00	0.00	0.00	0.00	kantiii	Inhibition rate of IL-2 by anti-IL-2 drug
0.00	0.00	0.00	0.00	lamICB	Degradation rate of ICB
0.00	0.00	0.00	0.00	deltaICB	Effect of ICB drug on CTL killing rate
0.00	0.00	0.00	0.00	kantiM	Inhibition rate of MDSC by anti-MDSC drug
0.00	0.00	0.00	0.00	lamAI	Degradation rate of anti-IL-2

Figure A.7: Sensitivity analyses of mouse PCa model under androgen deprivation + vaccine + anti-Treg combination therapy. Local and global sensitivity analyses on tumor size under androgen deprivation + vaccine + anti-Treg combination therapy. The values are sorted by the highest GSA absolute values.

Androgen deprivation therapy + Immune checkpoint blockade					
LSA	ABS LSA	GSA	ABS GSA	Parameter	Description
-5.47	5.47	-98.09	98.09	kcx	Maximal killing rate of tumor by CTL
-5.25	5.25	-95.83	95.83	deltaICB	Effect of ICB drug on CTL killing rate
-4.46	4.46	-87.59	87.59	adc	Activation rate of CTLs by Dendritic cells
-1.31	1.31	-79.24	79.24	mum	MDSC death rate
-27.06	27.06	-76.63	76.63	ra2	AIPC death rate
1.12	1.12	65.48	65.48	rhoM	source of MDSC
-3.35	3.35	-64.25	64.25	axd	Activation rate of mature dendritic cells by tumor
1.23	1.23	59.30	59.30	kmc	CTL inhibition by MDSC
3.94	3.94	56.74	56.74	lamICB	Degradation rate of ICB
27.58	27.58	50.34	50.34	rp2	Proliferation rate of AIPC
-2.51	2.51	-29.73	29.73	mur	Treg death rate
-1.83	1.83	-27.78	27.78	mc	Migration rate of CTL out of Lympoid tissue
3.08	3.08	26.81	26.81	krc	CTL inhibition by Treg
2.14	2.14	22.50	22.50	muc	CTL death rate
0.99	0.99	19.30	19.30	adfdr	Transformation rate of D_f cells to D_r
1.87	1.87	19.07	19.07	air	Activation rate of Treg by IL-2
0.65	0.65	8.70	8.70	adr	Activation rate of Treg by mature Dendritic cells
1.08	1.08	8.51	8.51	aci	Activation rate of IL-2 by CTL
-0.18	0.18	-7.94	7.94	sm	Tumor cells saturation level for MDSC clonal expansion
0.18	0.18	7.94	7.94	axm	Maximal activation rate of MDSC by tumor
0.34	0.34	7.17	7.17	md	Migration rate of mature Dendritic cells out of prostate
-0.58	0.58	-5.26	5.26	mui	IL-2 death rate
0.24	0.24	4.11	4.11	adrr	Activation rate of Treg by regulatory dendritic cells.
-0.06	0.06	-3.37	3.37	rm	Mutation rate of AD into AI
0.40	0.40	3.16	3.16	si	IL-2 saturation level for CTL clonal expansion
-0.40	0.40	-3.16	3.16	aic	Maximal activation rate of CTL by IL-2
-0.20	0.20	-3.05	3.05	mud	Dendritic cells death rate
0.37	0.37	2.50	2.50	axr	Activation rate of Treg by tumor
-0.15	0.15	-2.34	2.34	lamA	death rate of androgens
-0.04	0.04	-0.63	0.63	rhoN	Source of NK
0.05	0.05	0.50	0.50	kmn	NK cytotoxic effect MDSC-dependent inhibition
-0.05	0.05	-0.49	0.49	kNT	Maximal killing rate of tumor by NK
0.01	0.01	-0.41	0.41	mr	Migration rate of Treg out of Lymphoid tissue
0.04	0.04	0.28	0.28	mun	NK death rate
0.13	0.13	0.13	0.13	krn	NK cytotoxic effect Treg-dependent inhibition
0.29	0.29	0.11	0.11	rp1	Proliferation rate of ADPC
-0.03	0.03	-0.11	0.11	ra1	ADPC death rate
0.00	0.00	0.08	0.08	kxn	NK inactivation by tumor
0.00	0.00	0.00	0.00	ain	Maximal activation rate of NK by IL-2
0.00	0.00	0.00	0.00	sn	IL-2 saturation level for NK clonal expansion
0.00	0.00	0.00	0.00	lamAM	Degradation rate of anti-MDSC
0.00	0.00	0.00	0.00	avd	Activation rate of mature Dendritic cells by vaccine
0.00	0.00	0.00	0.00	kantirr	Inhibition rate of Treg by anti-Treg drug
0.00	0.00	0.00	0.00	kantiii	Inhibition rate of IL-2 by anti-IL-2 drug
0.00	0.00	0.00	0.00	kantiM	Inhibition rate of MDSC by anti-MDSC drug
0.00	0.00	0.00	0.00	lamV	Degradation rate of vaccine
0.00	0.00	0.00	0.00	lamAI	Degradation rate of anti-IL-2
0.00	0.00	0.00	0.00	lamAR	Dengradation rate of anti-Treg

Figure A.8: Sensitivity analyses of mouse PCa model under androgen deprivation + immune checkpoint blockade combination therapy. Local and global sensitivity analyses on tumor size under androgen deprivation + immune checkpoint blockade combination therapy. The values are sorted by the highest GSA absolute values.

Androge deprivation therapy + anti-MDSC					
LSA	ABS LSA	GSA	ABS GSA	Parameter	Description
38.23	38.23	252.778	252.78	rp2	Proliferation rate of AIPC
-33.32	33.32	-195.332	195.33	ra2	AIPC death rate
-0.76	0.76	-23.0627	23.06	kNT	Maximal killing rate of tumor by NK
-0.69	0.69	-19.5655	19.57	rhoN	Source of NK
0.02	0.02	16.8539	16.85	kxn	NK inactivation by tumor
-0.31	0.31	-14.0105	14.01	kcx	Maximal killing rate of tumor by CTL
0.22	0.22	12.7313	12.73	kmn	NK cytotoxic effect MDSC-dependent inhibition
0.19	0.19	11.5637	11.56	rhoM	source of MDSC
-0.24	0.24	-11.3853	11.39	adc	Activation rate of CTLs by Dendritic cells
0.65	0.65	9.49143	9.49	rp1	Proliferation rate of ADPC
0.22	0.22	7.24568	7.25	lamAM	Degradation rate of anti-MDSC
-0.13	0.13	-6.09555	6.10	axd	Activation rate of mature dendritic cells by tumor
-0.23	0.23	-5.6008	5.60	mur	Treg death rate
-0.06	0.06	-5.17332	5.17	mum	MDSC death rate
0.17	0.17	4.68966	4.69	krc	CTL inhibition by Treg
0.02	0.02	3.83778	3.84	kmc	CTL inhibition by MDSC
-0.09	0.09	-3.77448	3.77	kantiM	Inhibition rate of MDSC by anti-MDSC drug
0.08	0.08	3.68106	3.68	rm	Mutation rate of AD into AI
0.13	0.13	3.22405	3.22	muc	CTL death rate
0.68	0.68	3.08348	3.08	mun	NK death rate
0.16	0.16	3.08341	3.08	air	Activation rate of Treg by IL-2
0.04	0.04	3.02284	3.02	axm	Maximal activation rate of MDSC by tumor
-0.04	0.04	-3.02278	3.02	sm	Tumor cells saturation level for MDSC clonal expansion
0.07	0.07	2.93497	2.93	adr	Activation rate of Treg by mature Dendritic cells
-0.09	0.09	-2.92812	2.93	mc	Migration rate of CTL out of Lympoid tissue
0.19	0.19	1.99478	1.99	krn	NK cytotoxic effect Treg-dependent inhibition
-0.01	0.01	1.33784	1.34	md	Migration rate of mature Dendritic cells out of prostate
0.04	0.04	1.25305	1.25	adfdr	Transformation rate of D_f cells to D_r
0.05	0.05	1.18545	1.19	axr	Activation rate of Treg by tumor
-0.06	0.06	-0.84111	0.84	ra1	ADPC death rate
0.07	0.07	0.79911	0.80	aci	Activation rate of IL-2 by CTL
-0.04	0.04	-0.51237	0.51	mui	IL-2 death rate
0.01	0.01	0.4112	0.41	adrr	Activation rate of Treg by regulatory dendritic cells.
0.02	0.02	0.40275	0.40	si	IL-2 saturation level for CTL clonal expansion
-0.02	0.02	-0.40272	0.40	aic	Maximal activation rate of CTL by IL-2
-0.01	0.01	-0.26517	0.27	mud	Dendritic cells death rate
0.01	0.01	0.09003	0.09	mr	Migration rate of Treg out of Lymphoid tissue
-0.01	0.01	-0.02577	0.03	ain	Maximal activation rate of NK by IL-2
0.01	0.01	0.02551	0.03	sn	IL-2 saturation level for NK clonal expansion
-0.16	0.16	-0.00384	0.00	lamA	death rate of androgens
0.00	0.00	0	0.00	avd	Activation rate of mature Dendritic cells by vaccine
0.00	0.00	0	0.00	kantirr	Inhibition rate of Treg by anti-Treg drug
0.00	0.00	0	0.00	kantiii	Inhibition rate of IL-2 by anti-IL-2 drug
0.00	0.00	0	0.00	lamICB	Degradation rate of ICB
0.00	0.00	0	0.00	deltaICB	Effect of ICB drug on CTL killing rate
0.00	0.00	0	0.00	lamV	Degradation rate of vaccine
0.00	0.00	0	0.00	lamAI	Degradation rate of anti-IL-2
0.00	0.00	0	0.00	lamAR	Dengradation rate of anti-Treg

Figure A.9: Sensitivity analyses of mouse PCa model under androgen deprivation + anti-MDSC combination therapy. Local and global sensitivity analyses on tumor size under androgen deprivation + anti-MDSC combination therapy. The values are sorted by the highest GSA absolute values.

Androgen deprivation therapy + Immune checkpoint blockade + anti-MDSC					
LSA	ABS LSA	GSA	ABS GSA	Parameter	Description
-6.42	6.42	-115.11	115.11	kcx	Maximal killing rate of tumor by CTL
-26.39	26.39	-112.76	112.76	ra2	AIPC death rate
-6.16	6.16	-110.98	110.98	deltaICB	Effect of ICB drug on CTL killing rate
26.74	26.74	105.16	105.16	rp2	Proliferation rate of AIPC
-4.96	4.96	-100.30	100.30	adc	Activation rate of CTLs by Dendritic cells
4.36	4.36	66.56	66.56	krc	CTL inhibition by Treg
4.51	4.51	65.27	65.27	lamICB	Degradation rate of ICB
-3.57	3.57	-62.12	62.12	axd	Activation rate of mature dendritic cells by tumor
-3.50	3.50	-58.10	58.10	mur	Treg death rate
-0.65	0.65	-35.84	35.84	rhoN	Source of NK
-0.70	0.70	-35.82	35.82	kNT	Maximal killing rate of tumor by NK
2.90	2.90	35.48	35.48	muc	CTL death rate
2.68	2.68	32.80	32.80	air	Activation rate of Treg by IL-2
-2.09	2.09	-32.36	32.36	mc	Migration rate of CTL out of Lympoid tissue
0.26	0.26	31.65	31.65	rhoM	source of MDSC
0.36	0.36	27.84	27.84	lamAM	Degradation rate of anti-MDSC
0.93	0.93	23.24	23.24	adr	Activation rate of Treg by mature Dendritic cells
1.14	1.14	18.92	18.92	adfdr	Transformation rate of D_f cells to D_r
1.56	1.56	14.18	14.18	aci	Activation rate of IL-2 by CTL
-0.13	0.13	-13.44	13.44	kantiM	Inhibition rate of MDSC by anti-MDSC drug
0.19	0.19	12.78	12.78	kmn	NK cytotoxic effect MDSC-dependent inhibition
0.09	0.09	11.20	11.20	kmc	CTL inhibition by MDSC
0.64	0.64	10.96	10.96	mun	NK death rate
0.01	0.01	10.74	10.74	kxn	NK inactivation by tumor
-0.80	0.80	-8.34	8.34	mui	IL-2 death rate
0.50	0.50	6.47	6.47	axr	Activation rate of Treg by tumor
0.59	0.59	5.17	5.17	si	IL-2 saturation level for CTL clonal expansion
-0.58	0.58	-5.17	5.17	aic	Maximal activation rate of CTL by IL-2
0.28	0.28	5.01	5.01	adrr	Activation rate of Treg by regulatory dendritic cells.
-0.23	0.23	-3.94	3.94	mud	Dendritic cells death rate
-0.02	0.02	-3.81	3.81	mum	MDSC death rate
0.27	0.27	2.61	2.61	rp1	Proliferation rate of ADPC
-0.06	0.06	-2.31	2.31	rm	Mutation rate of AD into AI
0.03	0.03	2.21	2.21	axm	Maximal activation rate of MDSC by tumor
-0.03	0.03	-2.21	2.21	sm	Tumor cells saturation level for MDSC clonal expansion
-0.14	0.14	-2.02	2.02	lamA	death rate of androgens
0.13	0.13	-1.25	1.25	md	Migration rate of mature Dendritic cells out of prostate
0.05	0.05	0.37	0.37	mr	Migration rate of Treg out of Lymphoid tissue
0.12	0.12	0.32	0.32	krn	NK cytotoxic effect Treg-dependent inhibition
-0.03	0.03	-0.28	0.28	ra1	ADPC death rate
-0.01	0.01	-0.12	0.12	ain	Maximal activation rate of NK by IL-2
0.01	0.01	0.12	0.12	sn	IL-2 saturation level for NK clonal expansion
0.00	0.00	0.00	0.00	avd	Activation rate of mature Dendritic cells by vaccine
0.00	0.00	0.00	0.00	kantirr	Inhibition rate of Treg by anti-Treg drug
0.00	0.00	0.00	0.00	kantiii	Inhibition rate of IL-2 by anti-IL-2 drug
0.00	0.00	0.00	0.00	lamV	Degradation rate of vaccine
0.00	0.00	0.00	0.00	lamAI	Degradation rate of anti-IL-2
0.00	0.00	0.00	0.00	lamAR	Dengradation rate of anti-Treg

Figure A.10: Sensitivity analyses of mouse PCa model under androgen deprivation + immune checkpoint blockade + anti-MDSC combination therapy. Local and global sensitivity analyses on tumor size under androgen deprivation + immune checkpoint blockade + anti-MDSC combination therapy. The values are sorted by the highest GSA absolute values.

NK infusion					
LSA	abs LSA	GSA	abs GSA	Parameter	Description
9.04	9.04	60.74	60.74	rp1	Proliferation rate of ADPC
-0.53	0.53	-15.04	15.04	kNT	Maximal killing rate of tumor by NK
1.15	1.15	12.33	12.33	krn	NK cytotoxic effect Treg-dependent inhibition
0.21	0.21	10.66	10.66	kmn	NK cytotoxic effect MDSC-dependent inhibition
0.01	0.01	9.05	9.05	kxn	NK inactivation by tumor
-0.15	0.15	-4.37	4.37	mum	MDSC death rate
0.13	0.13	3.80	3.80	rhoM	source of MDSC
-0.60	0.60	-3.07	3.07	mur	Treg death rate
-0.08	0.08	-2.75	2.75	kcx	Maximal killing rate of tumor by CTL
0.41	0.41	2.08	2.08	mun	NK death rate
0.36	0.36	1.90	1.90	air	Activation rate of Treg by IL-2
-0.10	0.10	-1.43	1.43	rhoN	Source of NK
0.01	0.01	-1.10	1.10	adc	Activation rate of CTLs by Dendritic cells
0.00	0.00	1.04	1.04	kmc	CTL inhibition by MDSC
0.06	0.06	0.95	0.95	adr	Activation rate of Treg by mature Dendritic cells
0.02	0.02	0.84	0.84	axm	Maximal activation rate of MDSC by tumor
-0.02	0.02	-0.84	0.84	sm	Tumor cells saturation level for MDSC clonal expansion
0.20	0.20	0.55	0.55	axr	Activation rate of Treg by tumor
0.00	0.00	-0.39	0.39	mc	Migration rate of CTL out of Lympoid tissue
-0.01	0.01	0.33	0.33	muc	CTL death rate
-0.10	0.10	-0.26	0.26	mui	IL-2 death rate
0.12	0.12	0.24	0.24	aci	Activation rate of IL-2 by CTL
0.01	0.01	0.22	0.22	adfdr	Transformation rate of D_f cells to D_r
-0.06	0.06	-0.20	0.20	md	Migration rate of mature Dendritic cells out of prostate
-0.01	0.01	0.20	0.20	krc	CTL inhibition by Treg
0.04	0.04	0.18	0.18	mr	Migration rate of Treg out of Lymphoid tissue
0.01	0.01	0.11	0.11	adrr	Activation rate of Treg by regulatory dendritic cells.
-0.01	0.01	-0.06	0.06	mud	Dendritic cells death rate
0.00	0.00	0.02	0.02	si	IL-2 saturation level for CTL clonal expansion
0.00	0.00	-0.02	0.02	aic	Maximal activation rate of CTL by IL-2
0.01	0.01	-0.01	0.01	axd	Activation rate of mature dendritic cells by tumor
0.00	0.00	-0.01	0.01	ain	Maximal activation rate of NK by IL-2
0.00	0.00	0.01	0.01	sn	IL-2 saturation level for NK clonal expansion
0.00	0.00	0.00	0.00	lamAM	Degradation rate of anti-MDSC
0.00	0.00	0.00	0.00	ra1	ADPC death rate
0.00	0.00	0.00	0.00	rm	Mutation rate of AD into AI
0.00	0.00	0.00	0.00	rp2	Proliferation rate of AIPC
0.00	0.00	0.00	0.00	ra2	AIPC death rate
0.00	0.00	0.00	0.00	avd	Activation rate of mature Dendritic cells by vaccine
0.00	0.00	0.00	0.00	lamA	death rate of androgens
0.00	0.00	0.00	0.00	kantirr	Inhibition rate of Treg by anti-Treg drug
0.00	0.00	0.00	0.00	kantiii	Inhibition rate of IL-2 by anti-IL-2 drug
0.00	0.00	0.00	0.00	lamICB	Degradation rate of ICB
0.00	0.00	0.00	0.00	deltaICB	Effect of ICB drug on CTL killing rate
0.00	0.00	0.00	0.00	kantiM	Inhibition rate of MDSC by anti-MDSC drug
0.00	0.00	0.00	0.00	lamV	Degradation rate of vaccine
0.00	0.00	0.00	0.00	lamAI	Degradation rate of anti-IL-2
0.00	0.00	0.00	0.00	lamAR	Dengradation rate of anti-Treg

Figure A.11: Sensitivity analyses of mouse PCa model under NK infusion. Local and global sensitivity analyses on tumor size under NK infusion. The values are sorted by the highest GSA absolute values.

Appendix B

Local Sensitivity Analysis of human PCa model

This appendix includes the results of the LSA on tumor size. The LSA value has been computed by the formula:

$$LSA(p) = \frac{X(t_f, p + 1\%p) - X(t_f, p - 1\%p)}{0.02 \cdot X(t_f, p)},$$

by fixing the simulation time $t_f = 4$ months (Figure B.1) and $t_f = 6$ months (Figure B.2). These results are discussed in Section 3.2 .

LSA	ABS	Parameter	Description
1.14	1.14	r_1	proliferation rate of ADPC
0.52	0.52	a_0	baseline level of androgen
0.39	0.39	K	tumor carrying capacity
0.00	0.00	e_{CX}	killing rate of tumor by CTL
0.00	0.00	k_R	inactivation rate of CTL by Treg
0.00	0.00	e_C	activation rate of CTL by dendritic cells
0.00	0.00	a_{IR}	activation rate of Treg by IL-2
0.00	0.00	μ_R	death rate of Treg
0.00	0.00	g_C	dendritic cells saturation level for CTL clonal expansion
0.00	0.00	μ_D	death rate of dendritic cells
0.00	0.00	s_D	source of dendritic cells
0.00	0.00	μ_I	death rate of IL-2
0.00	0.00	e_I	activation rate of IL-2 by CTL and tumor
0.00	0.00	g_{CX}	CTL saturation level for tumor cells inhibition
0.00	0.00	g_I	tumor cells saturation level for CTL stimulation of IL-2
0.00	0.00	a_R	activation rate of Treg by IL-2
0.00	0.00	μ_C	death rate of CTL
0.00	0.00	e_{IC}	activation rate of CTL by IL-2
0.00	0.00	g_{IC}	IL-2 saturation level for CTL clonal expansion
0.00	0.00	k_{ip}	Killing rate of tumor by CTL due to ipilimumab drug
0.00	0.00	I_{p0}	Ipilimumab dose
0.00	0.00	λ_P	degradation rate of ipilimumab
0.00	0.00	μ_1	death rate of ADPC
0.00	0.00	m_1	mutation rate from AD into AI
0.00	0.00	r_2	proliferation rate of AIPC
0.00	0.00	γ_A	androgen turnover rate
0.00	0.00	v	dendritic cells vaccine

(a) Untreated case

LSA	ABS	Parameter	Description
-3.41	3.41	μ_1	death rate of ADPC
0.59	0.59	m_1	mutation rate from AD into AI
-0.45	0.45	γ_A	androgen turnover rate
0.34	0.34	r_2	proliferation rate of AIPC
-0.31	0.31	a_0	baseline level of androgen
0.16	0.16	r_1	proliferation rate of ADPC
0.02	0.02	K	tumor carrying capacity
0.00	0.00	e_{CX}	killing rate of tumor by CTL
0.00	0.00	g_{CX}	CTL saturation level for tumor cells inhibition
0.00	0.00	μ_R	death rate of Treg
0.00	0.00	e_C	activation rate of CTL by dendritic cells
0.00	0.00	k_R	inactivation rate of CTL by Treg
0.00	0.00	a_{IR}	activation rate of Treg by IL-2
0.00	0.00	g_C	dendritic cells saturation level for CTL clonal expansion
0.00	0.00	μ_D	death rate of dendritic cells
0.00	0.00	s_D	source of dendritic cells
0.00	0.00	μ_I	death rate of IL-2
0.00	0.00	e_I	activation rate of IL-2 by CTL and tumor
0.00	0.00	g_I	tumor cells saturation level for CTL stimulation of IL-2
0.00	0.00	a_R	activation rate of Treg by IL-2
0.00	0.00	μ_C	death rate of CTL
0.00	0.00	g_{IC}	IL-2 saturation level for CTL clonal expansion
0.00	0.00	e_{IC}	activation rate of CTL by IL-2
0.00	0.00	k_{ip}	Killing rate of tumor by CTL due to ipilimumab drug
0.00	0.00	I_{p0}	Ipilimumab dose
0.00	0.00	λ_P	degradation rate of ipilimumab
0.00	0.00	v	dendritic cells vaccine

(b) Androgen deprivation therapy

LSA	ABS	Parameter	Description
-3.41	3.41	μ_1	death rate of ADPC
0.59	0.59	m_1	mutation rate from AD into AI
-0.45	0.45	γ_A	androgen turnover rate
0.34	0.34	r_2	proliferation rate of AIPC
-0.31	0.31	a_0	baseline level of androgen
0.16	0.16	r_1	proliferation rate of ADPC
0.02	0.02	K	tumor carrying capacity
0.00	0.00	e_{CX}	killing rate of tumor by CTL
0.00	0.00	g_{CX}	CTL saturation level for tumor cells inhibition
0.00	0.00	μ_R	death rate of Treg
0.00	0.00	e_C	activation rate of CTL by dendritic cells
0.00	0.00	k_R	inactivation rate of CTL by Treg
0.00	0.00	a_{IR}	activation rate of Treg by IL-2
0.00	0.00	g_C	dendritic cells saturation level for CTL clonal expansion
0.00	0.00	μ_D	death rate of dendritic cells
0.00	0.00	s_D	source of dendritic cells
0.00	0.00	v	dendritic cells vaccine
0.00	0.00	μ_I	death rate of IL-2
0.00	0.00	e_I	activation rate of IL-2 by CTL and tumor
0.00	0.00	g_I	tumor cells saturation level for CTL stimulation of IL-2
0.00	0.00	a_R	activation rate of Treg by IL-2
0.00	0.00	μ_C	death rate of CTL
0.00	0.00	g_{IC}	IL-2 saturation level for CTL clonal expansion
0.00	0.00	e_{IC}	activation rate of CTL by IL-2
0.00	0.00	k_{ip}	Killing rate of tumor by CTL due to ipilimumab drug
0.00	0.00	I_{p0}	Ipilimumab dose
0.00	0.00	λ_P	degradation rate of ipilimumab

(c) Androgen deprivation + vaccine therapy

LSA	ABS	Parameter	Description
-3.67	3.67	μ_1	death rate of ADPC
1.70	1.70	λ_P	degradation rate of ipilimumab
-1.40	1.40	k_{ip}	Killing rate of tumor by CTL due to ipilimumab drug
-1.40	1.40	I_{p0}	Ipilimumab dose
0.90	0.90	k_R	inactivation rate of CTL by Treg
-0.90	0.90	e_C	activation rate of CTL by dendritic cells
0.87	0.87	a_{IR}	activation rate of Treg by IL-2
-0.85	0.85	μ_R	death rate of Treg
0.80	0.80	g_C	dendritic cells saturation level for CTL clonal expansion
-0.62	0.62	s_D	source of dendritic cells
0.62	0.62	μ_D	death rate of dendritic cells
-0.59	0.59	γ_A	androgen turnover rate
0.59	0.59	m_1	mutation rate from AD into AI
-0.50	0.50	μ_I	death rate of IL-2
0.49	0.49	e_I	activation rate of IL-2 by CTL and tumor
-0.48	0.48	a_0	baseline level of androgen
0.34	0.34	r_2	proliferation rate of AIPC
-0.34	0.34	g_I	tumor cells saturation level for CTL stimulation of IL-2
0.21	0.21	r_1	proliferation rate of ADPC
0.02	0.02	K	tumor carrying capacity
0.00	0.00	a_R	activation rate of Treg by IL-2
0.00	0.00	e_{CX}	killing rate of tumor by CTL
0.00	0.00	g_{CX}	CTL saturation level for tumor cells inhibition
0.00	0.00	μ_C	death rate of CTL
0.00	0.00	g_{IC}	IL-2 saturation level for CTL clonal expansion
0.00	0.00	e_{IC}	activation rate of CTL by IL-2
0.00	0.00	v	dendritic cells vaccine

(d) Androgen deprivation + anti-CTLA4 therapy

Figure B.1: Local sensitivity analysis oh human PCa model with $t_f = 4$ months. Tables show the LSA values of tumor variable for several treatment conditions. The values are computed by considering the final tumor size, by fixing the simulation time to 4 months.

LSA	ABS	Parameter	Description
1.14	1.14	r_1	proliferation rate of ADPC
0.52	0.52	a_0	baseline level of androgen
0.39	0.39	K	tumor carrying capacity
0.00	0.00	e_{CX}	killing rate of tumor by CTL
0.00	0.00	k_R	inactivation rate of CTL by Treg
0.00	0.00	e_C	activation rate of CTL by dendritic cells
0.00	0.00	a_{IR}	activation rate of Treg by IL-2
0.00	0.00	μ_R	death rate of Treg
0.00	0.00	g_C	dendritic cells saturation level for CTL clonal expansion
0.00	0.00	μ_D	death rate of dendritic cells
0.00	0.00	s_D	source of dendritic cells
0.00	0.00	μ_I	death rate of IL-2
0.00	0.00	e_I	activation rate of IL-2 by CTL and tumor
0.00	0.00	g_{CX}	CTL saturation level for tumor cells inhibition
0.00	0.00	g_I	tumor cells saturation level for CTL stimulation of IL-2
0.00	0.00	a_R	activation rate of Treg by IL-2
0.00	0.00	μ_C	death rate of CTL
0.00	0.00	e_{IC}	activation rate of CTL by IL-2
0.00	0.00	g_{IC}	IL-2 saturation level for CTL clonal expansion
0.00	0.00	k_{IP}	Killing rate of tumor by CTL due to ipilimumab drug
0.00	0.00	I_{p0}	Ipilimumab dose
0.00	0.00	λ_P	degradation rate of ipilimumab
0.00	0.00	μ_1	death rate of ADPC
0.00	0.00	m_1	mutation rate from AD into AI
0.00	0.00	r_2	proliferation rate of AIPC
0.00	0.00	γ_A	androgen turnover rate
0.00	0.00	v	dendritic cells vaccine

(a) Untreated case

LSA	ABS	Parameter	Description
-1.02	1.02	μ_1	death rate of ADPC
0.99	0.99	m_1	mutation rate from AD into AI
0.94	0.94	r_2	proliferation rate of AIPC
0.14	0.14	r_1	proliferation rate of ADPC
-0.08	0.08	γ_A	androgen turnover rate
0.02	0.02	a_0	baseline level of androgen
0.02	0.02	K	tumor carrying capacity
0.00	0.00	e_{CX}	killing rate of tumor by CTL
0.00	0.00	g_{CX}	CTL saturation level for tumor cells inhibition
0.00	0.00	μ_R	death rate of Treg
0.00	0.00	e_C	activation rate of CTL by dendritic cells
0.00	0.00	k_R	inactivation rate of CTL by Treg
0.00	0.00	a_{IR}	activation rate of Treg by IL-2
0.00	0.00	g_C	dendritic cells saturation level for CTL clonal expansion
0.00	0.00	μ_D	death rate of dendritic cells
0.00	0.00	s_D	source of dendritic cells
0.00	0.00	μ_I	death rate of IL-2
0.00	0.00	e_I	activation rate of IL-2 by CTL and tumor
0.00	0.00	g_I	tumor cells saturation level for CTL stimulation of IL-2
0.00	0.00	a_R	activation rate of Treg by IL-2
0.00	0.00	μ_C	death rate of CTL
0.00	0.00	e_{IC}	activation rate of CTL by IL-2
0.00	0.00	g_{IC}	IL-2 saturation level for CTL clonal expansion
0.00	0.00	k_{IP}	Killing rate of tumor by CTL due to ipilimumab drug
0.00	0.00	I_{p0}	Ipilimumab dose
0.00	0.00	λ_P	degradation rate of ipilimumab
0.00	0.00	v	dendritic cells vaccine

(b) Androgen deprivation therapy

LSA	ABS	Parameter	Description
-1.02	1.02	μ_1	death rate of ADPC
0.99	0.99	m_1	mutation rate from AD into AI
0.94	0.94	r_2	proliferation rate of AIPC
0.14	0.14	r_1	proliferation rate of ADPC
-0.08	0.08	γ_A	androgen turnover rate
0.02	0.02	a_0	baseline level of androgen
0.02	0.02	K	tumor carrying capacity
0.00	0.00	e_{CX}	killing rate of tumor by CTL
0.00	0.00	g_{CX}	CTL saturation level for tumor cells inhibition
0.00	0.00	μ_R	death rate of Treg
0.00	0.00	e_C	activation rate of CTL by dendritic cells
0.00	0.00	k_R	inactivation rate of CTL by Treg
0.00	0.00	a_{IR}	activation rate of Treg by IL-2
0.00	0.00	g_C	dendritic cells saturation level for CTL clonal expansion
0.00	0.00	μ_D	death rate of dendritic cells
0.00	0.00	s_D	source of dendritic cells
0.00	0.00	v	dendritic cells vaccine
0.00	0.00	μ_I	death rate of IL-2
0.00	0.00	e_I	activation rate of IL-2 by CTL and tumor
0.00	0.00	g_I	tumor cells saturation level for CTL stimulation of IL-2
0.00	0.00	a_R	activation rate of Treg by IL-2
0.00	0.00	μ_C	death rate of CTL
0.00	0.00	e_{IC}	activation rate of CTL by IL-2
0.00	0.00	g_{IC}	IL-2 saturation level for CTL clonal expansion
0.00	0.00	k_{IP}	Killing rate of tumor by CTL due to ipilimumab drug
0.00	0.00	I_{p0}	Ipilimumab dose
0.00	0.00	λ_P	degradation rate of ipilimumab

(c) Androgen deprivation + vaccine therapy

LSA	ABS	Parameter	Description
1.73	1.73	λ_P	degradation rate of ipilimumab
-1.40	1.40	I_{p0}	Ipilimumab dose
-1.40	1.40	k_{IP}	Killing rate of tumor by CTL due to ipilimumab drug
-1.29	1.29	μ_1	death rate of ADPC
0.99	0.99	m_1	mutation rate from AD into AI
0.94	0.94	r_2	proliferation rate of AIPC
0.91	0.91	k_R	inactivation rate of CTL by Treg
-0.90	0.90	e_C	activation rate of CTL by dendritic cells
0.88	0.88	a_{IR}	activation rate of Treg by IL-2
-0.85	0.85	μ_R	death rate of Treg
0.81	0.81	g_C	dendritic cells saturation level for CTL clonal expansion
-0.62	0.62	s_D	source of dendritic cells
0.62	0.62	μ_D	death rate of dendritic cells
-0.50	0.50	μ_I	death rate of IL-2
0.49	0.49	e_I	activation rate of IL-2 by CTL and tumor
-0.34	0.34	g_I	tumor cells saturation level for CTL stimulation of IL-2
-0.22	0.22	γ_A	androgen turnover rate
0.19	0.19	r_1	proliferation rate of ADPC
-0.15	0.15	a_0	baseline level of androgen
0.02	0.02	K	tumor carrying capacity
0.00	0.00	a_R	activation rate of Treg by IL-2
0.00	0.00	e_{CX}	killing rate of tumor by CTL
0.00	0.00	g_{CX}	CTL saturation level for tumor cells inhibition
0.00	0.00	μ_C	death rate of CTL
0.00	0.00	g_{IC}	IL-2 saturation level for CTL clonal expansion
0.00	0.00	e_{IC}	activation rate of CTL by IL-2
0.00	0.00	v	dendritic cells vaccine

(d) Androgen deprivation + anti-CTLA4 therapy

Figure B.2: Local sensitivity analysis oh human PCa model with $t_f = 6$ months. Tables show the LSA values of tumor variable for several treatment conditions. The values are computed by considering the final tumor size, by fixing the simulation time to 6 months.

Bibliography

[1] J. D. Murray. *Mathematical Biology.* Springer Berlin Heidelberg, 1989. doi: 10.1007/978-3-662-08542-4.

[2] N Bellomo, N K Li, and P K Maini. On the foundations of cancer modelling: selected topics, speculations and perspectives. *Mathematical Models and Methods in Applied Sciences*, 18 (04):593–646, 2008. doi: 10.1142/S0218202508002796.

[3] Raluca Eftimie, Jonathan L Bramson, and David J D Earn. Interactions Between the Immune System and Cancer: A Brief Review of Non-spatial Mathematical Models. *Bulletin of Mathematical Biology*, 73(1):2–32, 2011. ISSN 1522-9602. doi: 10.1007/s11538-010-9526-3.

[4] Thomas Hillen and Mark A Lewis. Mathematical Ecology of Cancer. In Marcello Delitala and Giulia Ajmone Marsan, editors, *Managing Complexity, Reducing Perplexity.*, pages 1–13, Cham, 2014. Springer International Publishing. ISBN 978-3-319-03759-2. doi: 10.1007/978-3-319-03759-2_1.

[5] Karla Misselbeck, Luca Marchetti, Martha S Field, Marco Scotti, Corrado Priami, and Patrick J Stover. A hybrid stochastic model of folate-mediated one-carbon metabolism: Effect of the common C677T MTHFR variant on de novo thymidylate biosynthesis. *Scientific Reports*, 7(1):797, 2017. ISSN 2045-2322. doi: 10.1038/s41598-017-00854-w.

[6] Abdallah K Alameddine, Frederick Conlin, and Brian Binnall. An Introduction to the Mathematical Modeling in the Study of Cancer Systems Biology. *Cancer informatics*, 17: 1176935118799754, 2018. ISSN 1176-9351 (Print). doi: 10.1177/1176935118799754.

[7] Cansu Uluseker, Giulia Simoni, Luca Marchetti, Marco Dauriz, Alice Matone, and Corrado Priami. A closed-loop multi-level model of glucose homeostasis. *PLOS ONE*, 13(2):1–23, 2018. doi: 10.1371/journal.pone.0190627.

[8] Karla Misselbeck, Luca Marchetti, Corrado Priami, Patrick J Stover, and Martha S Field. The 5-formyltetrahydrofolate futile cycle reduces pathway stochasticity in an extended hybrid-stochastic model of folate-mediated one-carbon metabolism. *Scientific Reports*, 9 (1):4322, 2019. ISSN 2045-2322. doi: 10.1038/s41598-019-40230-4.

[9] Luca Marchetti, Federico Reali, Marco Dauriz, Corinna Brangani, Linda Boselli, Giulia Ceradini, Enzo Bonora, Riccardo C Bonadonna, and Corrado Priami. A Novel Insulin/Glucose Model after a Mixed-Meal Test in Patients with Type 1 Diabetes on Insulin Pump Therapy. *Scientific Reports*, 6:36029, nov 2016. doi: 10.1038/srep36029.

[10] Luca Marchetti, Corrado Priami, and Vo Hong Thanh. *Simulation Algorithms for Computational Systems Biology*. Springer International Publishing, 1 edition, 2017. ISBN 978-3-319-63113-4. doi: 10.1007/978-3-319-63113-4.

[11] Giulia Simoni, Hong Thanh Vo, Corrado Priami, and Luca Marchetti. A comparison of deterministic and stochastic approaches for sensitivity analysis in computational systems biology. *Briefings in Bioinformatics*, 2019. ISSN 1477-4054. doi: 10.1093/bib/bbz014.

[12] Giulia Simoni, Federico Reali, Corrado Priami, and Luca Marchetti. Stochastic simulation algorithms for computational systems biology: Exact, approximate, and hybrid methods. *Wiley Interdisciplinary Reviews: Systems Biology and Medicine*, 11(6):e1459, 2019. doi: 10.1002/wsbm.1459.

[13] Federico Reali, Corrado Priami, and Luca Marchetti. Optimization Algorithms for Computational Systems Biology. *Frontiers in Applied Mathematics and Statistics*, 3:6, 2017. ISSN 2297-4687. doi: 10.3389/fams.2017.00006.

[14] Angela M Jarrett, Ernesto A B F Lima, David A Hormuth II, Matthew T McKenna, Xinzeng Feng, David A Ekrut, Anna Claudia M Resende, Amy Brock, and Thomas E Yankeelov. Mathematical models of tumor cell proliferation: A review of the literature. *Expert Review of Anticancer Therapy*, 18(12):1271–1286, 2018. doi: 10.1080/14737140.2018.1527689.

[15] Elena Piretto, Marcello Delitala, and Mario Ferraro. Combination therapies and intratumoral competition: Insights from mathematical modeling. *Journal of Theoretical Biology*, 446:149–159, 2018. ISSN 0022-5193. doi: 10.1016/j.jtbi.2018.03.014.

[16] John Metzcar, Yafei Wang, Randy Heiland, and Paul Macklin. A Review of Cell-Based Computational Modeling in Cancer Biology. *JCO Clinical Cancer Informatics*, 3:1–13, 2019. doi: 10.1200/CCI.18.00069.

[17] Sofia Farkona, Eleftherios P Diamandis, and Ivan M Blasutig. Cancer immunotherapy: The beginning of the end of cancer? *BMC Medicine*, 14(1):1–18, 2016. ISSN 17417015. doi: 10.1186/s12916-016-0623-5.

[18] Daniel S Chen and Ira Mellman. Oncology Meets Immunology: The Cancer-Immunity Cycle. *Immunity*, 39(1):1–10, 2013. ISSN 1074-7613. doi: https://doi.org/10.1016/j.immuni.2013.07.012.

[19] Rachel S Riley, Carl H June, Robert Langer, and Michael J Mitchell. Delivery technologies for cancer immunotherapy. *Nature Reviews Drug Discovery*, 18(3):175–196, 2019. ISSN 1474-1784. doi: 10.1038/s41573-018-0006-z.

[20] Alberto D'Onofrio. Metamodeling tumor–immune system interaction, tumor evasion and immunotherapy. *Mathematical and Computer Modelling*, 47(5):614–637, 2008. ISSN 0895-7177. doi: https://doi.org/10.1016/j.mcm.2007.02.032.

[21] Lisette de Pillis, Trevor Caldwell, Elizabeth Sarapata, and Heather Williams. Mathematical modeling of regulatory T cell effects on renal cell carcinoma treatment. *Discrete and Continuous Dynamical Systems - Series B*, 18:915–943, 2013. doi: 10.3934/dcdsb.2013.18.915.

[22] Siddhartha P Chakrabarty and Floyd B Hanson. Distributed parameters deterministic model for treatment of brain tumors using Galerkin finite element method. *Mathematical Biosciences*, 219(2):129–141, 2009. ISSN 00255564. doi: 10.1016/j.mbs.2009.03.005.

[23] Huiming Peng, Weiling Zhao, Hua Tan, Zhiwei Ji, Jingsong Li, King Li, and Xiaobo Zhou. Prediction of treatment efficacy for prostate cancer using a mathematical model. *Scientific Reports*, 6:21599, feb 2016. doi: 10.1038/srep21599.

[24] Erica M Rutter and Yang Kuang. Global dynamics of a model of joint hormone treatment with dendritic cell vaccine for prostate cancer. *Discrete and Continuous Dynamical Systems - Series B*, 22(3):1001–1021, 2017. ISSN 1531-3492. doi: 10.3934/dcdsb.2017050.

[25] Denise Kirschner and John Carl Panetta. Modeling immunotherapy of the tumor – immune interaction. *Journal of Mathematical Biology*, 37(3):235–252, sep 1998. ISSN 1432-1416. doi: 10.1007/s002850050127.

[26] Lisette de Pillis, K. Renee Fister, Weiqing Gu, Craig Collins, Michael Daub, David Gross, James Moore, and Benjamin Preskill. Mathematical model creation for cancer chemo-immunotherapy. *Computational and Mathematical Methods in Medicine*, 10(3):165–184, 2009. ISSN 1748670X. doi: 10.1080/17486700802216301.

[27] L G de Pillis, W Gu, and A E Radunskaya. Mixed immunotherapy and chemotherapy of tumors: modeling, applications and biological interpretations. *Journal of Theoretical Biology*, 238(4):841–862, 2006. ISSN 0022-5193. doi: https://doi.org/10.1016/j.jtbi.2005.06.037.

[28] Badal Joshi, Xueying Wang, Sayanti Banerjee, Haiyan Tian, Anastasios Matzavinos, and Mark A J Chaplain. On immunotherapies and cancer vaccination protocols: A mathe-

matical modelling approach. *Journal of Theoretical Biology*, 259(4):820–827, 2009. ISSN 00225193. doi: 10.1016/j.jtbi.2009.05.001.

[29] Khaphetsi Joseph Mahasa, Rachid Ouifki, Amina Eladdadi, and Lisette de Pillis. Mathematical model of tumor–immune surveillance. *Journal of Theoretical Biology*, 404:312–330, 2016. ISSN 10958541. doi: 10.1016/j.jtbi.2016.06.012.

[30] F Castiglione and B Piccoli. Cancer immunotherapy, mathematical modeling and optimal control. *Journal of Theoretical Biology*, 247(4):723–732, 2007. ISSN 00225193. doi: 10.1016/j.jtbi.2007.04.003.

[31] Luis Soto-Ortiz. A cancer treatment based on synergy between anti-angiogenic and immune cell therapies. *Journal of Theoretical Biology*, 394:197–211, 2016. ISSN 10958541. doi: 10.1016/j.jtbi.2016.01.026.

[32] Xiulan Lai and Avner Friedman. Combination therapy of cancer with cancer vaccine and immune checkpoint inhibitors: A mathematical model. *PLoS ONE*, 12(5):1–24, 2017. ISSN 19326203. doi: 10.1371/journal.pone.0178479.

[33] Milad Qomlaqi, Fariba Bahrami, Maryam Ajami, and Jamshid Hajati. An extended mathematical model of tumor growth and its interaction with the immune system, to be used for developing an optimized immunotherapy treatment protocol. *Mathematical Biosciences*, 292:1–9, 2017. ISSN 0025-5564. doi: https://doi.org/10.1016/j.mbs.2017.07.006.

[34] Aylin Sertkaya, Hui Hsing Wong, Amber Jessup, and Trinidad Beleche. Key cost drivers of pharmaceutical clinical trials in the United States. *Clinical Trials*, 13(2):117–126, 2016. ISSN 17407753. doi: 10.1177/1740774515625964.

[35] Francis S Collins and Harold Varmus. A New Initiative on Precision Medicine. *New England Journal of Medicine*, 372(9):793–795, 2015. doi: 10.1056/NEJMp1500523. URL `https://doi.org/10.1056/NEJMp1500523`.

[36] Euan A Ashley. The Precision Medicine Initiative: A New National Effort. *JAMA*, 313 (21):2119–2120, 2015. ISSN 0098-7484. doi: 10.1001/jama.2015.3595. URL `https://doi.org/10.1001/jama.2015.3595`.

[37] K Gadkar, D C Kirouac, D E Mager, P H Van Der Graaf, and S Ramanujan. A six-stage workflow for robust application of systems pharmacology. *CPT: Pharmacometrics and Systems Pharmacology*, 5(5):235–249, 2016. ISSN 21638306. doi: 10.1002/psp4.12071.

[38] O. Demin, T. Karelina, D. Svetlichniy, E. Metelkin, G. Speshilov, O. Demin, D. Fairman, Ph Van Der Graaf, and B. M. Agoram. Systems pharmacology models can be used to understandcomplex pharmacokinetic-pharmacodynamic behavior: An example using 5-lipoxygenase inhibitors. *CPT: Pharmacometrics and Systems Pharmacology*, 2(9), 2013. ISSN 21638306. doi: 10.1038/psp.2013.49.

[39] Peter K Sorger, Sandra R B Allerheiligen, Russ B Altmann, Brian Shoichet, Douglas a Lauffenburger, Ravi Iyengar, and Andrea Califano. Quantitative and systems pharmacology in the postgenomic era: New approaches to discovering drugs and understanding therapeutic mechanisms. *QSP White Paper*, pages 1–48, 2011.

[40] Andrew M. Stern, Mark E. Schurdak, Ivet Bahar, Jeremy M. Berg, and D. Lansing Taylor. A Perspective on Implementing a Quantitative Systems Pharmacology Platform for Drug Discovery and the Advancement of Personalized Medicine. *Journal of Biomolecular Screening*, 21(6):521–534, 2016. ISSN 1552454X. doi: 10.1177/1087057116635818.

[41] K Gadkar, D Kirouac, N Parrott, and S Ramanujan. Quantitative systems pharmacology: a promising approach for translational pharmacology. *Drug Discovery Today: Technologies*, 21-22(Ldl):57–65, 2016. ISSN 17406749. doi: 10.1016/j.ddtec.2016.11.001.

[42] C M Friedrich. A model qualification method for mechanistic physiological QSP models to support model-informed drug development. *CPT: Pharmacometrics and Systems Pharmacology*, 5(2):43–53, 2016. ISSN 21638306. doi: 10.1002/psp4.12056.

[43] Chanchala Kaddi, Federico Reali, Luca Marchetti, Bradley Niesner, Silvia Parolo, Giulia Simoni, Susana Zaph, Mengdi Tao, Ruth E Abrams, Zachary van Rijn, John P Leonard, M Judith Peterschmitt, Ana Cristina Puga, Kevin C Mange, Jeffrey S Barrett, Corrado Priami, Edward H Schuchman, and Karim Azer. Integrated quantitative systems pharmacology (QSP) model of lysosomal diseases provides an innovative computational platform to support research and therapeutic development for the sphingolipidoses. *Molecular Genetics and Metabolism*, 123(2):S73–S74, 2018. doi: 10.1016/j.ymgme.2017.12.183.

[44] Harold Evelyn Taitt. Global Trends and Prostate Cancer: A Review of Incidence, Detection, and Mortality as Influenced by Race, Ethnicity, and Geographic Location. *American Journal of Men's Health*, 12(6):1807–1823, 2018. doi: 10.1177/1557988318798279.

[45] Rebecca L Siegel, Kimberly D Miller, and Ahmedin Jemal. Cancer statistics, 2019. *CA: A Cancer Journal for Clinicians*, 69(1):7–34, 2019. doi: 10.3322/caac.21551.

[46] Kimberly D Miller, Leticia Nogueira, Angela B Mariotto, Julia H Rowland, K Robin Yabroff, Catherine M Alfano, Ahmedin Jemal, Joan L Kramer, and Rebecca L Siegel. Cancer treatment and survivorship statistics, 2019. *CA: A Cancer Journal for Clinicians*, 2019. doi: 10.3322/caac.21565.

[47] Freddie C Hamdy, Jenny L Donovan, J Athene Lane, Malcolm Mason, Chris Metcalfe, Peter Holding, Michael Davis, Tim J Peters, Emma L Turner, Richard M Martin, Jon Oxley, Mary Robinson, John Staffurth, Eleanor Walsh, Prasad Bollina, James Catto, Andrew Doble, Alan Doherty, David Gillatt, Roger Kockelbergh, Howard Kynaston, Alan Paul, Philip Powell, Stephen Prescott, Derek J Rosario, Edward Rowe, and David E Neal. 10-Year Outcomes after Monitoring, Surgery, or Radiotherapy for Localized Prostate Cancer. *New England Journal of Medicine*, 375(15):1415–1424, 2016. doi: 10.1056/NEJMoa1606220.

[48] GERALD Hull, FARHANG Rabbani, FARHAT Abbas, THOMAS Wheeler, MICHAEL Kattan, and PETER Scardino. Cancer control with radical prostatectomy alone in 1,000

consecutive patients. *The Journal of Urology*, 167(2):528–534, 2002. doi: 10.1097/00005392-200202000-00018.

[49] Kimberly A Roehl, Misop Han, Christian G Ramos, Joannv Antenor, and William J CATALONA. Cancer progression and survival rates following anatomical radical retropubic prostatectomy in 3,478 consecutive patients: long-term results. *Journal of Urology*, 172(3): 910–914, 2004. doi: 10.1097/01.ju.0000134888.22332.bb.

[50] Andrew J Stephenson, Peter T Scardino, James A Eastham, Jr. Bianco Fernando J., Zohar A Dotan, Paul A Fearn, and Michael W Kattan. Preoperative Nomogram Predicting the 10-Year Probability of Prostate Cancer Recurrence After Radical Prostatectomy. *JNCI: Journal of the National Cancer Institute*, 98(10):715–717, 2006. ISSN 0027-8874. doi: 10.1093/jnci/djj190.

[51] Semini Sumanasuriya and Johann De Bono. Treatment of Advanced Prostate Cancer - A Review of Current Therapies and Future Promise. *Cold Spring Harbor Perspectives in Medicine*, 2017. doi: 10.1101/cshperspect.a030635.

[52] Brian J Feldman and David Feldman. The development of androgen-independent prostate cancer. *Nature Reviews Cancer*, 1(1):34–45, 2001. ISSN 1474-1768. doi: 10.1038/35094009.

[53] Philip A Watson, Vivek K Arora, and Charles L Sawyers. Emerging mechanisms of resistance to androgen receptor inhibitors in prostate cancer. *Nature Reviews Cancer*, 15:701, nov 2015. doi: 10.1038/nrc4016.

[54] Giuseppe Di Lorenzo, Carlo Buonerba, and Philip W Kantoff. Immunotherapy for the treatment of prostate cancer. *Nature Reviews Clinical Oncology*, 8(9):551–561, 2011. ISSN 1759-4782. doi: 10.1038/nrclinonc.2011.72.

[55] Patrick W K Lee and Shashi Gujar. Potentiating prostate cancer immunotherapy with oncolytic viruses. *Nature Reviews Urology*, 15:235–250, 2018. doi: 10.1038/nrurol.2018.10.

[56] Nicholas J Venturini and Charles G Drake. Immunotherapy for Prostate Cancer. *Cold Spring Harbor Perspectives in Medicine*, 9(5), 2019. doi: 10.1101/cshperspect.a030627.

[57] Adeline N Boettcher, Ahmed Usman, Alicia Morgans, David J VanderWeele, Jeffrey Sosman, and Jennifer D Wu. Past, Current, and Future of Immunotherapies for Prostate Cancer. *Frontiers in Oncology*, 9:884, 2019. ISSN 2234-943X. doi: 10.3389/fonc.2019.00884.

[58] Yukiko Kiniwa, Yoshihiro Miyahara, Helen Y Wang, Weiyi Peng, Guangyong Peng, Thomas M Wheeler, Timothy C Thompson, Lloyd J Old, and Rong-Fu Wang. CD8+ Foxp3+ Regulatory T Cells Mediate Immunosuppression in Prostate Cancer, 2007.

[59] Ira Mellman, George Coukos, and Glenn Dranoff. Cancer immunotherapy comes of age. *Nature*, 480:480, dec 2011. doi: 10.1038/nature10673.

[60] Antoni Ribas and Jedd D Wolchok. Cancer immunotherapy using checkpoint blockade. *Science*, 359(6382):1350–1355, 2018. ISSN 0036-8075. doi: 10.1126/science.aar4060.

[61] Paul Andrew Antony and Nicholas P Restifo. CD4+CD25+ T regulatory cells, immunotherapy of cancer, and interleukin-2. *Journal of immunotherapy (Hagerstown, Md. : 1997)*, 28 (2):120–128, 2005. ISSN 1524-9557 (Print). doi: 10.1097/01.cji.0000155049.26787.45.

[62] Ilaria Marigo, Luigi Dolcetti, Paolo Serafini, Paola Zanovello, and Vincenzo Bronte. Tumor-induced tolerance and immune suppression by myeloid derived suppressor cells. *Immunological Reviews*, 222(1):162–179, 2008. doi: 10.1111/j.1600-065X.2008.00602.x.

[63] Dmitry I. Gabrilovich and Srinivas Nagaraj. Myeloid-derived suppressor cells as regulators of the immune system. *Nature Reviews Immunology*, 9:162, 2009. doi: 10.1038/nri2506.

[64] Guocan Wang, Xin Lu, Prasenjit Dey, Pingna Deng, Chia Chin Wu, Shan Jiang, Zhuangna Fang, Kun Zhao, Ramakrishna Konaparthi, Sujun Hua, Jianhua Zhang, Elsa M Li-Ning-Tapia, Avnish Kapoor, Chang-Jiun Wu, Neelay Bhaskar Patel, Zhenglin Guo, Vandhana Ramamoorthy, Trang N Tieu, Tim Heffernan, Di Zhao, Xiaoying Shang, Sunada Khadka,

Pingping Hou, Baoli Hu, Eun-Jung Jin, Wantong Yao, Xiaolu Pan, Zhihu Ding, Yanxia Shi, Liren Li, Qing Chang, Patricia Troncoso, Christopher J Logothetis, Mark J McArthur, Lynda Chin, Y Alan Wang, and Ronald A DePinho. Targeting YAP-Dependent MDSC Infiltration Impairs Tumor Progression. *Cancer discovery*, 6(1):80–95, jan 2016. ISSN 2159-8290 (Electronic). doi: 10.1158/2159-8290.CD-15-0224.

[65] Walter Kolch, Dirk Fey, Colm J Ryan, Iman Tavassoly, Joseph Goldfarb, and Ravi Iyengar. Systems biology primer: the basic methods and approaches. *Essays in Biochemistry*, 62 (4):487–500, 2018. ISSN 0071-1365. doi: 10.1042/EBC20180003. URL `https://doi.org/10.1042/EBC20180003`.

[66] Anthony Trewavas. A Brief History of Systems Biology. *The Plant Cell*, 18(10):2420–2430, 2006. ISSN 1040-4651. doi: 10.1105/tpc.106.042267.

[67] Rachel A Hillmer. Systems Biology for Biologists. *PLOS Pathogens*, 11(5):1–6, 2015. doi: 10.1371/journal.ppat.1004786.

[68] Rachel A Gottschalk, Andrew J Martins, Virginie Sjoelund, Bastian R Angermann, Bin Lin, and Ronald N Germain. Recent progress using systems biology approaches to better understand molecular mechanisms of immunity. *Seminars in immunology*, 25(3):201–208, oct 2013. ISSN 1044-5323. doi: 10.1016/j.smim.2012.11.002.

[69] Lisa M Pham, Luis Carvalho, Scott Schaus, and Eric D Kolaczyk. Perturbation Detection Through Modeling of Gene Expression on a Latent Biological Pathway Network: A Bayesian Hierarchical Approach. *Journal of the American Statistical Association*, 111(513):73–92, 2016. doi: 10.1080/01621459.2015.1110523.

[70] Thomas Lemberger. Systems biology in human health and disease. *Molecular Systems Biology*, 3:136, 2007. ISSN 1744-4292. doi: 10.1038/msb4100175. URL `https://europepmc.org/articles/PMC2013921`.

[71] Evan J Molinelli, Anil Korkut, Weiqing Wang, Martin L Miller, Nicholas P Gauthier, Xiaohong Jing, Poorvi Kaushik, Qin He, Gordon Mills, David B Solit, Christine A Pratilas, Martin Weigt, Alfredo Braunstein, Andrea Pagnani, Riccardo Zecchina, and Chris Sander. Perturbation Biology: Inferring Signaling Networks in Cellular Systems. *PLOS Computational Biology*, 9(12):1–23, 2013. doi: 10.1371/journal.pcbi.1003290. URL `https://doi.org/10.1371/journal.pcbi.1003290`.

[72] Brian P. Ingalls. *Mathematical Modeling in Systems Biology: An Introduction*. Cambridge, Massachusetts : MIT Press, 2013.

[73] Philippe Renard, Andres Alcolea, and David Ginsbourger. *Stochastic versus Deterministic Approaches*, chapter 8, pages 133–149. John Wiley & Sons, Ltd, 2013. ISBN 9781118351475. doi: 10.1002/9781118351475.ch8. URL `https://onlinelibrary.wiley.com/doi/abs/10.1002/9781118351475.ch8`.

[74] Stephen Wiggins. *Introduction To Applied Nonlinear Dynamical Systems And Chaos*, volume 4. Springer Verlag, 2nd edition, 2003. doi: 10.1007/b97481.

[75] Lawrence Perko. *Differential Equations and Dynamical Systems*. Springer-Verlag New York, 3 edition, 2001. doi: 10.1007/978-1-4613-0003-8.

[76] Mimmo Iannelli and Andrea Pugliese. *Basic theory of Ordinary Differential Equations*, pages 295–314. Springer International Publishing, Cham, 2014. ISBN 978-3-319-03026-5. doi: 10.1007/978-3-319-03026-5_10. URL `https://doi.org/10.1007/978-3-319-03026-5{_}10`.

[77] A. Dhooge, W. Govaerts, and Yu. A. Kuznetsov. MATCONT: A MATLAB Package for Numerical Bifurcation Analysis of ODEs. *ACM Transaction Mathematical Software*, 29(2):141–164, 2003. doi: 10.1145/779359.779362.

[78] Panos Pardalos and H Romeijn. *Handbook of Global Optimization*. Springer, 2002. doi: 10.1007/978-1-4757-5362-2.

[79] Julio R Banga. Optimization in computational systems biology. *BMC Systems Biology*, 2 (1):47, 2008. ISSN 1752-0509. doi: 10.1186/1752-0509-2-47. URL https://doi.org/10.1186/1752-0509-2-47.

[80] Mohd Nadhir Ab Wahab, Samia Nefti-Meziani, and Adham Atyabi. A comprehensive review of swarm optimization algorithms. *PloS one*, 10(5):e0122827, 2015. ISSN 1932-6203 (Electronic). doi: 10.1371/journal.pone.0122827.

[81] Fevrier Valdez, Patricia Melin, and Oscar Castillo. A survey on nature-inspired optimization algorithms with fuzzy logic for dynamic parameter adaptation. *Expert Systems with Applications*, 41(14):6459–6466, 2014. ISSN 0957-4174. doi: https://doi.org/10.1016/j.eswa.2014.04.015. URL http://www.sciencedirect.com/science/article/pii/S0957417414002127.

[82] Sebastian Ruder. An overview of gradient descent optimization algorithms. *ArXiv*, 2016.

[83] R Bellman and K J Åström. On structural identifiability. *Mathematical Biosciences*, 7(3): 329–339, 1970. ISSN 0025-5564. doi: https://doi.org/10.1016/0025-5564(70)90132-X.

[84] Oana Chiş, Julio R Banga, and Eva Balsa-Canto. GenSSI: a software toolbox for structural identifiability analysis of biological models. *Bioinformatics (Oxford, England)*, 27(18):2610–2611, sep 2011. ISSN 1367-4811 (Electronic). doi: 10.1093/bioinformatics/btr431.

[85] Oana Chiş, Julio R Banga, and Eva Balsa-Canto. GenSSI: generating series approach for testing structural identifiability - USER GUIDE, 2011.

[86] Z Zi. Sensitivity analysis approaches applied to systems biology models. *IET Systems Biology*, 5(6):336–346(10), nov 2011. ISSN 1751-8849. URL https://digital-library.theiet.org/content/journals/10.1049/iet-syb.2011.0015.

[87] H Wei, M A. Nearing, and J J. Stone. A Comprehensive Sensitivity Analysis Framework for Model Evaluation and Improvement Using a Case Study of the Rangeland Hydrology

and Erosion Model. *Transactions of the ASABE*, 50(3):945–953, 2007. ISSN 2151-0032. doi: https://doi.org/10.13031/2013.23159.

[88] Elizabeth J Akins, Miranda L Moore, Shuai Tang, Mark C Willingham, Janet A Tooze, and Purnima Dubey. In situ Vaccination Combined with Androgen Ablation and Regulatory T-Cell Depletion Reduces Castration-Resistant Tumor Burden in Prostate-Specific Pten Knockout Mice. *Cancer Research*, 70(9):3473 LP – 3482, may 2010. doi: 10.1158/0008-5472.CAN-09-2490.

[89] Shuai Tang, Miranda L Moore, Jason M Grayson, and Purnima Dubey. Increased CD8+ T-cell Function following Castration and Immunization Is Countered by Parallel Expansion of Regulatory T Cells. *Cancer Research*, 72(8):1975–1985, 2012. ISSN 0008-5472. doi: 10.1158/0008-5472.CAN-11-2499.

[90] Natasha Vitkin, Sarah Nersesian, David Robert Siemens, and Madhuri Koti. The Tumor Immune Contexture of Prostate Cancer. *Frontiers in Immunology*, 10:603, 2019. ISSN 1664-3224. doi: 10.3389/fimmu.2019.00603.

[91] Shin Jen Lin, Fu Ju Chou, Lei Li, Chang Yi Lin, Shuyuan Yeh, and Chawnshang Chang. Natural killer cells suppress enzalutamide resistance and cell invasion in the castration resistant prostate cancer via targeting the androgen receptor splicing variant 7 (ARv7). *Cancer Letters*, 398:62–69, 2017. ISSN 18727980. doi: 10.1016/j.canlet.2017.03.035. URL `http://dx.doi.org/10.1016/j.canlet.2017.03.035`.

[92] Alejandro J Garcia, Marcus Ruscetti, Teresita L Arenzana, Linh M Tran, Daniella Bianci-Frias, Elysia Sybert, Saul J Priceman, Lily Wu, Peter S Nelson, Stephen T Smale, and Hong Wu. Pten Null Prostate Epithelium Promotes Localized Myeloid-Derived Suppressor Cell Expansion and Immune Suppression during Tumor Initiation and Progression. *Molecular and Cellular Biology*, 34(11):2017–2028, 2014. ISSN 0270-7306. doi: 10.1128/MCB.00090-14.

[93] Xin Lu, James W Horner, Erin Paul, Xiaoying Shang, Patricia Troncoso, Pingna Deng, Shan Jiang, Qing Chang, Denise J Spring, Padmanee Sharma, John A Zebala, Dean Y Maeda, Y Alan Wang, and Ronald A DePinho. Effective combinatorial immunotherapy for castration-resistant prostate cancer. *Nature*, 543:728, mar 2017. doi: 10.1038/nature21676.

[94] Elysia C Saputra, Lu Huang, Yihui Chen, and Lisa Tucker-Kellogg. Combination Therapy and the Evolution of Resistance: The Theoretical Merits of Synergism and Antagonism in Cancer. *Cancer Research*, 2018. ISSN 0008-5472. doi: 10.1158/0008-5472.CAN-17-1201.

[95] Anna Domogala, J Alejandro Madrigal, and Aurore Saudemont. Natural Killer Cell Immunotherapy: From Bench to Bedside. *Frontiers in Immunology*, 6:264, 2015. ISSN 1664-3224. doi: 10.3389/fimmu.2015.00264.

[96] Drew M Pardoll. The blockade of immune checkpoints in cancer immunotherapy. *Nature Reviews Cancer*, 12(4):252–264, 2012. ISSN 1474-1768. doi: 10.1038/nrc3239.

[97] Piotr Trzonkowski, Ewa Szmit, Jolanta Myśliwska, Anita Dobyszuk, and Andrzej Myśliwski. CD4 +CD25 + T regulatory cells inhibit cytotoxic activity of T CD8 + and NK lymphocytes in the direct cell-to-cell interaction. *Clinical Immunology*, 112(3):258–267, 2004. ISSN 15216616. doi: 10.1016/j.clim.2004.04.003.

[98] Shimon Sakaguchi, Kajsa Wing, Yasushi Onishi, Paz Prieto-Martin, and Tomoyuki Yamaguchi. Regulatory T cells: how do they suppress immune responses? *International Immunology*, 21(10):1105–1111, 2009. doi: 10.1093/intimm/dxp095.

[99] Nicholas Mitsiades. A Road Map to Comprehensive Androgen Receptor Axis Targeting for Castration-Resistant Prostate Cancer. *Cancer Research*, 73(15):4599–4605, 2013. ISSN 0008-5472. doi: 10.1158/0008-5472.CAN-12-4414.

[100] The Jackson Laboratory. BODY WEIGHT INFORMATION FOR DBA/2J (000671), JAX Mice Strain - DBA/2J. *https://www.jax.org/jax-mice-and-services/strain-data-sheet-pages/body-weight-chart-000671*, 2019.

[101] The Jackson Laboratory. BODY WEIGHT INFORMATION FOR C57BL/6J (000664), JAX Mice Strain - C57BL/6J. *https://www.jax.org/jax-mice-and-services/strain-data-sheet-pages/body-weight-chart-000664*, 2019.

[102] R. T. Costello L. Farnault, C. Sanchez, C. Baier T. Le Treut. Hematological Malignancies Escape from NK Cell Innate Immune Surveillance: Mechanisms and Therapeutic Implications. *Clinical and Developmental Immunology*, 2012, 2012. doi: 10.1155/2012/421702.

[103] Christine Pasero, Gwenaëlle Gravis, Mathilde Guerin, Samuel Granjeaud, Jeanne Thomassin-Piana, Palma Rocchi, Maria Paciencia-Gros, Flora Poizat, Mélanie Bentobji, Francine Azario-Cheillan, Jochen Walz, Naji Salem, Serge Brunelle, Alessandro Moretta, and Daniel Olive. Inherent and Tumor-Driven Immune Tolerance in the Prostate Microenvironment Impairs Natural Killer Cell Antitumor Activity. *Cancer Research*, 76(8): 2153–2165, 2016. ISSN 0008-5472. doi: 10.1158/0008-5472.CAN-15-1965.

[104] Adriana C Vidal, Lauren E Howard, Emily Wiggins, Amanda M De Hoedt, Stephen L Shiao, Simon Knott, Emanuela Taioli, Jay H Fowke, and Stephen J Freedland. Natural killer cell activity and prostate cancer risk in veteran men undergoing prostate biopsy. *Cancer Epidemiology*, 62:101578, 2019. ISSN 1877-7821. doi: https://doi.org/10.1016/j.canep.2019.101578.

[105] A Stojanovic and A Cerwenka. Natural Killer Cells and Solid Tumors. *Journal of Innate Immunity*, 3(4):355–364, 2011. ISSN 1662-811X. doi: 10.1159/000325465.

[106] Seyed Peyman Shariatpanahi, Seyed Pooya Shariatpanahi, Keivan Madjidzadeh, Moustapha Hassan, and Manuchehr Abedi-Valugerdi. Mathematical modeling of tumor-induced immunosuppression by myeloid-derived suppressor cells: Implications for therapeutic targeting strategies. *Journal of Theoretical Biology*, 442:1–10, 2018. ISSN 0022-5193. doi: 10.1016/j.jtbi.2018.01.006.

[107] Karen M Doersch, Kelvin A Moses, and Warren E Zimmer. Synergistic immunologic targets for the treatment of prostate cancer. *Experimental Biology and Medicine*, 241(17):1900–1910, 2016. doi: 10.1177/1535370216660212.

[108] Milad Qomlaqi, Fariba Bahrami, Maryam Ajami, and Jamshid Hajati. An extended mathematical model of tumor growth and its interaction with the immune system, to be used for developing an optimized immunotherapy treatment protocol. *Mathematical Biosciences*, 292:1–9, 2017. ISSN 18793134. doi: 10.1016/j.mbs.2017.07.006.

[109] Asad Usman and Chris Cunningham. Application of the Mathematical Model of Tumor- Immune Interactions for IL-2 Adoptive Immunotherapy to Studies on Patients with Metastatic Melanoma or Renal Cell Cancer. *Rose-Hulman Undergraduate Mathematics Journal*, 6(2), 2005.

[110] U. S. Food and Drug Administration/Center for Drug Evaluation and Research. Application number 203756Orig1s000 PHARMACOLOGY/TOXICOLOGY NDA REVIEW AND EVALUATION, 2012.

[111] V G Ghetie, E Sally Ward, and Ellen Vitetta. The Pharmacokinetics of Antibodies and Immunotoxins in Mice and Humans. In *Handbook of Anticancer Pharmacokinetics and Pharmacodynamics*, chapter 29, pages 298–475. Humana Press, Totowa, NJ, 2004. doi: 10.1007/978-1-59259-734-5_29.

[112] Josiah T Ryman and Bernd Meibohm. Pharmacokinetics of Monoclonal Antibodies. *CPT: pharmacometrics & systems pharmacology*, 6(9):576–588, sep 2017. ISSN 2163-8306 (Electronic). doi: 10.1002/psp4.12224.

[113] Patrick J Hensley and Natasha Kyprianou. Modeling Prostate Cancer in Mice: Limitations and Opportunities. *Journal of Andrology*, 33(2):133–144, 2012. doi: 10.2164/jandrol.111.013987.

[114] Julie Foucquier and Mickael Guedj. Analysis of drug combinations: current methodological landscape. *Pharmacology research & perspectives*, 3(3):e00149, jun 2015. ISSN 2052-1707 (Print). doi: 10.1002/prp2.149.

[115] C I BLISS. THE TOXICITY OF POISONS APPLIED JOINTLY1. *Annals of Applied Biology*, 26(3):585–615, 1939. doi: 10.1111/j.1744-7348.1939.tb06990.x.

[116] Inc. The MathWorks. MATLAB and Statistics Toolbox Release 2019b. *Natick, Massachusetts*, 2019.

[117] Eric J Small, N Simon Tchekmedyian, Brian I Rini, Lawrence Fong, Israel Lowy, and James P Allison. A Pilot Trial of CTLA-4 Blockade with Human Anti-CTLA-4 in Patients with Hormone-Refractory Prostate Cancer. *Clinical Cancer Research*, 13(6):1810–1815, 2007. ISSN 1078-0432. doi: 10.1158/1078-0432.CCR-06-2318.

[118] Anu Sharma, Sumit K Subudhi, Jorge Blando, Jorge Scutti, Luis Vence, Jennifer Wargo, James P Allison, Antoni Ribas, and Padmanee Sharma. Anti-CTLA-4 Immunotherapy Does Not Deplete FOXP3+ Regulatory T Cells (Tregs) in Human Cancers. *Clinical Cancer Research*, 25(4):1233–1238, 2019. ISSN 1078-0432. doi: 10.1158/1078-0432.CCR-18-0762.

[119] Natalie Kronik, Yuri Kogan, Moran Elishmereni, Karin Halevi-Tobias, Stanimir Vuk-Pavlović, and Zvia Agur. Predicting outcomes of prostate cancer immunotherapy by personalized mathematical models. *PLoS ONE*, 5(12), 2010. ISSN 19326203. doi: 10.1371/journal.pone.0015482.

[120] Takatoshi Chinen, Arun K Kannan, Andrew G Levine, Xiying Fan, Ulf Klein, Ye Zheng, Georg Gasteiger, Yongqiang Feng, Jason D Fontenot, and Alexander Y Rudensky. An essential role for the IL-2 receptor in Treg cell function. *Nature Immunology*, 17:1322, sep 2016. doi: 10.1038/ni.3540.

[121] Aiko Miyamura Ideta, Gouhei Tanaka, Takumi Takeuchi, and Kazuyuki Aihara. A Mathematical Model of Intermittent Androgen Suppression for Prostate Cancer. *Journal of Nonlinear Science*, 18(6):593, 2008. ISSN 1432-1467. doi: 10.1007/s00332-008-9031-0.

[122] Zhimin Wu, Tin Phan, Javier Baez, Yang Kuang, and Eric J. Kostelich. Predictability and identifiability assessment of models for prostate cancer under androgen suppression therapy. *Mathematical Biosciences and Engineering*, 16(5):3512, 2019. doi: 10.3934/mbe.2019176.

[123] Hong Bang Shim, Sang Eun Lee, Hyoung Keun Park, and Ja Hyeon Ku. Accuracy of a High Prostate-Specific Antigen Level for Prostate Cancer Diagnosis upon Initial Biopsy in Korean Men. *Yonsei Med J*, 48(4):678–683, aug 2007. ISSN 0513-5796. doi: 10.3349/ymj.2007.48.4.678.

[124] Annerleim Walton Diaz, Anthony N Hoang, Baris Turkbey, Cheng William Hong, Hong Truong, Todd Sterling, Soroush Rais-Bahrami, M Minhaj Siddiqui, Lambros Stamatakis, Srinivas Vourganti, Jeffrey Nix, Jennifer Logan, Colette Harris, Michael Weintraub, Celene Chua, Maria J Merino, Peter Choyke, Bradford J Wood, and Peter A Pinto. Can magnetic resonance-ultrasound fusion biopsy improve cancer detection in enlarged prostates? *The Journal of urology*, 190(6):2020–2025, dec 2013. ISSN 1527-3792 (Electronic). doi: 10.1016/j.juro.2013.05.118.

[125] Ersin Konyalioglu, Huseyin Tarhan, Ozgur Cakmak, Emel Ebru Pala, and Ferruh Zorlu. Prostate cancer volume estimations based on transrectal ultrasonography-guided biopsy in order to predict clinically significant prostate cancer. *International Braz J Urol: official journal of the Brazilian Society of Urology*, 41(3):442–448, 2015. ISSN 1677-6119 (Electronic). doi: 10.1590/S1677-5538.IBJU.2014.0251.

[126] Murali Varma and John M Morgan. The weight of the prostate gland is an excellent surrogate for gland volume. *Histopathology*, 57(1):55–58, 2010. doi: 10.1111/j.1365-2559.2010.03591.x.

[127] Cheryl D Fryar, Deanna Kruszan-Moran, Qiuping Gu, and Cynthia L Ogden. Mean body weight, weight, waist circumference, and body mass index among adults : United States, 1999–2000 through 2015–2016, 2018.

[128] D B Fearnley, L F Whyte, S A Carnoutsos, A H Cook, and D N J Hart. Monitoring Human Blood Dendritic Cell Numbers in Normal Individuals and in Stem Cell Transplantation. *Blood*, 93(2):728–736, 1999. ISSN 0006-4971.

[129] Sahamoddin Khailaie, Fariba Bahrami, Mahyar Janahmadi, Pedro Milanez-Almeida, Jochen Huehn, and Michael Meyer-Hermann. A mathematical model of immune activation with a unified self-nonself concept. *Frontiers in immunology*, 4:474, 2013. ISSN 1664-3224 (Print). doi: 10.3389/fimmu.2013.00474.

[130] J. Quinonez, N. Dasu, and M. Qureshi. A Mathematical Investigation on Tumor-Immune Dynamics: The Impact of Vaccines on the Immune Response. *Journal of Cancer Science and Therapy*, 9:675–682, 2017. doi: 10.4172/1948-5956.1000491.

[131] Stanimir Vuk-Pavlovic. Rebuilding immunity in cancer patients. *Blood cells, molecules & diseases*, 40(1):94–100, 2008. ISSN 1079-9796 (Print). doi: 10.1016/j.bcmd.2007.06.025.

[132] Z Bajzer, K Pavelic, and S Vuk-Pavlovic. Growth self-incitement in murine melanoma B16: a phenomenological model. *Science*, 225(4665):930–932, 1984. ISSN 0036-8075. doi: 10.1126/science.6382606.

[133] Zachary Reese, Ali Straubhar, Sumanta K Pal, and Neeraj Agarwal. Ipilimumab in the treatment of prostate cancer. *Future Oncology*, 11(1):27–37, 2015. doi: 10.2217/fon.14.196. PMID: 25572782.

[134] SF Slovin, CS Higano, O Hamid, S Tejwani, A Harzstark, JJ Alumkal, and HI Scher. Ipilimumab alone or in combination with radiotherapy in metastatic castration–resistant prostate cancer: results from an open–label, multicenter phase I/II study. *Annals of Oncology*, 24(7):1813–1821, 2013. doi: 10.1093/annonc/mdt107.

[135] Barbara Boldin. Introducing a Population into a Steady Community: The Critical Case, the Center Manifold, and the Direction of Bifurcation. *SIAM Journal on Applied Mathematics*, 66(4):1424–1453, 2006. doi: 10.1137/050629082.

[136] Jorge A Garcia. Sipuleucel-T in patients with metastatic castration-resistant prostate cancer: an insight for oncologists. *Therapeutic advances in medical oncology*, 3(2):101–108, mar 2011. ISSN 1758-8359 (Electronic). doi: 10.1177/1758834010397692.

[137] Channing J Paller and Emmanuel S Antonarakis. Sipuleucel-T for the treatment of metastatic prostate cancer. *Human Vaccines & Immunotherapeutics*, 8(4):509–519, 2012. doi: 10.4161/hv.18860. URL `https://doi.org/10.4161/hv.18860`.

[138] Chris Fellner. Ipilimumab (yervoy) prolongs survival in advanced melanoma: serious side effects and a hefty price tag may limit its use. *P & T : a peer-reviewed journal for formulary management*, 37(9):503–530, sep 2012. ISSN 1052-1372 (Print).

[139] Jeffrey S Weber, Reinhard Dummer, Veerle de Pril, Celeste Lebbé, F Stephen Hodi, and for the MDX010-20 Investigators. Patterns of onset and resolution of immune-related adverse events of special interest with ipilimumab. *Cancer*, 119(9):1675–1682, 2013. doi: 10.1002/cncr.27969.

[140] F Stephen Hodi, Steven J O'Day, David F McDermott, Robert W Weber, Jeffrey A Sosman, John B Haanen, Rene Gonzalez, Caroline Robert, Dirk Schadendorf, Jessica C Hassel, Wallace Akerley, Alfons J M van den Eertwegh, Jose Lutzky, Paul Lorigan, Julia M Vaubel, Gerald P Linette, David Hogg, Christian H Ottensmeier, Celeste Lebbé, Christian Peschel, Ian Quirt, Joseph I Clark, Jedd D Wolchok, Jeffrey S Weber, Jason Tian, Michael J Yellin, Geoffrey M Nichol, Axel Hoos, and Walter J Urba. Improved survival with ipilimumab in patients with metastatic melanoma. *The New England journal of medicine*, 363(8):711–723, aug 2010. ISSN 1533-4406 (Electronic). doi: 10.1056/NEJMoa1003466.

[141] S J O'Day, M Maio, V Chiarion-Sileni, T F Gajewski, H Pehamberger, I N Bondarenko, P Queirolo, L Lundgren, S Mikhailov, L Roman, C Verschraegen, R Humphrey, R Ibrahim,

V de Pril, A Hoos, and J D Wolchok. Efficacy and safety of ipilimumab monotherapy in patients with pretreated advanced melanoma: a multicenter single-arm phase II study. *Annals of Oncology*, 21(8):1712–1717, 2010. ISSN 0923-7534. doi: https://doi.org/10.1093/annonc/mdq013.

[142] Jedd D Wolchok, Bart Neyns, Gerald Linette, Sylvie Negrier, Jose Lutzky, Luc Thomas, William Waterfield, Dirk Schadendorf, Michael Smylie, Troy Guthrie, Jean-Jacques Grob, Jason Chesney, Kevin Chin, Kun Chen, Axel Hoos, Steven J O'Day, and Celeste Lebbé. Ipilimumab monotherapy in patients with pretreated advanced melanoma: a randomised, double-blind, multicentre, phase 2, dose-ranging study. *The Lancet Oncology*, 11(2):155–164, 2010. ISSN 1470-2045. doi: https://doi.org/10.1016/S1470-2045(09)70334-1.

[143] Trachette L. Jackson. A mathematical model of prostate tumor growth and androgen-independent relapse. *Discrete & Continuous Dynamical Systems - B*, 4, 2004. doi: 10.3934/dcdsb.2004.4.187.

[144] Yoshito Hirata, Nicholas Bruchovsky, and Kazuyuki Aihara. Development of a mathematical model that predicts the outcome of hormone therapy for prostate cancer. *Journal of Theoretical Biology*, 264(2):517–527, 2010. ISSN 0022-5193. doi: https://doi.org/10.1016/j.jtbi.2010.02.027.

[145] Javier Baez and Yang Kuang. Mathematical Models of Androgen Resistance in Prostate Cancer Patients under Intermittent Androgen Suppression Therapy. *Applied Sciences*, 6 (11), 2016. ISSN 2076-3417. doi: 10.3390/app6110352.

[146] Diletta Di Mitri, Alberto Toso, Jing Jing Chen, Manuela Sarti, Sandra Pinton, Tanja Rezzonico Jost, Rocco D'Antuono, Erica Montani, Ramon Garcia-Escudero, Ilaria Guccini, Sabela Da Silva-Alvarez, Manuel Collado, Mario Eisenberger, Zhe Zhang, Carlo Catapano, Fabio Grassi, and Andrea Alimonti. Tumour-infiltrating Gr-1+ myeloid cells antagonize senescence in cancer. *Nature*, 515:134, aug 2014. doi: 10.1038/nature13638.

[147] Karen A Autio, Phillip Wong, Angel Rabinowitz, Jianda Yuan, Lauryn Michelle Slavin, Ryan Brennan, Melineh DerSarkissian, Zhenyu Mu, Howard I Scher, and Alexander M Lesokhin. Presence of myeloid-derived suppressor cells (MDSC) in patients with metastatic castration-sensitive and castration-resistant prostate cancer. *Journal of Clinical Oncology*, 33(7_suppl):222, 2015. doi: 10.1200/jco.2015.33.7_suppl.222.

[148] Viktor Fleming, Xiaoying Hu, Rebekka Weber, Vasyl Nagibin, Christopher Groth, Peter Altevogt, Jochen Utikal, and Viktor Umansky. Targeting Myeloid-Derived Suppressor Cells to Bypass Tumor-Induced Immunosuppression. *Frontiers in Immunology*, 9:398, 2018. ISSN 1664-3224. doi: 10.3389/fimmu.2018.00398.

[149] Arianna Calcinotto, Clarissa Spataro, Elena Zagato, Diletta Di Mitri, Veronica Gil, Mateus Crespo, Gaston De Bernardis, Marco Losa, Michela Mirenda, Emiliano Pasquini, Andrea Rinaldi, Semini Sumanasuriya, Maryou B Lambros, Antje Neeb, Roberta Lucianò, Carlo A Bravi, Daniel Nava-Rodrigues, David Dolling, Tommaso Prayer-Galetti, Ana Ferreira, Alberto Briganti, Antonio Esposito, Simon Barry, Wei Yuan, Adam Sharp, Johann de Bono, and Andrea Alimonti. IL-23 secreted by myeloid cells drives castration-resistant prostate cancer. *Nature*, 559(7714):363–369, 2018. ISSN 1476-4687. doi: 10.1038/s41586-018-0266-0.

[150] R J Tesi. MDSC; the Most Important Cell You Have Never Heard Of. *Trends in Pharmacological Sciences*, 40(1):4–7, 2019. ISSN 0165-6147. doi: https://doi.org/10.1016/j.tips.2018.10.008.

[151] Richard P Tobin, Kimberly R Jordan, William A Robinson, Dana Davis, Virginia F Borges, Rene Gonzalez, Karl D Lewis, and Martin D McCarter. Targeting myeloid-derived suppressor cells using all-trans retinoic acid in melanoma patients treated with Ipilimumab. *International Immunopharmacology*, 63:282–291, 2018. ISSN 1567-5769. doi: https://doi.org/10.1016/j.intimp.2018.08.007.

[152] Editorial Overview. Natural killer cells for cancer immunotherapy: a new CAR is catching

up. *EBioMedicine*, 39:1–2, 2019. ISSN 2352-3964. doi: https://doi.org/10.1016/j.ebiom.2019.01.018.

[153] Alexander David Barrow and Marco Colonna. Exploiting NK Cell Surveillance Pathways for Cancer Therapy. *Cancers*, 11(1), 2019. ISSN 2072-6694. doi: 10.3390/cancers11010055.

[154] Behnaz Valipour, Kobra Velaei, Ali Abedelahi, Mohammad Karimipour, Masoud Darabi, and Hojjatollah Nozad Charoudeh. NK cells: An attractive candidate for cancer therapy. *Journal of Cellular Physiology*, 2019. doi: 10.1002/jcp.28657.

[155] Katayoun Rezvani, Rayne Rouce, Enli Liu, and Elizabeth Shpall. Engineering Natural Killer Cells for Cancer Immunotherapy. *Molecular Therapy*, 25(8):1769–1781, 2017. ISSN 1525-0016. doi: https://doi.org/10.1016/j.ymthe.2017.06.012.

[156] Anastasia Constantinidou, Constantinos Alifieris, and Dimitrios T Trafalis. Targeting Programmed Cell Death -1 (PD-1) and Ligand (PD-L1): A new era in cancer active immunotherapy. *Pharmacology & Therapeutics*, 194:84–106, 2019. ISSN 0163-7258. doi: https://doi.org/10.1016/j.pharmthera.2018.09.008.

[157] Alessandra Modena, Chiara Ciccarese, Roberto Iacovelli, Matteo Brunelli, Rodolfo Montironi, Michelangelo Fiorentino, Giampaolo Tortora, and Francesco Massari. Immune Checkpoint Inhibitors and Prostate Cancer: A New Frontier? *Oncology reviews*, 10(1): 293, apr 2016. ISSN 1970-5565 (Print). doi: 10.4081/oncol.2016.293.

[158] Jason M Redman, James L Gulley, and Ravi A Madan. Combining immunotherapies for the treatment of prostate cancer. *Urologic Oncology: Seminars and Original Investigations*, 35(12):694–700, 2017. ISSN 1078-1439. doi: https://doi.org/10.1016/j.urolonc.2017.09.024.

[159] Andrew L Laccetti and Sumit K Subudhi. Immunotherapy for metastatic prostate cancer: immuno-cold or the tip of the iceberg? *Current Opinion in Urology*, 27(6), 2017. ISSN 0963-0643. doi: 10.1097/MOU.0000000000000433.

[160] Marijo Bilusic, Ravi A Madan, and James L Gulley. Immunotherapy of Prostate Cancer: Facts and Hopes. *Clinical Cancer Research*, 2017. ISSN 1078-0432. doi: 10.1158/1078-0432. CCR-17-0019.

[161] Julie Nicole Graff, Joshi J Alumkal, Reid F Thompson, Amy Moran, George V Thomas, Mary A Wood, Charles G Drake, Rachel Slottke, and Tomasz M Beer. Pembrolizumab (Pembro) plus enzalutamide (Enz) in metastatic castration resistant prostate cancer (mCRPC): Extended follow up. *Journal of Clinical Oncology*, 36(15_suppl):5047, 2018. doi: 10.1200/JCO.2018.36.15_suppl.5047.

[162] Mark Robertson-Tessi, Ardith El-Kareh, and Alain Goriely. A mathematical model of tumor–immune interactions. *Journal of Theoretical Biology*, 294:56–73, 2012. ISSN 0022-5193. doi: https://doi.org/10.1016/j.jtbi.2011.10.027.

[163] Alexander Shimabukuro-Vornhagen, Philipp Gödel, Marion Subklewe, Hans Joachim Stemmler, Hans Anton Schlößer, Max Schlaak, Matthias Kochanek, Boris Böll, and Michael S von Bergwelt-Baildon. Cytokine release syndrome. *Journal for ImmunoTherapy of Cancer*, 6(1):56, 2018. ISSN 2051-1426. doi: 10.1186/s40425-018-0343-9.

[164] C Alberti. Prostate cancer immunotherapy, particularly in combination with androgen deprivation or radiation treatment. Customized pharmacogenomic approaches to overcome immunotherapy cancer resistance. *Il Giornale di chirurgia*, 37(5):225–235, 2017. ISSN 0391-9005 (Print). doi: 10.11138/gchir/2016.37.5.225.

[165] B Harpreet Singh and James L Gulley. Immunotherapy and therapeutic vaccines in prostate cancer: an update on current strategies and clinical implications. *Asian journal of andrology*, 16(3):364–371, 2014. ISSN 1745-7262 (Electronic). doi: 10.4103/1008-682X.122585.

[166] J Gao, Q He, S Subudhi, A Aparicio, A Zurita-Saavedra, D H Lee, C Jimenez, M Suarez-Almazor, and P Sharma. Review of immune-related adverse events in prostate cancer patients treated with ipilimumab: MD Anderson experience. *Oncogene*, 34(43):5411–5417, 2015. ISSN 1476-5594. doi: 10.1038/onc.2015.5.

[167] Caroline J Voskens, Simone M Goldinger, Carmen Loquai, Caroline Robert, Katharina C Kaehler, Carola Berking, Tanja Bergmann, Clemens L Bockmeyer, Thomas Eigentler, Michael Fluck, Claus Garbe, Ralf Gutzmer, Stephan Grabbe, Axel Hauschild, Rüdiger Hein, Gheorghe Hundorfean, Armin Justich, Ullrich Keller, Christina Klein, Christine Mateus, Peter Mohr, Sylvie Paetzold, Imke Satzger, Dirk Schadendorf, Marc Schlaeppi, Gerold Schuler, Beatrice Schuler-Thurner, Uwe Trefzer, Jens Ulrich, Julia Vaubel, Roger von Moos, Patrik Weder, Tabea Wilhelm, Daniela Göppner, Reinhard Dummer, and Lucie M Heinzerling. The Price of Tumor Control: An Analysis of Rare Side Effects of Anti-CTLA-4 Therapy in Metastatic Melanoma from the Ipilimumab Network. *PLOS ONE*, 8(1):1–17, 2013. doi: 10.1371/journal.pone.0053745.

[168] M. Scholz, S. Yep, M. Chancey, C. Kelly, K. Chau, J. Turner, and R. Lam. Phase I clinical trial of sipuleucel-T combined with escalating doses of ipilimumab in progressive metastatic castrate-resistant prostate cancer. *ImmunoTargets and Therapy*, 6:11–16, 2017. doi: 10.2147/ITT.S122497.

[169] Alexandra Olischewsky, Sofie De Schrijver, Agnes Bankfalvi, Axel Wetter, Lisa Zimmer, Elisabeth Livingstone, Dirk Schadendorf, and Selma Ugurel. Dose-dependent toxicity of ipilimumab in metastatic melanoma. *European Journal of Cancer*, 95:104–108, may 2018. ISSN 0959-8049. doi: 10.1016/j.ejca.2018.01.088.

[170] Utkarsh H Acharya and Joanne M Jeter. Use of ipilimumab in the treatment of melanoma. *Clinical pharmacology : advances and applications*, 5(Suppl 1):21–27, aug 2013. ISSN 1179-1438 (Print). doi: 10.2147/CPAA.S45884.